

TYPE THE TITLE OF DISSERTATION, WORDED EXACTLY AS IT
APPEARS ON YOUR ABSTRACT, ALL CAPS, INVERTED PYRAMID STYLE,
DOUBLE-SPACED IF MORE THAN ONE LINE

by

YOUR NAME

A DISSERTATION

Presented to the Program, School, or Department as appropriate
and the Graduate School of the University of Oregon
in partial fulfillment of the requirements
for the degree of
Doctor of Something

June 2019

DISSERTATION APPROVAL PAGE

Student: Your Name

Title: Title of Dissertation in Title Case, as it appears on The Abstract Page, No Line Breaks, Single Spaced, No Period at the End

This dissertation has been accepted and approved in partial fulfillment of the requirements for the Doctor of Something degree in the Program, School, or Department as appropriate by:

Chair's name	Chair
Advisor's name	Advisor
Member name	Core Member
Member name	Core Member
Outside member name	Institutional Representative

and

Janet Woodruff-Borden Vice Provost and Dean of the Graduate School

Original approval signatures are on file with the University of Oregon Graduate School.

Degree awarded June 2019

© 2019 Your Name

This work is licensed under a Creative Commons
Attribution-NonCommercial-NoDerivs (United States) License.



DISSERTATION ABSTRACT

Your Name

Doctor of Something

Official Department Name

June 2019

Title: Title of Dissertation in Title Case, as it appears on The Abstract Page, No Line Breaks, Single Spaced, No Period at the End

Indent first line of every paragraph of abstract text, which must be double spaced and no longer than 350 words.

CURRICULUM VITAE

NAME OF AUTHOR: Your Name

GRADUATE AND UNDERGRADUATE SCHOOLS ATTENDED:

University of Oregon, Eugene, OR

Name of previous graduate/undergraduate school (indent second line if needed)

DEGREES AWARDED:

Doctor of [insert degree name], [Major, if desired], [Year], University of Oregon

[Degree, Major, Year, School](indent second line if needed)

AREAS OF SPECIAL INTEREST:

[Name of Area of Special Interest]

PROFESSIONAL EXPERIENCE:

[Job Title, Employer, Duration]

GRANTS, AWARDS AND HONORS:

[Award, Project Title, Institution, Year]

PUBLICATIONS:

Thomas, D. R. K., & Smith, A. B. (2009). System models for the study of procrastination in high school students. *American Journal of Everything*, 100, 7–20.

Smith, A. B., Thomas, D. R. K., & Kemper, S. (2008). Models and instruments for analysis. E. Rampino & J. R. Douglas (Eds.), *Behavior analysis: The areas of research* (pp. 67-69). Englewood Cliffs, NJ: Prentice-Hall.

ACKNOWLEDGEMENTS

I thank Professors Smith and Jones for their assistance in the preparation of this manuscript. Special thanks are due to Mr. John Doe, whose familiarity with the needs and ideas of the community was helpful during the early programming phase of this undertaking. I also thank the members of the community councils for their valuable input. This research was supported in part by a Public Health Service Fellowship, Number 6 RP BV-22, 731-03, from the National Institutes of Mental Health, and by a grant from the National Science Foundation, ABC 123-45678, to Dr. John Smith at the University of Oregon.

TABLE OF CONTENTS

Chapter	Page
I. INTRODUCTION	1
II. BACTERIAL COHESION PREDICTS SPATIAL DISTRIBUTION IN THE LARVAL ZEBRAFISH INTESTINE	2
REFERENCES CITED	18
III. STATIONARY MOMENTS, DIFFUSION LIMITS, AND EXTINCTION TIMES FOR LOGISTIC GROWTH WITH RANDOM CATASTROPHES	22
3.1. Introduction	24
3.2. Background on the Logistic Random Catastrophe model	26
3.3. Results	27
3.4. Discussion	34
3.5. Materials and Methods	36
3.6. Acknowledgements	37
3.7. Detailed calculation of stationary moments	38
3.8. The diffusion limit and the Central Limit Theorem	42
3.9. An alternative mapping that equates stationary means	49
REFERENCES CITED	50
APPENDICES	

Chapter	Page
A. SUBLETHAL ANTIBIOTICS COLLAPSE GUT BACTERIAL POPULATIONS BY ENHANCING AGGREGATION AND EXPULSION	57
REFERENCES CITED	86
B. SWIMMING MOTILITY OF A GUT BACTERIAL SYMBIONT PROMOTES RESISTANCE TO INTESTINAL EXPULSION AND ENHANCES INFLAMMATION	100
B.1. Abstract	90
B.2. Introduction	91
B.3. Results	95
B.4. Discussion	114
B.5. Methods	118
B.6. Acknowledgements	134
B.7. Supporting Information	135
REFERENCES CITED	145
C. CONCLUSION	146

LIST OF FIGURES

Figure	Page
1.1. This is a short description that goes in the Table of Figures.	1
2.1. Diversity of bacterial population structures within the zebrafish intestine. (A) Schematic of a 5-day old larval zebrafish. (B) Schematic of a larval zebrafish intestine with the three general anatomical regions and their approximate relative sizes highlighted. (C) Representative images from across the range of observed population structures. Each image is a maximum intensity projection of a full 3D image stack, except for the top right inset, which is a single optical plane. Dashed amber lines trace the approximate boundaries of the intestine in each image. Examples of single cells (open arrowheads), small aggregates (closed arrowheads), and large aggregates (tailed arrowheads) are noted within insets under “sub-region”. See also Supplementary Movies 1-4. Top row: Populations of <i>V. cholerae</i> ZWU0020 localize to the anterior bulb and are dominated by highly motile planktonic cells (Supplementary Movie 1). Inset shows <i>V. cholerae</i> ZWU0020 cells in a different fish that was colonized with 1:100 mixture of green and red variants. The dilute channel (green) is shown. Middle row: Populations of <i>A. caviae</i> ZOR0002 typically contain a range of bacterial aggregate sizes, as indicated by arrows. Inset shows a zoomed-in view of the same intestine. Bottom row: Populations of <i>E. cloacae</i> ZOR0014 typically consist of small numbers of large aggregates. Inset shows a zoomed-in view of the same intestine.	15
2.2. Metrics of cohesion correlate with spatial distribution across bacterial strains. (A) the fraction of the population of each strain existing as single planktonic cells, (B) the average number of cells per cluster, and (C) the total number of clusters plotted against the population center, the center of mass position of each strain normalized by the length of the intestine. For the plots shown in B and C, individual cells are considered clusters of size 1. Circles show median values for each strain, bars show 25% and 75% quartiles. Trendlines were generated from the unweighted linear regression of log ₁₀ -transformed medians.	16
2.3. Signatures of a cohesion-distribution relationship can be detected within populations at the strain level. For each strain shown, the size of every cluster with size 2 cells and greater across all samples is plotted against its normalized position along the intestine	

<p>(small circles). Trendlines depict linear regressions of \log_{10}-transformed cluster sizes against position (black dashed lines). To better highlight trends, data were binned by position and the mean \pm standard deviation of cluster sizes were overlaid on each plot as large circles and bars.</p> <p>.1. Sample paths of LRC and LES models. A: A sample path from the LRC model. Simulation parameters: $r = 1$, $K = 10^4$, $\lambda = .07$, $f = 10^{-2}$, $dt = .01$. B: A sample path from the LES model. Simulation parameters: $r = 1$, $K = 10^4$, $\sigma = .53$, $dt = .01$.</p> <p>.2. Analytic results reveal statistical structure of LRC model. A: Analytic results for stationary cumulants agree with numerical simulations. Time evolution of the first 4 cumulants, C_n, of the LRC model, computed numerically (solid lines). Dashed lines indicate the asymptotic values predicted by the analytic results, with the cumulants computed from the moments given by equation (3). Parameters: $r = 1$, $K = 10^4$, $\lambda = .1$, $f = .0012$, $dt = .01$, $N_{trials} = 5 \cdot 10^5$. B: Range of validity of $\lambda \ln f$ as an effective catastrophe parameter. Parameters were scaled according to $\lambda' = \beta\lambda$ and $\ln f' = \beta^{-1} \ln f$ by dimensionless scale factor β. Dashed lines are analytic results for first 4 stationary cumulants as a function of β. Parameters same as in A.</p> <p>.3. The diffusion limit and extinction times. A: Smoothly transforming the stationary distribution of LRC model to that of LES model in the diffusion limit. LRC model (no extinction) was simulated for $T_{max} = 300$ units of inverse growth rate for 5 values of the scale parameter α, rescaling parameters according to equation (8). Frames i-v depict the stationary distribution of $\log X$ (for visual clarity) for $\alpha = 1, 2.94, 8.66, 25.49, 75.00$ respectively, estimated from 10^6 paths. Frame vi depicts the stationary distribution of $\log X$ for the target LES model. Parameters: $r = .68$, $K = 6800$, $\lambda = .1$, $\sigma = .8$, $\ln f = -\sigma/\sqrt{\lambda}$, $dt = .01$. B: Mean time to extinction increases as the LRC model is morphed into the LES model (bottom), despite the stationary mean remaining constant throughout the transformation (top). Parameters: Same as in A but α ranges logarithmically from 1 to 500 and $\sigma = 1$. C: Mean times to extinction for the beginning (purple circles) and end (green squares) points of the diffusion limit as a function of carrying capacity. Parameters: $r = 1$, $\lambda = .1$, $f = .01$, $N_{trials} = 5000$, $x_0 = 10$, $x^* = 1$. For LES endpoints, $\sigma^2 = \lambda \ln^2 f$. D: The exponent of this power law, obtained by linear regression, as a function of effective noise strengths. Parameters: $r = 1$, $f = .01$, $N_{trials} = 5000$, λ is varied from .06 to .4. For each value of λ, τ vs K is computed for 10 values of K ranging from 100 to 10000. The last 5 values are used to compute ν. For the LRC model, the x-axis corresponds</p>	<p>17</p> <p>53</p> <p>53</p> <p>53</p>
---	---

to $\sigma^2 = \lambda \ln^2 f$. The exponent appears to asymptotically follow a power law in σ^2 , consistent with [48] S1. Mean time to extinction is largely independent of initial starting population. Mean time to extinction, τ , plotted on a shifted log scale as a function of initial starting population, x_0 . Green squares denote the LES model, purple circles denote the LRC model. The mean extinction time, defined as the first hitting time to $x^* = 1$, starts from 0 but rapidly increases to a value independent of x_0 . Parameters: $r = 1$, $K = 10^4$, $\lambda = .1$, $f = .01$, $N_{trials} = 500$ S2. The LRC model has higher extinction risk than the LES model for equivalent stationary means. A: Illustration of the mapping. Numerical results for the average population plotted over time in the LRC (purple) and LES (green) models, showing both the cases of no extinction (dark solid lines) and extinction (light dashed lines) via an absorbing state at $x^* = 1$. LES model has the same growth rate and carrying capacity as the LRC model and σ is determined by $\sigma^2 = -2\lambda \ln f$, such that the two models have equal stationary means (Appendix C). Parameters: $r = 1$, $K = 10^4$, $\lambda = .1$, $f = .0012$, $\sigma = 1.16$, $dt = .01$, $N_{trials} = 5 \cdot 10^5$. B: Mean time to extinction, τ , in units of inverse growth rate, for LRC (purple circles) and LES (green squares) models as a function of noise strength, with $\sigma^2 = -2\lambda \ln f$. Parameters: $r = 1$, $dt = .01$, $N_{trials} = 5 \cdot 10^3$. For LRC model, $f = .01$ and λ was varied from .065 to .195. Inset: Mean time to extinction as a function of carrying capacity. Parameters: $r = 1$, $\lambda = .13$, $f = .01$, $\sigma = 1.09$, $dt = .01$, $N_{trials} = 5 \cdot 10^3$ S2. Two bacterial species show different extremes of in vivo aggregation phenotypes. A: Schematic of a zebrafish 5 days post-fertilization (dpf). B: Schematic of the larval zebrafish intestine with numbers denoting approximate fraction of gut length. C: <i>Vibrio cholerae</i> ZWU0020 in vivo. Left: a maximum intensity projection of a three-dimensional image of the full gut. Dense, bright bacteria and dimmer intestinal autofluorescence are evident. The orange dashed curve indicates a coarse outline of the gut boundary. Scale bar: 200 μm . Right: a single optical plane within the anterior bulb in a fish colonized with 1:100 green fluorescent protein (GFP): dTomato (dTOM)-expressing <i>Vibrio</i> , with the GFP channel shown to highlight individual microbes in the dense swarm. The orange dashed curve indicates the approximate contour of the intestinal epithelium. Black arrowheads indicate examples of single planktonic cells. Scale bar: 25 μm . (See also SI Movie 1) D: <i>Enterobacter cloacae</i> ZOR0014 in vivo, shown as a maximum intensity projection of the full gut (left) and a subset of the same projection in the anterior bulb (right); bacterial aggregates	54 55 55 56 56
---	----------------------------

- are evident. The black arrowhead indicates an example of a single planktonic cell; the white arrowhead indicates an example of a multicellular aggregate. Scale bars same as in (C). 59
- S2. **Low-dose ciprofloxacin induces *Vibrio* aggregation and expulsion in vivo.** A: Schematic of the experimental timeline. B: Schematic of the sampling scheme for plating measurements. C: Normalized abundances (number of colony forming units (CFUs) scaled by untreated medians) of water and gut populations. N values left to right: 8, 24, 7, 20, 6, 18, 5, 20. Water N values denote number of flasks; gut N values denote number of fish. D: Histograms of gut CFUs with pooled data from 24 and 48 h treatments. Counts indicate the number of individual fish with a given \log_{10} *Vibrio* CFUs. Dashed lines indicate the mean of each set, showing a ~100-fold reduction in intestinal *Vibrio* abundance in antibiotic-treated fish. E: Ensemble-averaged spatial distributions of log-transformed cell density as a function of distance along the gut axis, integrated over the perpendicular dimensions. F: Maximum intensity projections of 3D images of untreated (top) and ciprofloxacin-treated (bottom) *Vibrio* populations. Insets: Viability staining of bacteria expelled from the gut, with green and magenta indicating living and dead cells, respectively. G-H: Dynamics of in vivo *Vibrio* populations untreated (grey lines) and treated with 10 ng/ml ciprofloxacin (blue lines). G: 1D center of mass, normalized to intestine length. H: Total image-derived *Vibrio* abundance. In both (G) and (H), each curve represents a different zebrafish. Vertical dotted lines indicate the time of drug administration to the treatment cohort, $t = 0.67$ hours. 82
- S2. **Low-dose ciprofloxacin collapses *Enterobacter* populations and suppresses small clusters in vivo.** A: Normalized abundances (number of colony forming units (CFUs) scaled by untreated medians) of water and gut populations. N values left to right: 4, 20, 4, 20, 4, 19, 4, 20. Water N values denote number of flasks; gut N values denote number of fish. B: Histograms of gut CFUs with pooled data from 24 and 48 h treatments. Counts indicate the number of individual fish with a given \log_{10} *Enterobacter* CFUs. Dashed lines indicate the mean of each set, showing a ~1000-fold reduction in intestinal *Enterobacter* abundance in antibiotic-treated fish. C: Total number of bacterial clusters in the intestine, quantified from 3D images (Materials and Methods). D: Maximum intensity projections of 3D images of untreated (top) and ciprofloxacin-treated (bottom) *Enterobacter* populations. Insets: Viability staining of bacteria expelled from the gut, with green and magenta indicating living and dead cells, respectively. 83
- S2. **Small bacterial clusters are required for recovery after large expulsion events.** A: Maximum intensity projections

of untreated <i>Enterobacter</i> populations before (top, $t = 2$ hours from the start of imaging) and after (bottom, $t = 3$ hours) an expulsion event (See also SI Movie 5). Scale bar = 200 μm . B: Schematic of a kinetic model of bacterial cluster dynamics, illustrating its four constituent processes. C: Image-derived time-series of <i>Enterobacter</i> abundance in five untreated hosts showing sporadic large expulsion events.	84
S2. A stochastic kinetic model predicts bacterial cluster sizes and generates a phase diagram for in vivo abundance. A: The distribution of image-derived <i>Enterobacter</i> cluster sizes (grey circles) along with the prediction of our stochastic model (purple line). There are no free parameters in the fit; values were fixed by abundance, growth, and expulsion rate measurements independent of cluster size. Parameters: $r = 0.27 \text{ hr}^{-1}$, $\lambda = 0.11 \text{ hr}^{-1}$, $\alpha = 0.1 \text{ hr}^{-1}$, $\beta = 10^{1.5} \text{ hr}^{-1}$, $K = 10^5$. Error bars on experimental data are standard deviations across hosts. Shaded confidence intervals for the model prediction are bounds from parameter uncertainties. Inset: The same experimental data and model plotted without binning as a reverse cumulative distribution. B: Phase diagram of the log-transformed abundance, $\langle \log_{10}(N+1) \rangle$, showing the extinction transition (white dashed line). From best fit parameter estimates, the in vivo state of untreated <i>Enterobacter</i> is overlaid as a grey circle, and 25 ng/ml ciprofloxacin-treated <i>Enterobacter</i> as an orange circle; both circles are marked with “e”. Untreated <i>Vibrio</i> is located off the scale, indicated by the arrow, 10 ng/ml ciprofloxacin treated <i>Vibrio</i> is overlaid as a cyan circle marked with “v”. The doses for <i>Enterobacter</i> and <i>Vibrio</i> were established to be approximately equivalent in vitro. Parameters: $\lambda = 0.11 \text{ hr}^{-1}$, $\alpha = 0.1 \text{ hr}^{-1}$, $K = 10^5$ were fixed; r and β were varied on logarithmic grids.	85
S2. This is a short description that goes in the Table of Figures.	146

LIST OF TABLES

Table	Page
2.1. Bacterial strains and imaging-derived estimates of mono-association abundances <i>in vivo</i>. Abundances were estimated from 3D image stacks using the computational pipeline described in Methods and Supplementary Text	8

CHAPTER I

INTRODUCTION

A reference to an image can be done like this one, to Figure S2. You might also want to cite an article like this: [?].



FIGURE 1.1. This is a short description that goes in the Table of Figures. This is an extension of that description, which may include cascading turns of phrase, which appears directly below the figure as expected, but not in the table of figures which appears at the beginning of this exceedingly amazing dissertation.

CHAPTER II

BACTERIAL COHESION PREDICTS SPATIAL DISTRIBUTION IN THE LARVAL ZEBRAFISH INTESTINE

Are there general biophysical relationships governing the spatial organization of the gut microbiome? Despite growing realization that spatial structure is important for population stability, inter-bacterial competition, and host functions, it is unclear in any animal gut whether such structure is subject to predictive, unifying rules, or if it results from contextual, species-specific behaviors. To explore this, we used light sheet fluorescence microscopy to conduct a high-resolution comparative study of bacterial distribution patterns throughout the entire intestinal volume of live, larval zebrafish. Fluorescently tagged strains of seven bacterial symbionts, representing six different species native to zebrafish, were each separately mono-associated with animals that had been raised initially germ-free. The strains showed large differences in both cohesion—the degree to which they auto-aggregate—and spatial distribution. We uncovered a striking correlation between each strain’s mean position and its cohesion, whether quantified as the fraction of cells existing as planktonic individuals, the average aggregate size, or the total number of aggregates. Moreover, these correlations held within species as well; aggregates of different sizes localized as predicted from the pan-species observations. Together, our findings indicate that bacteria within the zebrafish intestine are subject to generic processes that organize populations by their cohesive properties. The likely drivers of this relationship, peristaltic fluid flow, tubular anatomy, and bacterial growth and aggregation kinetics, are common throughout animals. We therefore suggest that the framework introduced here, of

biophysical links between bacterial cohesion and spatial organization, should be useful for directing explorations in other host-microbe systems, formulating detailed models that can quantitatively map onto experimental data, and developing new tools that manipulate cohesion to engineer microbiome function.

Introduction

Dense and diverse communities of microbes reside in the intestines of humans and other animals. Their large impact on processes ranging from digestion to disease progression [1, 2, 3] motivates a great deal of work aiming to uncover determinants of community composition and function. Because of the size and anatomy of the gut, and because of the remarkable number of microbial species that coexist within it—hundreds to thousands in humans—it is widely believed that spatial organization plays an important role in orchestrating community structure [4, 5]. In support of this, for example, recent studies have shown that distinct groups of bacteria inhabit the luminal space of the intestine compared to the dense mucus layer lining the epithelium [6] and that distinct taxa are found in different regions along the length of the digestive tract [7]. The drivers of spatial organization are most often considered to be anatomical, as above, or biochemical, for example caused by variation in pH or the concentrations of nutrients, oxygen, or antimicrobial peptides [8].

Here, we suggest and demonstrate that the biophysical character of the microbes themselves, namely the degree to which they are planktonic or aggregated, can be a strong predictor of their population’s overall position within the intestine. In macroscopic ecological contexts, such relationships between morphology and spatial distribution are well known. For example, animal body

mass is greater in colder regions (Bergmann's rule), likely due to the scaling of surface driven heat loss with size; phytoplankton aggregation is correlated with position in the water column, due to buoyancy [9]; and seed mass varies robustly with latitude, for reasons that are still unclear [10].

It remains an open question whether gut microbes are governed by broad, pan-species principles linking cellular behavior and large-scale distribution, or whether spatial structure is contingent on context- and species-specific interactions. Investigating this requires high-resolution imaging within live animals in a controlled setting, which has only recently become possible. Uncovering such principles would demonstrate that despite the biochemical complexity of the vertebrate microbiota, general biophysical principles governing the architecture of gut microbial communities may exist.

Our study makes use of larval zebrafish (Fig. 1A, 1B), a model organism of particular utility to investigations of host-microbe interactions due to its anatomical and physiological similarities to other vertebrates, its optical transparency, and its amenability to gnotobiotic techniques for the creation of fish colonized only by particular microbial species [11, 76, 86, 99]. Zebrafish naturally associate with a diverse intestinal microbiome containing hundreds of bacterial species [15, 75] that influence a wide range of host processes [17, 18, 19, 20]. Earlier work on the dynamics of two native zebrafish bacterial symbionts [76] and a human-derived pathogen [86] showed associations between cellular growth mode, specifically whether the bacteria are planktonic or aggregated, and spatial distribution, specifically the location of the population along the length of the intestine, but the robustness and generality of this association remains unexplored.

As detailed below, we find across multiple bacterial strains, and even within strains, that greater aggregation is strongly correlated with more posterior localization.

Materials and Methods

Bacteria: All bacterial strains used in this study are listed in Table 1. Each strain was previously engineered via Tn7-mediated insertion to constitutively express either dTomato or sfGFP fluorescent reporters from a single chromosomal locus [77]. Archived stocks of bacteria were maintained in 25% glycerol at -80°C. Prior to experiments, bacteria were directly inoculated from frozen stocks into 5ml lysogeny broth (LB) media (10g/L NaCl, 5g/L yeast extract, 12g/L tryptone, 1g/L glucose) and grown for 16h (overnight) shaking at 30°C.

Animal care and gnotobiology: All experiments with zebrafish were done in accordance with protocols approved by the University of Oregon Institutional Animal Care and Use Committee and following standard operating procedures [96]. Wild-type (AB x TU strain) zebrafish were derived germ-free and colonized with bacterial strains as previously described [97] with slight modification (Supplemental Text).

Live imaging: Live imaging of larval zebrafish was conducted using a home-built light sheet fluorescence microscope previously described in detail [99]. The full volume of the intestine (approximately 1200x300x150 microns) is captured in four sub-regions that are registered in software following imaging. An entire intestine sampled with 1-micron steps between planes is imaged in less than 1 minute. All images were taken with an exposure time of 30ms and an excitation laser power of 5mW at 488 nm and 561 nm wavelengths.

Image analysis: Three-dimensional image stacks were analyzed using a pipeline described in detail in [99], with minor changes (Supplemental Text). The goal of the analysis is to identify the location and size of all bacterial clusters, ranging from individual, planktonic cells to large multicellular aggregates. Small objects are identified using a spot detection algorithm calibrated to over count spots, which are then filtered using a trained classifier (Supplemental Text). Large objects are segmented using a graph-cut algorithm [24], typically seeded with a mask obtained by intensity thresholding. The number of cells per multicellular aggregate is estimated by dividing the total fluorescence intensity of the aggregate by the average intensity of single cells in the same fish host. In cases where single cells are sparse or absent, the average is taken across all single cells for that strain. From these estimates we compute the 1D center of population mass, i.e. the mean position weighted by population density at each position, normalized by intestine length (“population center”), and also calculate the various cohesion metrics discussed in the text.

Data: To maximize statistical power, we combined newly acquired data with a recently published image dataset obtained under identical conditions [77]. The recently published data had been subjected to prior analysis to estimate overall bacterial abundances, but was reanalyzed here from scratch using the methods described above and in the Supplemental Text. The combined dataset consisted of N=6 fish per strain, except for *Plesiomonas* ZOR0011, which had N=3 fish. The output of our computational pipeline, a text file containing the size and location of every bacterial cluster, with identifiers for strain, fish, and dataset, is included in Supplemental Data File 1, with details on its format in the Supplemental Text. In

addition, a spreadsheet with the cohesion and distribution metrics plotted in Figure 2 is included in Supplemental Data File 2.

Experimental Design

To investigate this putative relationship, we analyzed seven bacterial strains representing six different species (Table 1). All were isolated from zebrafish intestines, where they are common and abundant [75]. Each species was previously engineered to constitutively express fluorescent proteins [77]. To deduce relationships governing species morphology and its interaction with the gut environment, we examined animals that were sufficiently developed to exhibit stereotypical intestinal transport, and sufficiently young to permit germ-free derivation and handling. We first raised larvae germ-free and allowed them to be colonized with individual bacterial strains by inoculation of the aqueous medium for 24 hours starting at four days post-fertilization (dpf) (Methods and Supplemental Text). During this developmental stage, until roughly 7 dpf, larvae need not be fed and are sustained on yolk-derived nutrients, enabling maintenance under gnotobiotic conditions. The larval intestine is, however, highly active beginning at 3.5 days [25] and exhibits a range of motility patterns, including coordinated peristalsis-like movements that are controlled by the enteric nervous system and can act on resident bacteria [76, 87]. After the colonization period, three-dimensional image stacks were acquired using a custom-built light sheet fluorescence microscope described in detail elsewhere [99]. The images span the entire larval intestine, roughly 200 x 200 x 1000 microns in extent, with single-bacterium resolution. Additional details are provided in Methods.

strain	median abundance
<i>Aeromonas veronii</i> ZOR0001	8.4×10^2
<i>Aeromonas caviae</i> ZOR0002	1.2×10^3
<i>Enterobacter cloacae</i> ZOR0014	3.5×10^3
<i>Plesiomonas</i> ZOR0011	4.6×10^3
<i>Pseudomonas mendocina</i> ZWU0006	3.5×10^2
<i>Vibrio cholerae</i> ZOR0036	1.6×10^3
<i>Vibrio cholerae</i> ZWU0020	2.0×10^4

TABLE 2.1. **Bacterial strains and imaging-derived estimates of mono-association abundances *in vivo*.** Abundances were estimated from 3D image stacks using the computational pipeline described in Methods and Supplementary Text

Results

Imaging multiple fish per strain revealed a broad spectrum of growth modes and bacterial distributions, ranging from the highly planktonic populations of *Vibrio cholerae* ZWU0020 located within the anterior ÒbulbÓ (Fig. 1C, top; Supplemental Movie 1) to the almost entirely aggregated populations of *Enterobacter cloacae* ZOR0014 located within the midgut (Fig. 1C, bottom). Most populations displayed intermediate mixtures of cellular growth modes and spatial distributions, similar to that of *Aeromonas caviae* ZOR0002 (Fig. 1C, middle; Supplemental Fig. 1, Supplemental Movies 2-4). As with observations of *Aeromonas* strains in earlier work [76], bacterial aggregates were dense, compact, and cohesive. The predominant difference in spatial position between species was their location along the longitudinal axis of the intestine. We observed no strains, for example, that localized along the radial axis, lining the gut epithelium.

We computationally identified each individual bacterium and aggregate in each three-dimensional image stack, and also determined the number of cells in each aggregate [99] (see Methods). For each population, we computed the center of

mass along the longitudinal axis of the intestine, normalized by the total intestinal length, to represent its spatial distribution. We also enumerated the fraction of the population present as planktonic cells to represent the strain's growth mode. Plotting each strain's planktonic fraction versus its population center shows a clear and striking correlation (Fig. 2A). Linear regression of \log_{10} -transformed planktonic fraction ($\log_{10} f_p$) against center of mass position (x_c) gives a coefficient of determination of $R^2 = 0.91$, and best-fit parameters

$$\log_{10} f_p = (0.81 \pm 0.32) + (-5.4 \pm 0.8)x_c. \quad (2.1)$$

Making use of our image segmentation of bacterial aggregates, we examined the relationship between mean object size and position. Defining a cluster as any group of bacteria (so that an individual bacterium is a cluster of size one), we find a strong correlation between each species' average cluster size (mean cells per cluster, C_c) and its center of mass (Fig. 2B, $R^2 = 0.79$);

$$\log_{10} C_c = (-0.74 \pm 0.47) + (4.9 \pm 1.1)x_c. \quad (2.2)$$

Because C_c is proportional to the total number of cells and inversely proportional to the number of clusters per fish (n_c), the relationship in Fig. 2B could be caused by a dependence on either or both of these factors. However, the total population of each species, save for *V. cholerae* ZWU0020, is roughly similar (Table 1); in contrast, n_c is strongly negatively correlated with position (Fig. 2C, $R^2 = 0.88$). Regression gives

$$\log_{10} n_c = (4.7 \pm 0.5) + (-6.6 \pm 1.1)x_c. \quad (2.3)$$

The slope, -6.6 ± 1.1 , is close to the negative of the slope of the C_c vs x_c relationship (4.9 ± 1.1), as would be expected if $C_c \sim 1/n_c$ with the overall population being species-independent. Together, the C_c vs x_c and n_c vs x_c relationships confirm the lack of a global correlation between abundance and location and imply instead that local interactions relate the size and positioning of aggregates.

We next asked if the relationship between aggregation and intestinal distribution we found between strains could be detected within individual strain populations, which would further support its biophysical generality. For this, we considered only clusters of two or more cells because individual cells dominate each dataset. For each strain, excluding *V. cholerae* ZWU0020 because it shows almost no aggregation (Fig. 2A), we combined measurements of cluster size and intestinal position from all specimens. We restricted our analysis to the anterior half of the intestine because the distal half rarely contained substantial populations (likely due to frequent intestinal expulsion), limiting our statistical power in that region. Regressing \log_{10} -transformed sizes of aggregates against their position (Fig. 3, small circles and dashed trendlines), we found a positive correlation between aggregate size and aggregate position for each of the six strains (Table 2). Finding this relationship within strains, as well as across strains, suggests a generic mechanism that spatially segregates bacterial cells based on their cohesive properties, resulting in the localization of small aggregates to the anterior of the intestine and larger aggregates to the posterior.

Discussion

Harnessing the natural variation displayed by native zebrafish symbionts and the spatial insights made possible by 3D live imaging, we have uncovered a quantitative relationship between bacterial cell behavior and large-scale spatial organization throughout the intestine. We found that across species and strains, the degree to which bacterial populations are aggregated, a biophysical characteristic we term “cohesion”, correlates strongly with their mean position along the intestine. Moreover, looking within strains we were able to detect further signatures of the cohesion-distribution correlation: namely, the size and location of individual aggregates are also correlated. These findings suggest that the relationship between cohesion and spatial structure represents a general principle that manifests across both taxonomic and cellular scales. Intriguingly, the diverse species and strains we examined each have well-defined characteristics, while together they span the range from almost wholly planktonic to almost wholly aggregated, with the corresponding range of intestinal locations. Each of these bacterial strains is a zebrafish gut symbiont, and so it is reasonable to suspect that traits such as degree of aggregation have evolved to enhance their fitness in the intestinal environment, or are responses to features of that environment. Through these traits, the bacteria have the capacity to influence how the intestine shapes their populations.

The specific mechanisms driving bacteria to aggregate may be complex. One can imagine, for example, simple adhesion of individual cells into clumps, assembly of aggregates through chemotaxis, and enchainment of daughter cells after division [72]. We note that specific motility behaviors do not in themselves explain aggregation; our data show that populations of both motile and non-motile strains [77] are capable of generating aggregates. These aggregates are perhaps

reminiscent of *in vitro* surface-mediated biofilms, but are distinct in that they form three-dimensional clumps in the intestinal lumen rather than lining the walls, and there is in general no simple mapping between strains' highly context dependent *in vitro* biofilm formation and *in vivo* aggregation. Nonetheless, investigating potential mechanisms of aggregation would be a valuable target for future studies, especially with an aim towards designing perturbations of cohesion.

We posit that the mechanism underlying the cohesion-distribution relationship emerges from the interplay between physical properties of the intestinal environment, especially its shape and peristaltic activity, and the cellular lifestyles of resident bacteria. As in all vertebrates, the larval zebrafish intestine is roughly tubular with a corrugated surface of villi, and transports and mixes contents using coordinated, periodic peristaltic contractions [28]. Earlier work looking solely at *A. veronii* ZOR0001 found aggregated microbes pushed and sporadically ejected by these contractions [76]; such forces more generally affect all aggregated bacteria. Theoretical studies of particle suspensions under low Reynolds number peristaltic flow also show spatial segregation of planktonic and aggregated cells [29]. These observations suggest that it should be possible to construct models that quantitatively match *in vivo* measurements and that offer predictions relevant for other animals, including humans. The development of such models will be challenging, as they must combine fluid dynamics, anatomy, and the nucleation, growth, and transport properties of bacterial aggregates. Aggregation kinetics are quantifiable from *in vivo* time-series imaging [99], and ongoing work, from both imaging and modeling, suggests that a robust, pan-species characterization of cluster dynamics is possible.

Even in the absence of such detailed models, however, it is reasonable to believe that the general relationship uncovered here will occur in larger systems, such as the human gut. Peristaltic transport, a tube-like geometry, and bacterial growth are universal features of all animal intestines. Given that Reynolds and Stokes numbers are low in both the zebrafish intestine and the much larger human intestine, we expect that the flow fields and particle transport that result from peristaltic contractions will be similar across scales. This similarity has already allowed quantitative comparisons of microbial compositions driven by pH and flow rates between in vitro fluidic devices and the human microbiome [30]. Therefore, the longitudinal segregation of bacterial clusters by size that we observed here may be a generic consequence of peristaltic activity. Moreover, the finer-scale structure of crypts and folds affords still further possibilities for spatial structuring driven by the associated flow fields and bacterial cohesion. Host anatomy, diet, and biochemical heterogeneity will likely complicate this picture, but we suggest that a general trend connecting bacterial morphology and intestinal position is reasonable to expect and intriguing to search for.

The relationship between cohesion and spatial distribution described here offers a framework for precision microbiome engineering. For example, by manipulating cohesion it may be possible to selectively displace bacterial populations from certain regions of the intestine or to remove them entirely. Reflecting this point, it was recently shown in a murine *Salmonella* vaccine model that antibody-mediated en chaining of bacterial cells led to aggregation and intestinal expulsion [72]. In addition, peristaltic activity can change in response to diet, therapeutic drugs, infection, and a range of chronic diseases. Therefore, elaborating the link between cohesion, spatial structure, and flow may help explain

diseases that result from microbial imbalances, and inspire methods for countering such changes in community composition through the targeted alteration of bacterial aggregation.

Author Contributions

BS, TW, KG, and RP designed the research. TW and EW performed gnotobiotic procedures. BS performed the imaging. BS, TW, and RP analyzed the data. All authors wrote the manuscript.

Acknowledgements

Research was supported through the M.J. Murdock Charitable Trust and an award from the Kavli Microbiome Ideas Challenge, a project led by the American Society for Microbiology in partnership with the American Chemical Society and the American Physical Society and supported by The Kavli Foundation. Work was also supported by the National Science Foundation under Award 1427957. Authors received funding from the National Institutes of Health (NIH, <http://www.nih.gov/>), P50GM09891 to KG and RP, F32AI112094 to TJW, and T32GM007759 to BHS. The funders had no role in study design, data collection and analysis, decision to publish, or preparation of the manuscript.

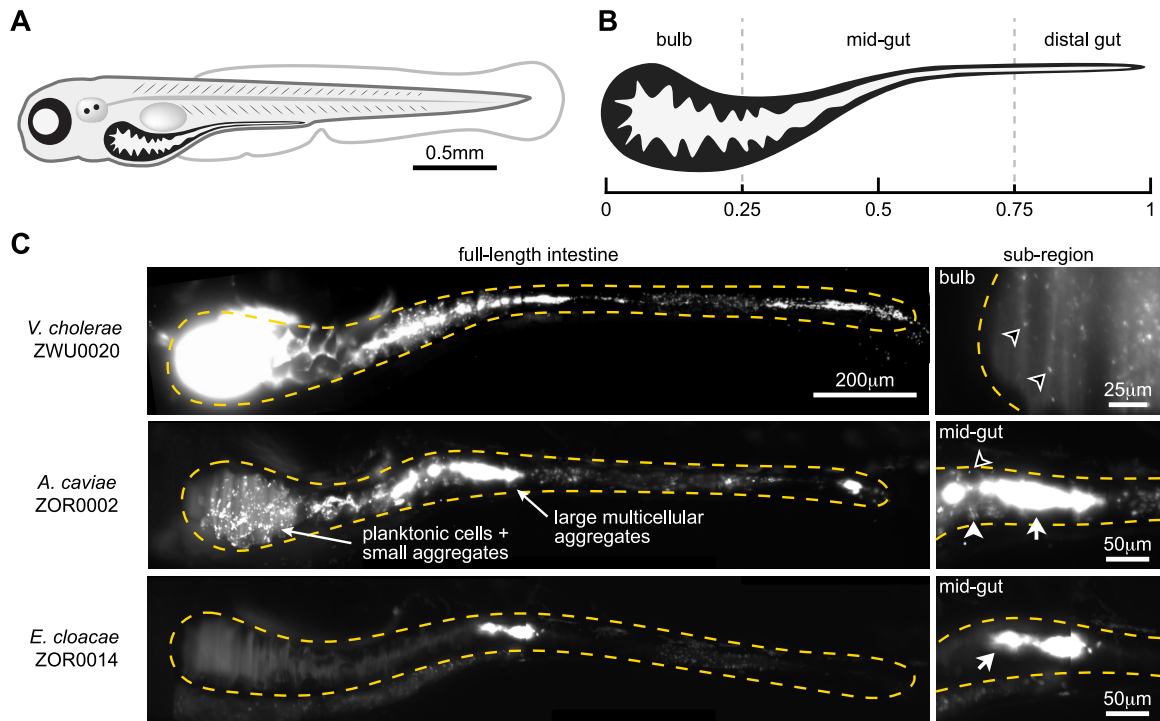


FIGURE 2.1. Diversity of bacterial population structures within the zebrafish intestine. (A) Schematic of a 5-day old larval zebrafish. (B) Schematic of a larval zebrafish intestine with the three general anatomical regions and their approximate relative sizes highlighted. (C) Representative images from across the range of observed population structures. Each image is a maximum intensity projection of a full 3D image stack, except for the top right inset, which is a single optical plane. Dashed amber lines trace the approximate boundaries of the intestine in each image. Examples of single cells (open arrowheads), small aggregates (closed arrowheads), and large aggregates (tailed arrowheads) are noted within insets under “sub-region”. See also Supplementary Movies 1-4. Top row: Populations of *V. cholerae* ZWU0020 localize to the anterior bulb and are dominated by highly motile planktonic cells (Supplementary Movie 1). Inset shows *V. cholerae* ZWU0020 cells in a different fish that was colonized with 1:100 mixture of green and red variants. The dilute channel (green) is shown. Middle row: Populations of *A. caviae* ZOR0002 typically contain a range of bacterial aggregate sizes, as indicated by arrows. Inset shows a zoomed-in view of the same intestine. Bottom row: Populations of *E. cloacae* ZOR0014 typically consist of small numbers of large aggregates. Inset shows a zoomed-in view of the same intestine.

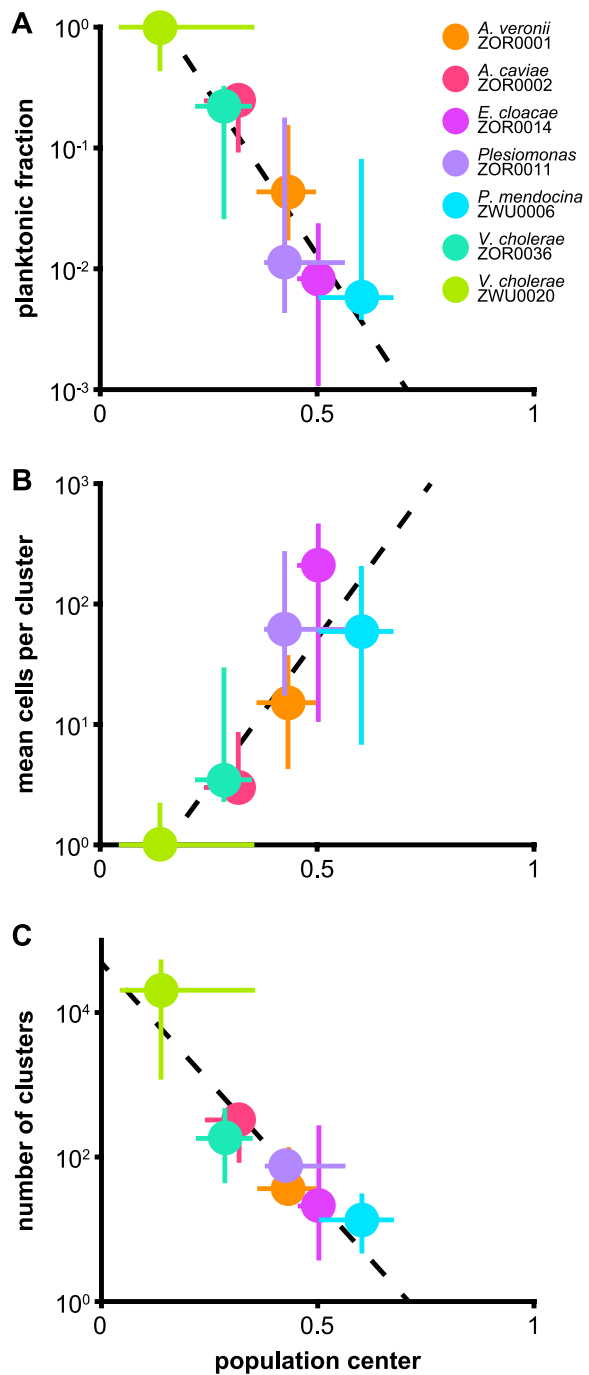


FIGURE 2.2. Metrics of cohesion correlate with spatial distribution across bacterial strains. (A) the fraction of the population of each strain existing as single planktonic cells, (B) the average number of cells per cluster, and (C) the total number of clusters plotted against the population center, the center of mass position of each strain normalized by the length of the intestine. For the plots shown in B and C, individual cells are considered clusters of size 1. Circles show median values for each strain, bars show 25% and 75% quartiles. Trendlines were generated from the unweighted linear regression of \log_{10} -transformed medians.

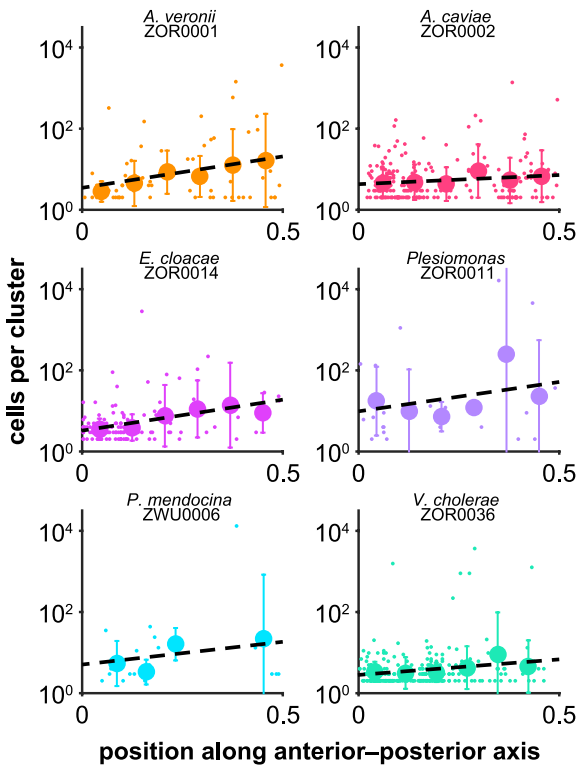


FIGURE 2.3. Signatures of a cohesion-distribution relationship can be detected within populations at the strain level. For each strain shown, the size of every cluster with size 2 cells and greater across all samples is plotted against its normalized position along the intestine (small circles). Trendlines depict linear regressions of \log_{10} -transformed cluster sizes against position (black dashed lines). To better highlight trends, data were binned by position and the mean \pm standard deviation of cluster sizes were overlaid on each plot as large circles and bars.

REFERENCES CITED

- [1] Laura M. Cox, Shingo Yamanishi, Jiho Sohn, Alexander V. Alekseyenko, Jacqueline M. Leung, Ilseung Cho, Sungheon G. Kim, Huilin Li, Zhan Gao, Douglas Mahana, Jorge G. Zárate Rodriguez, Arlin B. Rogers, Nicolas Robine, P'Ng Loke, and Martin J. Blaser. Altering the intestinal microbiota during a critical developmental window has lasting metabolic consequences. *Cell*, 158(4):705–721, 2014.
- [2] Parag Kundu, Eran Blacher, Eran Elinav, and Sven Pettersson. Our Gut Microbiome: The Evolving Inner Self. *Cell*, 171(7):1481–1493, 2017.
- [3] Peter T. McKenney and Eric G. Pamer. From Hype to Hope: The Gut Microbiota in Enteric Infectious Disease. *Cell*, 163(6):1326–1332., 2015.
- [4] Jessica L. Mark Welch, Yuko Hasegawa, Nathan P. McNulty, Jeffrey I. Gordon, and Gary G. Borisy. Spatial organization of a model 15-member human gut microbiota established in gnotobiotic mice. *Proceedings of the National Academy of Sciences*, page 201711596, 2017.
- [5] Carolina Tropini, Kristen A. Earle, Kerwyn Casey Huang, and Justin L. Sonnenburg. The Gut Microbiome: Connecting Spatial Organization to Function. *Cell Host and Microbe*, 21(4):433–442, 2017.
- [6] Thierry Pédron, Céline Mulet, Catherine Dauga, Lionel Frangeul, Christian Chervaux, Gianfranco Grompone, and Philippe J. Sansonettia. A crypt-specific core microbiota resides in the mouse colon. *mBio*, 3(3):e00116–12, 2012.
- [7] Koji Yasuda, Keunyoung Oh, Boyu Ren, Timothy L. Tickle, Eric A. Franzosa, Lynn M. Wachtman, Andrew D. Miller, Susan V. Westmoreland, Keith G. Mansfield, Eric J. Vallender, Gregory M. Miller, James K. Rowlett, Dirk Gevers, Curtis Huttenhower, and Xochitl C. Morgan. Biogeography of the intestinal mucosal and luminal microbiome in the rhesus macaque. *Cell Host and Microbe*, 17(3):385–391, 2015.
- [8] Gregory P. Donaldson, S. Melanie Lee, and Sarkis K. Mazmanian. Gut biogeography of the bacterial microbiota. *Nature Reviews Microbiology*, 14(1):20–32, 2015.
- [9] Daniel C.O. Thornton. Diatom aggregation in the sea: Mechanisms and ecological implications. *European Journal of Phycology*, 37(2):149–161, 2002.

- [10] A. T. Moles and M. Westoby. Latitude, seed predation and seed mass. *Journal of Biogeography*, 30(1):105–128, 2003.
- [11] Adam R. Burns and Karen Guillemin. The scales of the zebrafish: host–microbiota interactions from proteins to populations. *Current Opinion in Microbiology*, 38:137–141, 2017.
- [12] Matthew Jemielita, Michael J Taormina, Adam R Burns, Jennifer S Hampton, Annah S Rolig, Karen Guillemin, and Raghuveer Parthasarathy. Spatial and temporal features of the growth of a bacterial\`nspecies colonizing the zebrafish gut. *MBio*, 5(6):1–8, 2014.
- [13] Savannah L. Logan, Jacob Thomas, Jinyuan Yan, Ryan P. Baker, Drew S. Shields, Joao B. Xavier, Brian K. Hammer, and Raghuveer Parthasarathy. The Vibrio cholerae type VI secretion system can modulate host intestinal mechanics to displace gut bacterial symbionts. *Proceedings of the National Academy of Sciences*, 115(16):E3779–E3787, 2018.
- [14] Travis J. Wiles, Matthew Jemielita, Ryan P. Baker, Brandon H. Schlomann, Savannah L. Logan, Julia Ganz, Ellie Melancon, Judith S. Eisen, Karen Guillemin, and Raghuveer Parthasarathy. Host Gut Motility Promotes Competitive Exclusion within a Model Intestinal Microbiota. *PLoS Biology*, 14(7):1–24, 2016.
- [15] Annah S. Rolig, Erika K. Mittge, Julia Ganz, Josh V. Troll, Ellie Melancon, Travis J. Wiles, Kristin Alligood, W. Zac Stephens, Judith S. Eisen, and Karen Guillemin. The enteric nervous system promotes intestinal health by constraining microbiota composition. *PLoS Biology*, 15(2):e2000689, 2017.
- [16] W. Zac Stephens, Adam R. Burns, Keaton Stagaman, Sandi Wong, John F. Rawls, Karen Guillemin, and Brendan J.M. Bohannan. The composition of the zebrafish intestinal microbial community varies across development. *ISME Journal*, 10:644–654, 2016.
- [17] James M. Davison, Colin R. Lickwar, Lingyun Song, Ghislain Breton, Gregory E. Crawford, and John F. Rawls. Microbiota regulate intestinal epithelial gene expression by suppressing the transcription factor Hepatocyte nuclear factor 4 alpha. *Genome Research*, pages gr—220111, 2017.
- [18] Jennifer Hampton Hill, Eric A. Franzosa, Curtis Huttenhower, and Karen Guillemin. A conserved bacterial protein induces pancreatic beta cell expansion during zebrafish development. *eLife*, 5:e20145, 2016.

- [19] Drake Phelps, Nichole E. Brinkman, Scott P. Keely, Emily M. Anneken, Tara R. Catron, Doris Betancourt, Charles E. Wood, Scott T. Espenschied, John F. Rawls, and Tamara Tal. Microbial colonization is required for normal neurobehavioral development in zebrafish. *Scientific Reports*, 7(1):11244, 2017.
- [20] Joshua V. Troll, M. Kristina Hamilton, Melissa L. Abel, Julia Ganz, Jennifer M. Bates, W. Zac Stephens, Ellie Melancon, Michiel van der Vaart, Annemarie H. Meijer, Martin Distel, Judith S. Eisen, and Karen Guillemin. Microbiota promote secretory cell determination in the intestinal epithelium by modulating host Notch signaling. *Development*, 145(4):dev155317, 2018.
- [21] Travis J. Wiles, Elena S. Wall, Brandon H. Schlomann, Edouard A. Hay, Raghuveer Parthasarathy, and Karen Guillemin. Modernized tools for streamlined genetic manipulation and comparative study of wild and diverse proteobacterial lineages. *mBio*, 9(5):e01877–18, 2018.
- [22] M. Westerfield. The Zebrafish Book. A Guide for the Laboratory Use of Zebrafish (*Danio rerio*), 5th Edition. *University of Oregon Press, Eugene (Book)*, 2007.
- [23] E. Melancon, S. Gomez De La Torre Canny, S. Sichel, M. Kelly, T. J. Wiles, J. F. Rawls, J. S. Eisen, and K. Guillemin. Best practices for germ-free derivation and gnotobiotic zebrafish husbandry. *Methods in Cell Biology*, 138:61–100, 2017.
- [24] Y. Boykov and V. Kolmogorov. An experimental comparison of min-cut/max-flow algorithms for energy minimization in vision. *IEEE Transactions on Pattern Analysis and Machine Intelligence*, 26(9):1124–1137, 2004.
- [25] Iain Shepherd and Judith Eisen. Development of the zebrafish enteric nervous system. In *Methods in cell biology*, volume 101, pages 143–160. Elsevier, 2011.
- [26] J. Ganz, R. P. Baker, M. K. Hamilton, E. Melancon, P. Diba, J. S. Eisen, and R. Parthasarathy. Image velocimetry and spectral analysis enable quantitative characterization of larval zebrafish gut motility. *Neurogastroenterology & Motility*, 30(9):e13351, 2018.
- [27] Kathrin Moor, Médéric Diard, Mikael E. Sellin, Boas Felmy, Sandra Y. Wotzka, Albulena Toska, Erik Bakkeren, Markus Arnoldini, Florence Bansept, Alma Dal Co, Tom Völler, Andrea Minola, Blanca Fernandez-Rodriguez, Gloria Agatic, Sonia Barbieri, Luca Piccoli, Costanza Casiraghi, Davide Corti, Antonio Lanzavecchia, Roland R. Regoes, Claude Loverdo, Roman Stocker, Douglas R. Brumley, Wolf Dietrich Hardt, and Emma Slack. High-avidity IgA protects the intestine by en chaining growing bacteria. *Nature*, 544(7651):498, 2017.

- [28] Kenneth N. Wallace, Shafinaz Akhter, Erin M. Smith, Kristin Lorent, and Michael Pack. Intestinal growth and differentiation in zebrafish. *Mechanisms of Development*, 122(2):157–173, 2005.
- [29] Joel Jiménez-Lozano, Mihir Sen, and Patrick F. Dunn. Particle motion in unsteady two-dimensional peristaltic flow with application to the ureter. *Physical Review E - Statistical, Nonlinear, and Soft Matter Physics*, 79(4):18–20, 2009.
- [30] Jonas Cremer, Igor Segota, Chih-yu Yang, Markus Arnoldini, John T. Sauls, Zhongge Zhang, Edgar Gutierrez, Alex Groisman, and Terence Hwa. Effect of flow and peristaltic mixing on bacterial growth in a gut-like channel. *Proceedings of the National Academy of Sciences*, 113(41):11414–11419, 2016.

CHAPTER III

STATIONARY MOMENTS, DIFFUSION LIMITS, AND EXTINCTION TIMES FOR LOGISTIC GROWTH WITH RANDOM CATASTROPHES

A central problem in population ecology is understanding the consequences of stochastic fluctuations. Analytically tractable models with Gaussian driving noise have led to important, general insights, but they fail to capture rare, catastrophic events, which are increasingly observed at scales ranging from global fisheries to intestinal microbiota. Due to mathematical challenges, growth processes with random catastrophes are less well characterized and it remains unclear how their consequences differ from those of Gaussian processes. In the face of a changing climate and predicted increases in ecological catastrophes, as well as increased interest in harnessing microbes for therapeutics, these processes have never been more relevant. To better understand them, I revisit here a differential equation model of logistic growth coupled to density-independent catastrophes that arrive as a Poisson process, and derive new analytic results that reveal its statistical structure. First, I derive exact expressions for the model's stationary moments, revealing a single effective catastrophe parameter that largely controls low order statistics. Then, I use weak convergence theorems to construct its Gaussian analog in a limit of frequent, small catastrophes, keeping the stationary population mean constant for normalization. Numerically computing statistics along this limit shows how they transform as the dynamics shifts from catastrophes to diffusions, enabling quantitative comparisons. For example, the mean time to extinction increases monotonically by orders of magnitude, demonstrating significantly higher extinction risk under catastrophes than under diffusions. Together, these results provide

insight into a wide range of stochastic dynamical systems important for ecology and conservation.

3.1. Introduction

Stochastic fluctuations are important drivers of ecological and evolutionary processes [31, 32, 33, 34]. Understanding their consequences is essential for ecological management, as well as for explaining observed patterns of biodiversity [32]. Given that data is often limited, general principles of stochastic population dynamics derived from the mathematical analysis of minimal models can be immensely useful [32, 35]. For example, in classic work [36] Beddington and May derive for a stochastic logistic growth model how harvesting yields become less predictable as harvesting rates increase, a phenomenon that was suggested by historical fisheries data at the time [37]. Extensions of this analysis have led to threshold harvesting strategies that are proven optimal for a wide class of stochastic growth models that include extinction [38]. Beyond harvesting theory, analytically tractable models have led to diverse ecological and evolutionary insights [31, 33, 39].

In these types of analyses, stochasticity is often modeled by coupling growth to a Gaussian noise process, leading to stochastic differential equations that are amenable to well established tools from diffusion theory [32, 40]. However, large, abrupt catastrophes are not captured by Gaussian models and are better modeled by discontinuous stochastic processes. These catastrophes are increasingly observed in a variety of ecological systems. On global scales, ecological catastrophes have already been observed as the result of rapid warming and are expected to become more frequent as the climate continues to change [41]. At the opposite extreme, the intestinal microbiomes of humans and other animals are observed to undergo abrupt compositional changes following perturbations, such as antibiotic treatments [42, 43, 45, 78]. At all scales, efforts to understand and manipulate

ecological systems would greatly benefit from general, quantitative principles of how perturbations and catastrophes shape population statistics.

I address this issue here by analytically and numerically studying a single-species model of logistic growth coupled to discontinuous, multiplicative jumps that arrive as a Poisson process, introduced in [46] and referred to here as the Logistic Random Catastrophe (LRC) model (Figure 1A). Using the method of moment equations [47], I derive exact expressions for the stationary moments of the population distribution, neglecting the possibility of extinction. These results provide a direct look into the statistical structure of the LRC model, revealing a single, effective catastrophe parameter that largely controls ensemble statistics. This effective parameter was recently observed empirically in computer simulations and aided the analysis of experimental data, but there was no theoretical basis for its existence [45].

With this insight, I then turn to an old and fundamental problem: which dynamics, intermittent random catastrophes or continuous stochasticity, poses a higher risk of extinction? For models of exponential growth up to a hard wall carrying capacity in the presence of either multiplicative Gaussian noise, called environmental stochasticity, or random, multiplicative Poisson catastrophes, Lande [48] derives how the mean time to extinction scales as a power law in the carrying capacity for positive long-run growth rate, with the exponent depending on the details of the particular model. This similarity in scaling behavior implies similar extinction risk in a qualitative sense, but it remains unclear how to construct a meaningful quantitative comparison, since the noise parameters of the two models describe distinct processes.

To circumvent this issue, I propose a method that treats the models not as distinct processes, but as extreme versions of the same process. Using functional generalizations of the Central Limit Theorem [49] and drawing inspiration from renormalization methods in theoretical physics [50, 51], I analytically construct the diffusion analog of the LRC model, referred to here as the Logistic Environmental Stochasticity model (Figure 1B), in the limit of infinitely frequent, infinitesimal catastrophes, such that the stationary mean of the process remains constant. In this way, the problem of quantitatively comparing two distinct models is traded for the more straightforward problem of computing statistics of one model as a function of parameters, specifically, along a particular limit in parameter space. I apply this method to the comparison of extinction times and find that the mean time to extinction increases monotonically along this limit by orders of magnitude in a wide region of parameter space, implying significantly higher risk of extinction under random catastrophes dynamics in general.

Taken together, these results highlight the power of analytically tractable models of stochastic population dynamics. The expressions derived here aid the analysis of experimental and observational data, inform the design of computer simulations, and reveal deep connections between distinct stochastic processes relevant for a wide range of ecological systems.

3.2. Background on the Logistic Random Catastrophe model

Hanson and Tuckwell [46] introduce an ideal minimal model for the study of random catastrophes in isolation from additional complications: single-species logistic growth coupled to constant fraction catastrophes that arrive as a Poisson process, referred to here as the Logistic Random Catastrophe (LRC) model. The

LRC model can be written analytically as an Itô Stochastic Differential Equation (SDE):

$$dX_t = rX_t \left(1 - \frac{X_t}{K}\right) dt - (1-f)X_t dN_t. \quad (3.1)$$

The first term on the right hand side, of order dt , encodes deterministic logistic growth with growth rate r and carrying capacity K . The second term encodes random catastrophes with the use of a differential Poisson process, dN_t , which is equal to one if a catastrophe happens at time t and zero otherwise. Poisson catastrophes arrive with a constant probability per unit time, λ , and have a size set by f , the fraction of the population remaining after catastrophe. The notation $X_t - dN_t$ indicates the Itô integration convention [52]. By including logistic growth, the LRC model captures realistic density-dependent regulation; by including catastrophes of constant fraction, it captures the realistic feature that larger populations can experience larger losses, assuming that all individuals are equally susceptible to the disturbance. Despite its simplicity, much about the statistical structure of the LRC model remains mysterious, due to the combined complications of the discontinuous Poisson process and nonlinear logistic growth.

3.3. Results

3.3.1. Deriving exact expressions for LRC stationary moments

I present here exact results for the stationary moments of the LRC model in absence of extinction, derived with the method of moment equations. The method of moment equations turns a stochastic differential equation into a deterministic differential equation for the moment in question by averaging. For nonlinear SDEs this results in a hierarchy of moment equations, in which each

moment is coupled to higher moments, that generally cannot be solved exactly. However, in the absence of extinction, this hierarchy reduces in the steady state to an algebraic recursion relation, which in the case of the LRC model is a simple relation between $\mathbb{E}[X^{n+1}]$ and $\mathbb{E}[X^n]$ (Appendix A). This recursion relation can be iterated to express each moment just as a function of the mean. The mean in turn can be computed independently from the steady state condition on $\ln X$ (Appendix A), resulting in

$$\mathbb{E}[X]_{LRC} = K \left(1 + \frac{\lambda}{r} \ln f \right). \quad (3.2)$$

(recall that $f \in (0, 1)$, so $\ln f$ is negative for $f < 1$). This then determines all higher moments:

$$\mathbb{E}[X^n] = K^n \left(1 + \frac{\lambda}{r} \ln f \right) \prod_{m=1}^{n-1} \left(1 - \frac{\lambda(1-f^m)}{mr} \right), \quad n \geq 2. \quad (3.3)$$

The stationary variance is readily computed to be

$$\text{Var}[X]_{LRC} = K^2 \frac{\lambda}{r} (-\ln f - (1-f)) \left(1 + \frac{\lambda}{r} \ln f \right). \quad (3.4)$$

These results agree well with simulations, as shown in Figure 2A in the form of cumulants [53], which generally provide more intuitive information than moments. The solid lines show the time evolution of the first 4 cumulants, C_n , of the LRC model, computed via stochastic simulation of the Poisson process with no absorbing state representing extinction (Materials and Methods). The dashed lines are the analytic results, computed from the expressions for the moments in equation (3) [53]. Each cumulant asymptotes to the analytic value.

3.3.2. A single, effective catastrophe parameter largely controls LRC moments

EDIT THIS SECTION

These analytic results suggest that the parameter combination $\lambda \ln f$ plays an important role in determining population statistics. To investigate its role, I computed the response of the first four stationary cumulants of the LRC model to simultaneous, reciprocal scaling of λ and $\ln f$ via a dimensionless scale factor, β . Specifically, parameters were scaled according to

$$\lambda' = \beta\lambda, \quad \ln f' = \beta^{-1} \ln f. \quad (3.5)$$

In regions of parameter space where statistics depend only on the effective parameter $\lambda \ln f$, curves of cumulants as a function of β will be flat. The results are shown Figure 2B for β ranging from $10^{-2} - 10^3$. Stationary moments were computed for each value of β using the analytic results derived above and converted to cumulants [53]. The stationary mean is invariant under this scaling, as indicated by equation (2). Higher order cumulants are approximately invariant for low values of β , which correspond to rare, large catastrophes, but decay to zero for large values of β , which correspond to frequent, small catastrophes.

The behavior of LRC cumulants under scalings of β can be understood by considering different limits of the two timescales of the model, namely the scales of growth and of catastrophe. Consider a population that started from carrying capacity and then experienced a catastrophe. The timescale of recovery back to carrying capacity, t_R , can be estimated by the time to reach half the carrying capacity, which is given by $-r^{-1} \ln f$. The typical time between catastrophes,

t_C , is given by λ^{-1} . The regime $t_C \ll t_R$ corresponds to large β , specifically, $\beta \gg (-r^{-1}\lambda \ln f)^{-1/2}$. As β increases, the size of the jumps becomes small fast enough to result in a deterministic limit, a dynamic analog of the law of large numbers. To see this, recall that for a Poisson process, all cumulants are equal to the mean, λt , just as all cumulants of a Poisson distribution are equal to the mean. The n^{th} cumulant of the scaled process $(1 - f)N_t$ is therefore $(1 - f)^n \lambda t$. The limit $\beta \rightarrow \infty$ corresponds to $\lambda' \rightarrow \infty$ and $f' \rightarrow 1$, such that $\lambda' \ln f'$ is constant. In this limit, $-(1 - f)$ is well approximated by $\ln f$, so, higher cumulants of the scaled process decay as $\beta^{-(n-1)}$, resulting in a deterministic model.

The other regime, $t_C \gg t_R$, corresponds to small β , specifically, $\beta \ll (-r^{-1}\lambda \ln f)^{-1/2}$. In this regime, since catastrophes are rare and populations can recover from them, only a single catastrophe per population needs to be considered. A population at time t will be at carrying capacity unless a catastrophe occurred recently enough that the population is still recovering, *i.e.*, if the catastrophe occurred in the interval $(t - t_R, t)$. The number of trajectories to have a collapse in this interval is governed by a Poisson distribution with mean $\lambda t_R = -r^{-1}\lambda \ln f$. The fact this this distribution is invariant under scalings of β suggests that cumulants of the full LRC model in this limit are as well, though further analysis is needed make this connection rigorous.

Finally, when $t_C \sim t_R$, the statistics of the LRC model are governed by a more complicated interaction of growth and collapse timescales, and the invariance under β scalings is lost; moments depend on λ and f independently via equation (3).

The effective parameter $\lambda \ln f$ has an intuitive interpretation: It is the correction to the long-run growth rate due to catastrophes, and has been previously

identified as an important quantity in a variety of related models [48, 52, 54]. Its existence has important consequences for analyzing experimental data. As was done in [45], fitting ensemble statistics with the effective catastrophe parameter reduces the number of parameters that needs to be estimated. In fact, attempting to fit both the rate (λ) and size (f) independently results in highly unconstrained parameter estimates [45] and should be avoided. The analytic results derived here put the use of the effective parameter, $\lambda \ln f$, on firmer ground and explicitly delineate the range of its validity.

3.3.3. The diffusion limit shows that random catastrophes pose higher extinction risk than environmental stochasticity

I now consider the problem of quantitatively comparing extinction risks in the LRC model and its environmental stochasticity analog, referred to here as the Logistic Environmental Stochasticity (LES) model. The LES model can be written as an SDE,

$$dX_t = rX_t \left(1 - \frac{X_t}{K}\right) + \sigma X_t dB_t, \quad (3.6)$$

with B_t the standard Brownian motion process [40, 52], whose intervals are independent, Gaussian distributed variables with $\mathbb{E}[B_t] = 0$ and $\text{Var}[B_t] = t$, and σ setting the strength of the noise. Historically, there has been no obvious way of quantitatively comparing extinction risk between the two models across parameter space, since the noise parameter σ and the catastrophe parameters, a rate λ and size f , describe distinct, model-specific processes [32, 48, 55].

To circumvent this issue, I propose an approach in which the LES model is viewed not as a distinct process, but as a special case of the LRC model. This notion has been expressed qualitatively for decades [48, 55], but, to my knowledge,

has never been made explicit. This can be done using a functional generalization of the Central Limit Theorem (CLT) [49], which says that fluctuations of the Poisson process about its mean converge in distribution to Brownian motion in the limit of infinite jump rate and infinitesimal jump size. In Appendix B, it is shown that the relevant limits are

$$\ln f(N_t - \lambda t) \xrightarrow{\lambda \rightarrow \infty, f \rightarrow 1} \sqrt{\lambda} \ln f B_t, \quad (3.7)$$

such that $\sqrt{\lambda} \ln f$ is constant. Consequently, the mean drift of the scaled Poisson process diverges as $\sqrt{\lambda}$, the variance remains finite and all higher cumulants go to zero. These are functional analogs to what happens when a Poisson distribution limits to a Gaussian in the classical CLT. In this case, the diverging drift - which is proportional to effective catastrophe parameter $\lambda \ln f$ discussed above - is a manifestation of the fact that catastrophes are unidirectional, whereas noise in the LES model is bidirectional. To obtain a non-trivial limiting process, this drift must be subtracted off manually before taking limits. This subtraction can be absorbed into a rescaling of the growth rate and carrying capacity, similar to renormalization methods in theoretical physics [50], such that the final transformation from the LRC model to the LES model involves rescaling all four LRC model parameters.

The complete transformation from the LRC to LES model will be parameterized by a dimensionless scale parameter, α . The prescription is as follows. Start from an LRC model together with a target LES noise strength σ and fix $\lambda \ln^2 f = \sigma^2$. Then transform the LRC parameters according to

$$\lambda' = \alpha \lambda, \quad \ln f' = -\sigma / \sqrt{\lambda'},$$

$$r' = r \left(1 - \frac{\lambda' \ln f'}{r} \right), \quad K' = K \left(1 - \frac{\lambda' \ln f'}{r} \right). \quad (3.8)$$

It is shown analytically in Appendix B that in the limit $\alpha \rightarrow \infty$, the LRC model $LRC(r', K', \lambda', f')$ gets mapped to an LES model $LES(r_{ES}, K_{ES}, \sigma)$, with $\sigma = \lambda \ln^2 f$, $r_{ES} = r(1 + (2r)^{-1}\sigma^2)$, and $K_{ES} = K(1 + (2r)^{-1}\sigma^2)$. In this way, the stationary mean of the process without extinction remains constant throughout this transformation, fixed at K . This is chosen as a convenient way to normalize the effects of noise. By adding constant offsets, the transformation can be tuned to preserve other properties (Appendix B). This transformation is shown visually in Figure 3A, which depicts numerical results for the stationary distribution of the LRC model (in log variables for visual reasons) being transformed with α increasing on the interval $(1, 75)$ (Materials and Methods). The distribution approaches that of the target LES model, shown in green in panel (vi) .

With this transformation, the question of relative risks of extinction under the LRC model and the LES model was revisited. The mean time to extinction, τ , was computed via stochastic simulation of the LRC model for various values of α (Figure 3B, bottom), rescaling LRC model parameters according to equation (8) for each α (Materials and Methods). The LRC model extinction time (purple circles) increases with increasing α and asymptotes to the LES model extinction time (green square). Computed numerically, the stationary population mean in the absence of extinction does indeed remain constant throughout the transformation (Figure 3B, top). The conclusion is again that there exists a significantly higher risk of extinction under random catastrophe dynamics than under environmental stochasticity dynamics.

This conclusion is robust across parameter space. Plotting the beginning and end points of the curve in Figure 3B for various values of carrying capacity reproduces the asymptotic power law behavior described by Lande for simpler

models [48] (Figure 3C), though the exponents obtained by linear fitting (Materials and Methods) are smaller for the LRC model across a wide range of effective noise strengths (Figure 3D). Note that because the growth rate is rescaled in this procedure, as long as the original growth rate r is positive, the long-run growth rate [48] is positive for all values of σ . The conclusion is also insensitive to the initial starting population, x_0 , as the mean time to extinction becomes independent of x_0 above a critical threshold (see [32, 46] and Supplementary Figure 1). In addition to this method based on the diffusion limit, an alternative approach, in which the stationary means of the LRC and LES models equated simply by mapping $\sigma^2 = -2\lambda \ln f$, leads to the same conclusion (Supplementary Figure 2, Appendix C).

3.4. Discussion

This work presented new results for the Logistic Random Catastrophe (LRC) model, a model that serves both as a foundation for understanding the ecological consequences of random catastrophes and as an empirical model that describes real data [45, 46]. Exact analytic results for its stationary moments were derived using the method of moment equations. These expressions revealed that ensemble statistics are largely controlled by a single parameter that combines the average catastrophe rate and size, which is both a fundamental insight into the model’s statistical structure and a useful result for the analysis of ecological data [45]. They also revealed the similarity in structure between the LRC model and its Gaussian noise counterpart, the Logistic Environmental Stochasticity (LES) model, which was exploited to construct the latter as a limit of the former. The mean time to extinction increased monotonically along this limit by orders of magnitude in

relevant regions of parameter space, indicating higher extinction risk under random catastrophe dynamics in general.

This heightened extinction risk has implications for the prioritization of conservations efforts in the face of different types of stochasticity. In the absence of detailed information, the results derived here imply that a system subject to random catastrophes should be considered to have higher risk of extinction than a comparable system experiencing strong environmental stochasticity. Moreover, for systems subject to random catastrophes, estimates of extinction risk obtained using Gaussian noise models will likely be underestimates.

In addition, given that large fluctuations appear to be intrinsic to intestinal microbiota [42, 43, 45], the enhanced extinction risk reported here may be important for understanding the evolution of functional redundancy across symbiotic taxa and of host biochemical networks that sense fluctuating microbial products. For example, it was recently discovered that a certain zebrafish intestinal bacterial species produces a compound that triggers the expansion of beta cells in the pancreas [56] during larval development. The same bacterial species has also been shown to exhibit random catastrophe dynamics driven by peristaltic contractions [45] during this developmental period. Given these large fluctuations, the question arises as to how the biochemical pathway that mediates this interaction evolved to remain sensitive yet robust, so to ensure proper timing of development. One possibility is that the sensing system effectively computes a type of running time average on the signal to smooth out large fluctuations. The diffusion limit of random catastrophes discussed here, with its roots in the Central Limit Theorem, can viewed precisely as a kind of running average, or

coarse-graining, and so may have a direct biological realization in these types of sensing systems.

The diffusion limit method derived here is readily applied to the study of other statistics of the LRC model. It can also be easily adapted to other Markov models, including multi-species models [49, 54]. These generalizations allow for more computations, analogous to extinction times in Figure 3B, that could provide useful insight. For one example, it would be useful to revisit optimal control problems relevant for ecological management in the presence of random catastrophes, such as the harvesting strategies for fisheries considered in [57], and study how optimal policies evolve when discontinuous jumps limit to continuous environmental stochasticity. For another, evolutionary studies of bet hedging in the presence of catastrophes [58] could be directly mapped to the analogous problem in the presence of continuous noise [33], connecting ecological and evolutionary dynamics relevant for a wide variety of systems.

3.5. Materials and Methods

All code was written in MATLAB and is available at [INSERT URL](#)

3.5.1. LRC and LES model simulations

Sample paths of the differential Poisson process were generated as Bernoulli trials [52]. These paths were then used in the numerical integration of the LRC model. For all calculations except for the diffusion limit calculations in Figure 3, the logistic growth equation was integrated with the Euler method between jump times, at which the population was reduced by a factor of f . The LES model was integrated with a straightforward application of the Milstein method [59].

3.5.2. The diffusion limit

In the diffusion limit, jump sizes approach the size of deterministic growth in one numerical timestep. So, the deterministic contribution of order Δt must be retained, resulting in a more straightforward Euler-type integration scheme. In this case, an adaptive timestep is used, scaling $\Delta t' = \Delta t / \sqrt{\alpha}$, identically to $\ln f$, which sets the size of the jump. This scaling will lead to numerical artifacts when the probability of catastrophe in one timestep, $\lambda' \Delta t'$, approaches unity. Since $\lambda' = \alpha \lambda$, this will occur at $\alpha_c \sim (\lambda \Delta t)^{-2}$, and so can be put off by starting with a sufficiently small time step.

3.5.3. Extinction times

Extinction times were computed by straightforward stochastic simulation, following population trajectories from an initial population, x_0 until they reached the extinction threshold, x^* . To extract the exponent, ν , of the asymptotic relationship $\tau \sim K^\nu$, a linear fit to log-transformed variables was done for the larger half of the carrying capacity values, typically 5 data points.

3.6. Acknowledgements

I thank Raghuveer Parthasarthy, Pankaj Mehta, and David Levin for helpful feedback. Research reported in this publication was supported by the NIH as follows: by the NIGMS under award number P50GM098911 and by training grant T32 GM007759.

Appendix

.7. Detailed calculation of stationary moments

In this section an expression for the n^{th} stationary moment for the LRC model is derived. The approach is analogous for the LES model and since the results are already known [60], a detailed derivation isn't given, though one remark is made on the application of this method to diffusion processes.

.7.1. LRC model

Before beginning, the chain rule for jump processes [52] is stated without proof, for reference. Let X_t by a general process given by

$$dX_t = f(X_t, t)dt + h(X_{t^-}, t^-)dN_t \quad (.71)$$

with f and h deterministic functions, N_t a Poisson process with rate λ , and t^- denoting the Itô convention as in the main text. Further let $Y_t \equiv F(X_t, t)$ be a transformed process. Then Y_t is governed by

$$dY_t = (\partial_t F(X_t, t) + f(X_t, t)\partial_{X_t} F(X_t, t)) dt + \Delta Y_{t^-}^{\text{jump}} dN_t \quad (.72)$$

with $\Delta Y_{t^-}^{\text{jump}} \equiv F(X_{t^-} + h(X_{t^-}, t^-)) - F(X_{t^-}, t^-)$.

Now recall the LRC model,

$$dX_t = rX_t \left(1 - \frac{X_t}{K}\right) dt - (1-f)X_t dN_t. \quad (.73)$$

The first step is to change variables to X_t^n using the stochastic chain rule for jump SDEs. The result is

$$dX_t^n = nrX_t^n \left(1 - \frac{X_t}{K}\right) dt - (1 - f^n)X_t^n dN_t. \quad (.74)$$

Then, each term in this SDE is averaged. The expectation of $X_{t^-}^n dN_t$ can be factored: $\mathbb{E}[X_{t^-}^n dN_t] = \mathbb{E}[X_{t^-}^n]\mathbb{E}[dN_t] = \mathbb{E}[X_{t^-}^n]\lambda dt$. Intuitively, this is because the two processes appear mutually independent. The Poisson process has independent increments, and since the Itô convention was used, $X_{t^-}^n$ is independent of N_t , which occurs in the future. This is certainly true for a discrete time model, but care must be taken in the continuous limit.

A more rigorous argument can be made using the Dominated Convergence Theorem. The case $n = 1$ is considered without loss of generality. Consider X_j , a discrete partition of the continuous time process X_t , such that $X_j \rightarrow X_t$ in probability. Then, sums of X_j converge in probability to integrals, in particular,

$$\sum_j X_{j-1} \Delta N_j \rightarrow \int_T X_{t^-} dN_t, \quad (.75)$$

where ΔN_j is a partition of the Poisson process. The Dominated Convergence Theorem says that if X_t is dominated by an integrable function on the interval T ,

$$\mathbb{E} \left[\sum_j X_{j-1} \Delta N_m \right] \rightarrow \mathbb{E} \left[\int_T X_{t^-} dN_t \right] \quad (.76)$$

in probability. Since populations in the LRC model are bounded by the carrying capacity for all time, this is always valid. The expectation of the sum is

straightforward, leading to the result,

$$\mathbb{E} \left[\int_T X_{t^-} dN_t \right] = \int_T \mathbb{E}[X_{t^-}] \lambda dt, \quad (.77)$$

from which the infinitesimal version follows as a special case.

Factoring the expectation results in an ODE for the n^{th} moment. In the steady state, this becomes the recursion relation

$$\mathbb{E}[X^{n+1}] = K \left(1 - \frac{\lambda(1-f^n)}{nr} \right) \mathbb{E}[X^n]. \quad (.78)$$

Defining

$$c_n \equiv \left(1 - \frac{\lambda(1-f^n)}{nr} \right), \quad (.79)$$

the n^{th} moment can be expressed in terms of the mean as

$$\mathbb{E}[X^n] = K^{n-1} \left(\prod_{m=1}^{n-1} c_m \right) \mathbb{E}[X]. \quad (.710)$$

To complete the recursion relation, the mean must be computed independently. This is accomplished by changing variables to $\ln X_t$ using the chain rule for jump processes:

$$d \ln X_t = r \left(1 - \frac{X_t}{K} \right) dt + \ln f dN_t, \quad (.711)$$

which in the steady state gives an expression for the stationary mean,

$$\mathbb{E}[X] = K \left(1 + \frac{\lambda}{r} \ln f \right). \quad (.712)$$

Plugging this back into equation (A10) gives the final result

$$\mathbb{E}[X^n] = K^n \left(1 + \frac{\lambda}{r} \ln f\right) \prod_{m=1}^{n-1} \left(1 - \frac{\lambda(1-f^m)}{mr}\right). \quad (.713)$$

Evaluating this equation for $n = 2$ leads to the expression for the variance in the main text:

$$\text{Var}[X]_{LRC} = K^2 \frac{\lambda}{r} (-\ln f - (1-f)) \left(1 + \frac{\lambda}{r} \ln f\right). \quad (.714)$$

.7.2. LES model

The derivation is analogous for the LES model, except that Itô's chain rule for diffusion processes is used. Since the results are already known [60], derived with traditional methods, a detailed computation will not be given. However, one remark worth making concerns the expectation of $X_{t^-} dB_t$. The intuitive argument outlined for the LRC model - that since the Itô convention was employed the expectation of the product can be factored - gives the correct answer in this case, but is in fact not generally valid. Essentially, for processes governed by equations of the form

$$dX_t = f(X_t, t)dt + g(X_{t^-}, t^-)dB_t, \quad (.715)$$

the integral $\int g(X_{t^-}, t^-)dB_t$ can acquire non-zero expectation if the function g grows too quickly. A classic example is the CEV model of quantitative finance [61], which is of the form $f(X_t, t) = X_t$ and $g(X_t, t) = X_t^\gamma$ for $\gamma > 1$. However, one can use the fact that the exponential version of the LES model, i.e. $K \rightarrow \infty$, is a well known SDE for which $\mathbb{E} [\int X_{t^-} dB_t] = 0$. This model is known as Geometric Brownian Motion and describes asset prices in the Black-Scholes model of quantitative finance [61]. Since paths of the exponential model almost surely

dominate paths of the LES model, $\int X_{t-} dB_t$ for the LES model inherits the martingale property from the exponential case, which implies zero expectation.

Following the same procedure as for the LRC model, factoring expectations of $X_{t-}^n dB_t$, results in

$$\mathbb{E}[X^n]_{LES} = K^n \left(1 - \frac{\sigma^2}{2r}\right) \prod_{m=1}^{n-1} \left(1 + \frac{(m-1)\sigma^2}{2r}\right). \quad (.716)$$

Special cases of this include

$$\mathbb{E}[X]_{LES} = K \left(1 - \frac{\sigma^2}{2r}\right) \quad (.717)$$

and

$$\text{Var}[X]_{LES} = \frac{K^2\sigma^2}{2r} \left(1 - \frac{\sigma^2}{2r}\right). \quad (.718)$$

.8. The diffusion limit and the Central Limit Theorem

This section contains details of the construction of the LES model from the LRC model in the limit of infinitely frequent, infinitesimal catastrophes, referred to here as the diffusion limit. The complete transformation involves all four LRC model parameters and is specified as follows. Let α be a scale parameter, $LRC(r, K, \lambda, f)$ an LRC model, and σ be the target noise-strength parameter of the limiting LES model. Fix $\lambda \ln^2 f = \sigma^2$, and scale

$$\lambda' = \alpha\lambda, \quad \ln f' = -\sigma/\sqrt{\lambda'}$$

$$r' = r \left(1 - \frac{\lambda' \ln f'}{r}\right) = r \left(1 + \frac{\sigma\sqrt{\lambda}}{r}\sqrt{\alpha}\right),$$

$$K' = K \left(1 - \frac{\lambda' \ln f'}{r} \right) = K \left(1 + \frac{\sigma\sqrt{\lambda}}{r} \sqrt{\alpha} \right). \quad (.819)$$

The claim is that in taking the limit $\alpha \rightarrow \infty$, the LRC model $LRC(r', K', \lambda', f')$ gets mapped to an LES model $LES(r_{ES}, K_{ES}, \sigma)$, with $\sigma^2 = \lambda \ln^2 f$, $r_{ES} = r(1 + (2r)^{-1}\sigma^2)$, and $K_{ES} = K(1 + (2r)^{-1}\sigma^2)$, such that the stationary means of both models are equal. I first motivate the form of this transformation, which involves all four LRC model parameters, by studying the behavior of the stationary moments. I then show how the precise form of these limits, namely $\lambda \rightarrow \infty$, $f \rightarrow 1$, such that $\lambda \ln^2 f \rightarrow \text{const.}$, follows from functional generalizations of the Central Limit Theorem (CLT), in which a scaled, compensated Poisson process limits to Brownian motion. Finally, I show analytically how the full transformation maps the LRC model into the LES model.

.8.1. Motivation

As discussed in the main text, taking the limits $\lambda \rightarrow \infty$, $f \rightarrow 1$, such that $\lambda \ln f \rightarrow \text{const.}$ is analogous to the law of large numbers, leading to a deterministic limit. The correct limits instead are $\lambda \rightarrow \infty$, $f \rightarrow 1$, such that $\lambda \ln^2 f \rightarrow \text{const.}$, which I show below is analogous to the CLT. To motivate the final four parameter transformation, let us first consider the behavior of the LRC variance under these limits:

$$\begin{aligned} \text{Var}[X] &= K^2 \frac{\lambda}{r} (-\ln f - (1-f)) \left(1 + \frac{\lambda}{r} \ln f \right) \\ &\xrightarrow{\text{limits}} K^2 \frac{\lambda \ln^2 f}{2r} \left(1 + \frac{\lambda}{r} \ln f \right) \\ &= K^2 \frac{c^2}{2r} - K^2 \frac{c^3}{r^2} \sqrt{\lambda}. \end{aligned} \quad (.820)$$

with $c = \text{const} = -\sqrt{\lambda} \ln f$. In taking the limit $f \rightarrow 1$, the relation $(-\ln f - (1 - f)) \rightarrow 2^{-1} \ln^2 f$ was used, based on a 2nd order Taylor expansion.

The variance diverges, but a part of it remains finite. The finite piece of the variance in this limit is exactly the variance of an LES model with $\sigma^2 = \lambda \ln^2 f$ and increased growth parameters $K_{ES} = K(1 + (2r)^{-1}\sigma^2)$, and $r_{ES} = r(1 + (2r)^{-1}\sigma^2)$. Looking at the behavior of the mean in this limit leads to the same conclusion. This suggests that this limit does take the LRC model into an LES model, but one that is accompanied by a noise-induced drift that diverges as $\sqrt{\lambda}$. This divergence should be expected, as it reflects the unidirectionality of jumps in the LRC model, which is absent in the LES, analogous to the divergence of the mean of a Poisson distribution when it limits to a Gaussian. To obtain a non-trivial limiting process, this drift needs to be subtracted off, for example, by adding a term $-\lambda \ln f dt$ to the LRC model SDE. This is equivalent to rescaling the growth rate and carrying capacity each by a factor of $(1 - r^{-1}\lambda \ln f)$, leading to the full four parameter transformation.

.8.2. Functional Central Limit Theorems

The form of the limits $\lambda \rightarrow \infty$, $f \rightarrow 1$, such that $\lambda \ln^2 f \rightarrow \text{const.}$, is a direct consequence of the CLT. The classical CLT says that given a set of n random variables, $\{\xi_j\}$, that are identically and independently distributed (i.i.d.) with mean μ and finite variance σ^2 , the sum of the deviations of these variables from their mean, when rescaled by \sqrt{n} , tends in distribution to a Gaussian variable as $n \rightarrow \infty$:

$$\lim_{n \rightarrow \infty} \frac{\sum_j \xi_j - n\mu}{\sqrt{n}} = \eta \sim \mathcal{N}(0, \sigma^2) \quad (.821)$$

where $\mathcal{N}(\mu, \sigma^2)$ is a Gaussian distribution with mean μ and variance σ^2 . The condition that the variables ξ_j follow identical distributions can be relaxed, but we focus on this restricted case here.

A vast body of mathematical literature concerns the construction of generalization of the CLT to stochastic processes. One important generalization, which we will employ in the study of the Poisson process, is Donsker's theorem [49]. Donsker's theorem dictates the limit of a sequence of stochastic process, $X_t^{(n)}$, constructed from sums of i.i.d. random variables $\tilde{\xi}_j$ with zero mean and finite variance via

$$X_t^{(n)} \equiv \frac{1}{\sqrt{n}} \sum_{j=1}^{[ns]} \tilde{\xi}_j, \quad ns \equiv t. \quad (.822)$$

Here we have introduced time as multiples of a unit s , such that $t = ns$, and [...] denotes the integer part. Donsker's theorem says that as $n \rightarrow \infty$ with $s \rightarrow 0$ such that $ns \rightarrow t$ for arbitrary t , the processes $X_t^{(n)}$ converge in law to Brownian motion,

$$X_t^{(n)} \rightarrow B_t. \quad (.823)$$

Donsker's theorem can be used to show the convergence of the compensated Poisson process to Brownian motion in particular limits. The idea is to write the Poisson process as a sum of intervals which themselves are i.i.d. random variables that meet the criteria for Donsker's theorem, and then scale the jump size and rate in the ways that map onto the $n \rightarrow \infty$ limit. This approach is based on a method known as finite dimensional convergence, which is only applicable to processes with independent increments [49].

Consider breaking a scaled, compensated Poisson process, $\epsilon \tilde{N}_t$ into a sum of finite intervals,

$$\epsilon \tilde{N}_t = \epsilon \sum_{j=1}^{[ns]} \Delta \tilde{N}_j. \quad (.824)$$

From inspection, we see that the appropriate mapping is $\lambda \rightarrow n\lambda$, $\epsilon = \sigma \lambda^{-1/2}$, in which case

$$\epsilon \tilde{N}_t = \sigma \sum_{j=1}^{[ns]} \frac{\Delta \tilde{N}_j / \sqrt{\lambda}}{\sqrt{n}}. \quad (.825)$$

Donsker's theorem can then be applied with $\tilde{\xi}_j \equiv \Delta \tilde{N}_j / \sqrt{\lambda}$, resulting in

$$\epsilon \tilde{N}_t \xrightarrow{\lambda \rightarrow \infty, \epsilon \rightarrow 0} \sqrt{\lambda} \epsilon B_t. \quad (.826)$$

In the LRC model, collapse size is forced to zero by taking $f \rightarrow 1$. This still leaves room for how exactly λ and f should map on to σ . One choice would be to take $\epsilon = -(1 - f)$, such that $\sigma^2 = \lambda(1 - f)^2$. In this case, a quick calculation shows that the limiting process would be an LES model with unchanged growth parameters, (r, K) , and consequently a reduced stationary mean of $K(1 - (2r)^{-1}\sigma^2)$, whereas the original LRC process, after removing the divergence of $\lambda \ln f$, has a stationary mean of K . Alternatively, one could take $\epsilon = \ln f$, such that $\sigma^2 = \lambda \ln^2 f$. This is the case examined above, which results in an LES model with an unchanged stationary mean, but altered growth parameters. Since our present goal is to normalize the effect of noise to construct a fair comparison of extinction risk, the latter choice is more appropriate.

.8.3. Convergence of LRC to LES

I now discuss the convergence of the LRC model to the LES model via the convergence of the Poisson process to Brownian motion discussed above. General conditions for the convergence of a pure jump Markov process to a diffusion are given in [49]. Rather than verify these general conditions here, I'll take a more intuitive approach that exploits the simplicity of the present models and uses the fact that both the LRC model and the LES model possess unique, strong solutions, as follows from special cases of a general result derived in [54]. This allows us to uniquely define a sequence of processes $X'_t(\alpha) \equiv F[\tilde{N}_t(\alpha); r(\alpha), K(\alpha), \lambda(\alpha), f(\alpha)]$, where F is the solution to the LRC model depending on parameters r , K , λ , and f , and the limit of the sequence $X_t^* \equiv \lim_{\alpha \rightarrow \infty} X'_t(\alpha)$. Existence and uniqueness of solutions to both models allows us in principle to take the limit and then invert the solution, recovering a diffusion SDE. In practice, we can take the limit directly in the context of the LRC model SDE. To begin, recall the LRC model,

$$dX_t = rX_t \left(1 - \frac{X_t}{K}\right) dt - (1-f)X_t dN_t. \quad (.827)$$

Let us expand $(1-f)$ in powers of $\ln f$ to second order and write the Poisson process in terms of its mean and compensated process.

$$dX_t = rX_t \left(1 - \frac{X_t}{K}\right) dt + \left(\ln f + \frac{1}{2} \ln^2 f\right) X_t \lambda dt + \left(\ln f + \frac{1}{2} \ln^2 f\right) X_t^- d\tilde{N}_t + \mathcal{O}(\lambda \ln^3 f) \quad (.828)$$

Now let us absorb the mean drift of the Poisson process as scaling factors for the growth rate and carrying capacity

$$dX_t = r \left(1 + \frac{\lambda}{r} \ln f + \frac{\lambda}{2r} \ln^2 f \right) X_t \left(1 + \frac{X_t}{K(1 - \frac{\lambda}{r} \ln f + \frac{\lambda}{2r} \ln^2 f)} \right) dt \\ + \left(\ln f + \frac{1}{2} \ln^2 f \right) X_{t-} d\tilde{N}_t + \mathcal{O}(\lambda \ln^3 f). \quad (.829)$$

Now we apply the transformation [19] with α finite and evaluate r' in terms of r and K' in terms of K . This has the effect of canceling all $\lambda \ln f$ terms, as intended.

$$dX'_t(\alpha) = r \left(1 + \frac{\lambda'}{2r} \ln^2 f' \right) X'_t \left(1 - \frac{X'_t}{K(1 + \frac{\lambda'}{2r} \ln^2 f')} \right) dt \\ + \left(\ln f' + \frac{1}{2} \ln^2 f' \right) X'_{t-} d\tilde{N}'_t + \mathcal{O}(\lambda \ln^3 f) \quad (.830)$$

where primed variables depend on α . Before taking the $\alpha \rightarrow \infty$ limit, we can identify $\lambda' \ln^2 f'$ as σ^2 , a finite constant independent of α ,

$$dX'_t(\alpha) = r \left(1 + \frac{\sigma^2}{2r} \right) X'_t \left(1 - \frac{X'_t}{K(1 + \frac{\sigma^2}{2r})} \right) dt + \left(\ln f' + \frac{1}{2} \ln^2 f' \right) X'_{t-} d\tilde{N}'_t + \mathcal{O}(\lambda \ln^3 f). \quad (.831)$$

We can now evaluate the $\alpha \rightarrow \infty$ limit, knowing how \tilde{N}_t transforms: $\ln f' d\tilde{N}_t \rightarrow \sigma dB_t$ in law, $\ln^2 f' d\tilde{N}_t \rightarrow 0$, resulting in

$$\lim_{\alpha \rightarrow \infty} dX'_t(\alpha) = dX_t^* = r \left(1 + \frac{\sigma^2}{2r} \right) X_t^* \left(1 - \frac{X_t^*}{K(1 + \frac{\sigma^2}{2r})} \right) dt + \sigma X_{t-}^* dB_t. \quad (.832)$$

The limiting process is an LES model with increased growth parameters $r_{LES} = r(1 + (2r)^{-1}\sigma^2)$ and $K_{LES} = K(1 + (2r)^{-1}\sigma^2)$. Comparing this model to the transformed LRC model of [31] using the analytic results for the stationary mean equations (A12) and (A17) reveals that the two models do indeed have the same stationary mean.

.9. An alternative mapping that equates stationary means

The stationary means of the LRC and LES models can also be equated by using the same growth rate and carrying capacities and mapping $\sigma^2 = -2\lambda \ln f$, as is clear from equations (A12) and (A17). This mapping provides an alternative method of quantitatively comparing the two models, though one that is perhaps less meaningful than the diffusion limit approach. It can be understood intuitively by plotting the time evolution of the mean population of both models in the presence and absence of extinction (Supplementary Figure 2A). In the absence of extinction, both models asymptote to the same value. In the presence of extinction, the LRC model average decays to zero faster than the LES model average, indicating higher extinction risk. Computed directly, the mean times to extinction for the LRC model are significantly shorter than for the LES model (Supplementary Figure 2B), supporting the conclusions of the diffusion limit-based method.

REFERENCES CITED

- [31] Richard Levins. *Evolution in changing environments: some theoretical explorations*. Princeton University Press, 1968.
- [32] Russell Lande, Steiner Engen, and Bernt-Erik Saether. *Stochastic Population Dynamics in Ecology and Conservation*. Oxford University Press, 2003.
- [33] Anna Melbinger and Massimo Vergassola. The impact of environmental fluctuations on evolutionary fitness functions. *Scientific Reports*, 5(15211), 2015.
- [34] Charles K Fisher and Pankaj Mehta. The transition between the niche and neutral regimes in ecology. *Proceedings of the National Academy of Sciences*, 111(36):13111–13116, 2014.
- [35] Alan Hastings. Timescales and the management of ecological systems. *Proceedings of the National Academy of Sciences*, 113(51):14568–14573, 2016.
- [36] John R Beddington and Robert M May. Harvesting natural populations in a randomly fluctuating environment. *Science*, 197(4302):463–465, 1977.
- [37] Milner B Schaefer. A study of the dynamics of the fishery for yellowfin tuna in the eastern tropical pacific ocean. *Inter-American Tropical Tuna Commission Bulletin*, 2(6):243–285, 1957.
- [38] Russell Lande, Steinar Engen, and Bernt-Erik Saether. Optimal harvesting of fluctuating populations with a risk of extinction. *The American Naturalist*, 145(5):728–745, 1995.
- [39] Benjamin Dickens, Charles K Fisher, and Pankaj Mehta. Analytically tractable model for community ecology with many species. *Physical Review E*, 94(2):022423, 2016.
- [40] Samuel Karlin and Howard E Taylor. *A Second Course in Stochastic Processes*. Elsevier, 1981.
- [41] Andrew J Pershing, Michael A Alexander, Christina M Hernandez, Lisa A Kerr, Arnault Le Bris, Katherine E Mills, Janet A Nye, Nicholas R Record, Hillary A Scannell, James D Scott, et al. Slow adaptation in the face of rapid warming leads to collapse of the gulf of maine cod fishery. *Science*, 350(6262):809–812, 2015.

- [42] Pål Trosvik, Eric Jacques De Muinck, and Nils Christian Stenseth. Biotic interactions and temporal dynamics of the human gastrointestinal microbiota. *The ISME journal*, 9(3):533–541, 2015.
- [43] J Gregory Caporaso, Christian L Lauber, Elizabeth K Costello, Donna Berg-Lyons, Antonio Gonzalez, Jesse Stombaugh, Dan Knights, Paweł Gajer, Jacques Ravel, Noah Fierer, et al. Moving pictures of the human microbiome. *Genome Biology*, 12(5):R50, 2011.
- [44] Les Dethlefsen and David A. Relman. Incomplete recovery and individualized responses of the human distal gut microbiota to repeated antibiotic perturbation. *Proceedings of the National Academy of Science*, 108, 2011.
- [45] Travis J Wiles, Matthew Jemielita, Ryan P Baker, Brandon H Schlomann, Savannah L Logan, Julia Ganz, Ellie Melancon, Judith S Eisen, Karen Guillemain, and Raghuveer Parthasarathy. Host gut motility promotes competitive exclusion within a model intestinal microbiota. *PLOS Biology*, 2016.
- [46] Floyd B. Hanson and Henry C. Tuckwell. Logistic growth with random density independent disasters. *Theoretical Population Biology*, 19(1):1–18, 1981.
- [47] DCC Bover. Moment equation methods for nonlinear stochastic systems. *Journal of Mathematical Analysis and Applications*, 65(2):306–320, 1978.
- [48] Russel Lande. Risks of population extinction from demographic and environmental stochasticity and random catastrophes. *American Naturalist*, pages 911–927, 1993.
- [49] Jean Jacod and Albert N Shiryaev. *Limit theorems for stochastic processes*, volume 288. Springer Science & Business Media, 2013.
- [50] Michael E Peskin and Daniel V Schroeder. Quantum field theory. *The Advanced Book Program, Perseus Books Reading, Massachusetts*, 1995.
- [51] G Jona-Lasinio. The renormalization group: A probabilistic view. *Il Nuovo Cimento B (1971-1996)*, 26(1):99–119, 1975.
- [52] Floyd B. Hanson. *Applied Stochastic Processes and Control for Jump-Diffusions: Modeling, Analysis, and Computation*. Cambridge University Press, 2007.
- [53] DS Broca. Cumulant-moment relations through determinants. *International Journal of Mathematical Education in Science and Technology*, 35(6):917–921, 2004.

- [54] Jianhai Bao, Xuerong Mao, Geroge Yin, and Chenggui Yuan. Competitive lotka–volterra population dynamics with jumps. *Nonlinear Analysis: Theory, Methods & Applications*, 74(17):6601–6616, 2011.
- [55] Mark Shaffer. Minimum population sizes for species conservation. *BioScience*, 31(2):131–134, 1981.
- [56] Jennifer Hampton Hill, Eric A Franzosa, Curtis Huttenhower, and Karen Gillemain. A conserved bacterial protein induces pancreatic beta cell expansion during zebrafish development. *Elife*, 5, 2016.
- [57] Floyd B Hanson and Dennis Ryan. Optimal harvesting with both population and price dynamics. *Mathematical Biosciences*, 148(2):129–146, 1998.
- [58] Paolo Visco, Rosalind J Allen, Satya N Majumdar, and Martin R Evans. Switching and growth for microbial populations in catastrophic responsive environments. *Biophysical Journal*, 98(7):1099–1108, 2010.
- [59] GN Mil’shtejn. Approximate integration of stochastic differential equations. *Theory of Probability & Its Applications*, 19(3):557–562, 1975.
- [60] Ola H. Diserud, Steinar Engen, and Associate Editor: Peter J. Morin. A general and dynamic species abundance model, embracing the lognormal and the gamma models. *The American Naturalist*, 155(4):497–511, 2000.
- [61] Vadim Linetsky and Rafael Mendoza. Constant elasticity of variance (cev) diffusion model. *Encyclopedia of Quantitative Finance*, 2010.

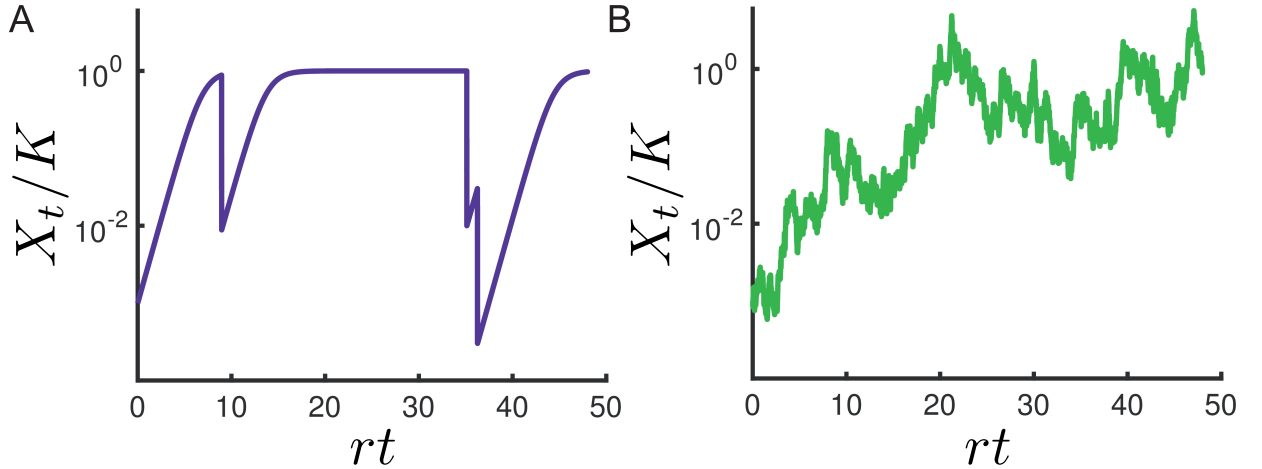


FIGURE .1. **Sample paths of LRC and LES models.** **A:** A sample path from the LRC model. Simulation parameters: $r = 1$, $K = 10^4$, $\lambda = .07$, $f = 10^{-2}$, $dt = .01$. **B:** A sample path from the LES model. Simulation parameters: $r = 1$, $K = 10^4$, $\sigma = .53$, $dt = .01$.

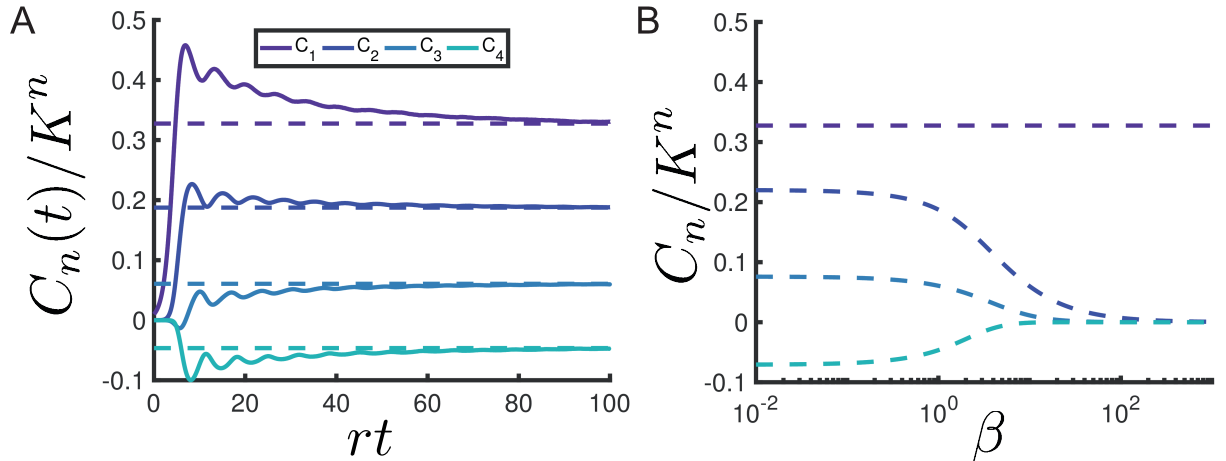


FIGURE .2. **Analytic results reveal statistical structure of LRC model.** **A:** Analytic results for stationary cumulants agree with numerical simulations. Time evolution of the first 4 cumulants, C_n , of the LRC model, computed numerically (solid lines). Dashed lines indicate the asymptotic values predicted by the analytic results, with the cumulants computed from the moments given by equation (3). Parameters: $r = 1$, $K = 10^4$, $\lambda = .1$, $f = .0012$, $dt = .01$, $N_{trials} = 5 \cdot 10^5$. **B:** Range of validity of $\lambda \ln f$ as an effective catastrophe parameter. Parameters were scaled according to $\lambda' = \beta \lambda$ and $\ln f' = \beta^{-1} \ln f$ by dimensionless scale factor β . Dashed lines are analytic results for first 4 stationary cumulants as a function of β . Parameters same as in A.

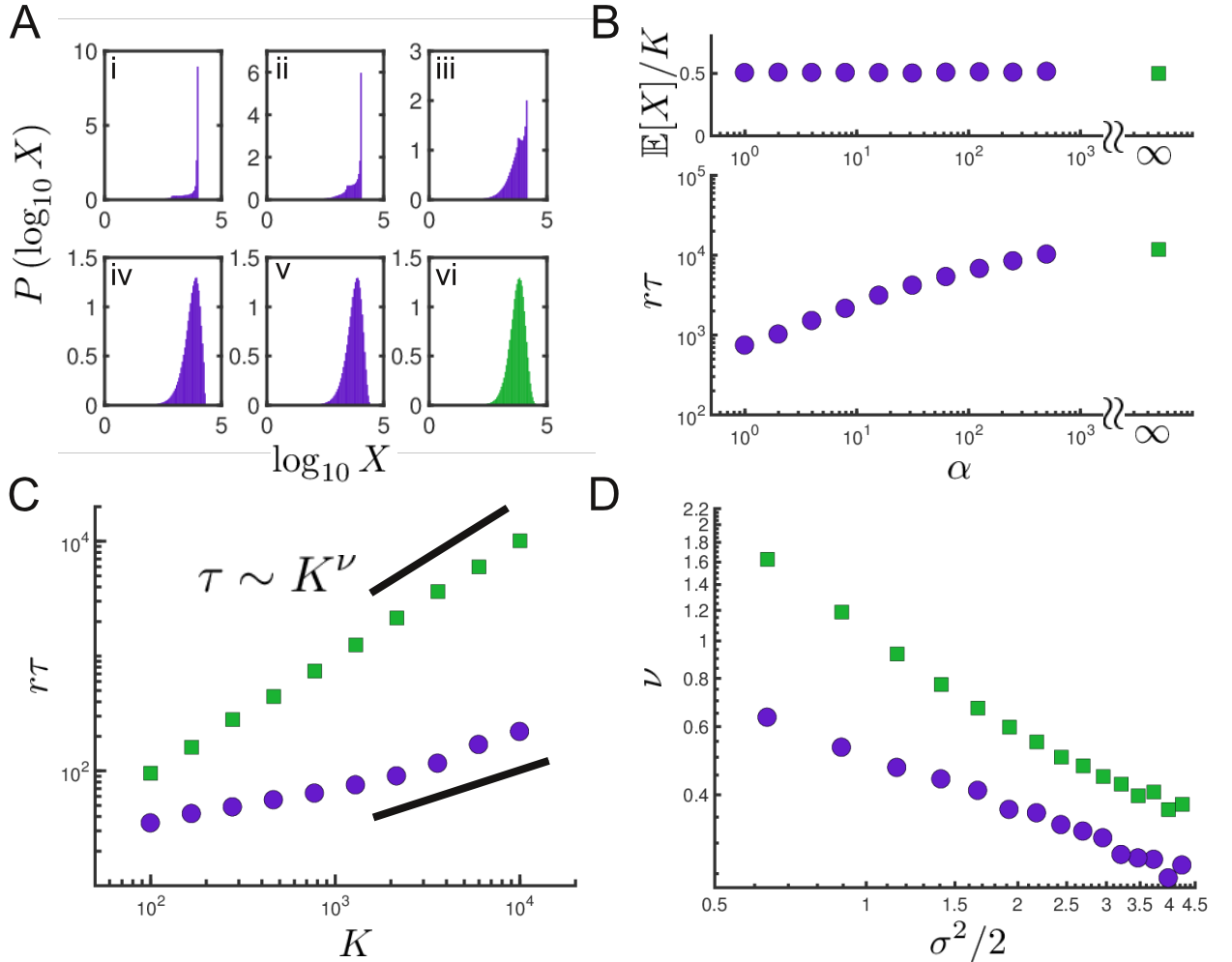


FIGURE .3. The diffusion limit and extinction times. **A:** Smoothly transforming the stationary distribution of LRC model to that of LES model in the diffusion limit. LRC model (no extinction) was simulated for $T_{max} = 300$ units of inverse growth rate for 5 values of the scale parameter α , rescaling parameters according to equation (8). Frames i-v depict the stationary distribution of $\log X$ (for visual clarity) for $\alpha = 1, 2.94, 8.66, 25.49, 75.00$ respectively, estimated from 10^6 paths. Frame vi depicts the stationary distribution of $\log X$ for the target LES model. Parameters: $r = .68$, $K = 6800$, $\lambda = .1$, $\sigma = .8$, $\ln f = -\sigma/\sqrt{\lambda}$, $dt = .01$. **B:** Mean time to extinction increases as the LRC model is morphed into the LES model (bottom), despite the stationary mean remaining constant throughout the transformation (top). Parameters: Same as in A but α ranges logarithmically from 1 to 500 and $\sigma = 1$. **C:** Mean times to extinction for the beginning (purple circles) and end (green squares) points of the diffusion limit as a function of carrying capacity. Parameters: $r = 1$, $\lambda = .1$, $f = .01$, $N_{trials} = 5000$, $x_0 = 10$, $x^* = 1$. For LES endpoints, $\sigma^2 = \lambda \ln^2 f$. **D:** The exponent of this power law, obtained by linear regression, as a function of effective noise strengths. Parameters: $r = 1$, $f = .01$, $N_{trials} = 5000$, λ is varied from 0.06 to 0.4. For each value of λ , τ vs K is computed for 10 values of K ranging from 100 to 10000. The last 5 values are used to compute ν . For the LRC model, the x-axis corresponds to $\sigma^2 = \lambda \ln^2 f$. The exponent appears to asymptotically follow a power law in σ^2 , consistent with [48]

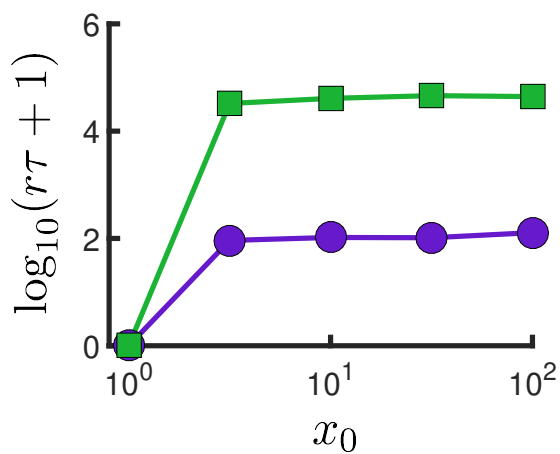


FIGURE S1. Mean time to extinction is largely independent of initial starting population. Mean time to extinction, τ , plotted on a shifted log scale as a function of initial starting population, x_0 . Green squares denote the LES model, purple circles denote the LRC model. The mean extinction time, defined as the first hitting time to $x^* = 1$, starts from 0 but rapidly increases to a value independent of x_0 . Parameters: $r = 1$, $K = 10^4$, $\lambda = .1$, $f = .01$, $N_{trials} = 500$.

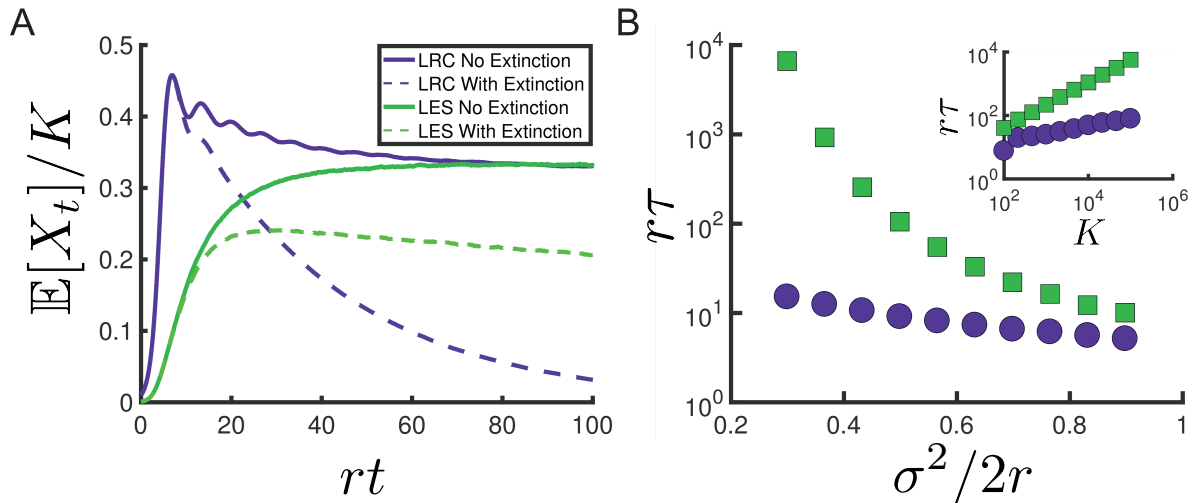


FIGURE S2. The LRC model has higher extinction risk than the LES model for equivalent stationary means. A: Illustration of the mapping.

Numerical results for the average population plotted over time in the LRC (purple) and LES (green) models, showing both the cases of no extinction (dark solid lines) and extinction (light dashed lines) via an absorbing state at $x^* = 1$. LES model has the same growth rate and carrying capacity as the LRC model and σ is determined by $\sigma^2 = -2\lambda \ln f$, such that the two models have equal stationary means (Appendix C). Parameters: $r = 1$, $K = 10^4$, $\lambda = .1$, $f = .0012$, $\sigma = 1.16$, $dt = .01$, $N_{trials} = 5 \cdot 10^5$. **B:** Mean time to extinction, τ , in units of inverse growth rate, for LRC (purple circles) and LES (green squares) models as a function of noise strength, with $\sigma^2 = -2\lambda \ln f$. Parameters: $r = 1$, $dt = .01$, $N_{trials} = 5 \cdot 10^3$. For LRC model, $f = .01$ and λ was varied from .065 to .195. Inset: Mean time to extinction as a function of carrying capacity. Parameters: $r = 1$, $\lambda = .13$, $f = .01$, $\sigma = 1.09$, $dt = .01$, $N_{trials} = 5 \cdot 10^3$.

APPENDIX A

SUBLETHAL ANTIBIOTICS COLLAPSE GUT BACTERIAL POPULATIONS BY ENHANCING AGGREGATION AND EXPULSION

Antibiotics induce large and highly variable changes in the intestinal microbiome even at sublethal concentrations, through mechanisms that remain elusive. Using gnotobiotic zebrafish, which allow high-resolution examination of microbial dynamics, we found that sublethal doses of the common antibiotic ciprofloxacin cause severe drops in bacterial abundance. Contrary to conventional views of antimicrobial tolerance, disruption was more pronounced for slow-growing, aggregated bacteria than for fast-growing, planktonic species. Live imaging revealed that antibiotic treatment promoted bacterial aggregation and increased susceptibility to intestinal expulsion. Intestinal mechanics therefore amplify the effects of antibiotics on resident bacteria. Microbial dynamics are captured by a biophysical model that connects antibiotic-induced collapses to gelation phase transitions in soft materials, providing a framework for predicting the impact of antibiotics on the intestinal microbiome.

Introduction

Antibiotic drugs induce large, long-lasting, and disease-associated alterations in the composition of the intestinal microbiota [62, 63, 64]. Even at concentrations well below the minimum inhibitory levels of many bacteria, antibiotics can lead to major and highly variable changes in the gut microbiome through mechanisms that remain mysterious [63, 64, 65]. Sublethal antibiotics can also significantly alter animal physiology; the intentional growth enhancement of livestock is a well-known

example that may involve microbiome-mediated pathways [63]. Low concentrations of antibiotics are often present in the environment as byproducts of unchecked agricultural and biomedical use, generating public health concerns associated with the emergence of drug resistance [66] as well as more direct impacts on human health [67]. It is therefore crucial to uncover mechanisms by which sublethal antibiotics reshape resident gut microbial communities. Understanding why particular bacterial strains are resilient or susceptible to antibiotic perturbations may allow us to predict the consequences of environmental contamination and may enable tailoring of antibiotic treatments as a therapeutic tool for manipulating the intestinal microbiome.

Conventional wisdom regarding bacterial responses to antibiotic drugs, derived largely from *in vitro* assays, holds that drug tolerance is facilitated by low growth rates and biofilm formation [68, 69]. Recent work suggests that microbes in the vertebrate gastrointestinal tract adopt a variety of growth and aggregation phenotypes [70, 71, 72, 73], raising the question of whether antibiotic susceptibility in the gut bears the same relationship to kinetics and physical structure as in less dynamic environments, or whether the strong mechanical activity and large fluid flows present in the intestine [74] lead to fundamentally different rules.

To investigate the *in vivo* response of gut bacteria to low-dose antibiotic exposure, especially the relationship between susceptibility and bacterial behavior, we conducted live imaging-based studies of larval zebrafish (Fig. 1A, 1B), spanning the entire intestinal volume with spatial and temporal resolutions not attainable in humans or other model vertebrates. We focused our study on two native zebrafish bacterial isolates, both frequently found in the intestine [75], that we identified as representing extremes of growth and aggregation phenotypes [71].

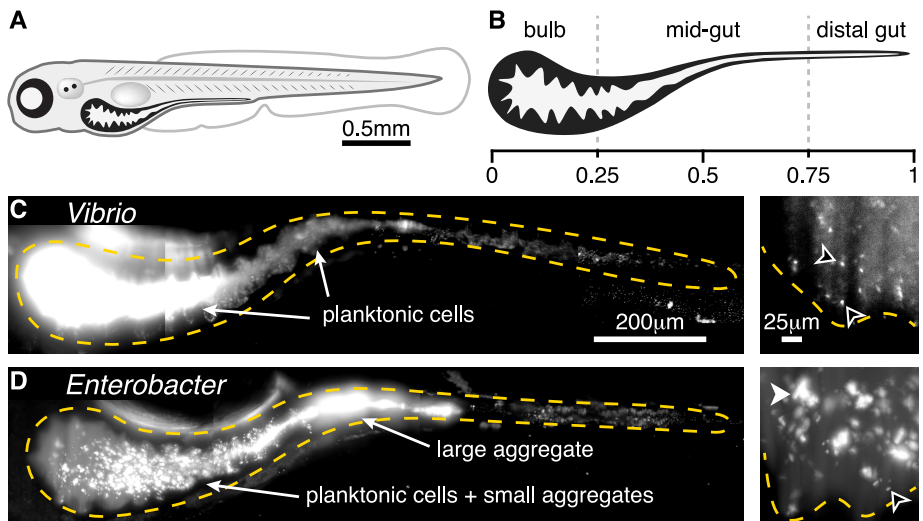


FIGURE S2. Two bacterial species show different extremes of in vivo aggregation phenotypes. A: Schematic of a zebrafish 5 days post-fertilization (dpf). B: Schematic of the larval zebrafish intestine with numbers denoting approximate fraction of gut length. C: *Vibrio cholerae* ZWU0020 *in vivo*. Left: a maximum intensity projection of a three-dimensional image of the full gut. Dense, bright bacteria and dimmer intestinal autofluorescence are evident. The orange dashed curve indicates a coarse outline of the gut boundary. Scale bar: 200 μm . Right: a single optical plane within the anterior bulb in a fish colonized with 1:100 green fluorescent protein (GFP): dTomato (dTOMO)-expressing *Vibrio*, with the GFP channel shown to highlight individual microbes in the dense swarm. The orange dashed curve indicates the approximate contour of the intestinal epithelium. Black arrowheads indicate examples of single planktonic cells. Scale bar: 25 μm . (See also SI Movie 1) D: *Enterobacter cloacae* ZOR0014 *in vivo*, shown as a maximum intensity projection of the full gut (left) and a subset of the same projection in the anterior bulb (right); bacterial aggregates are evident. The black arrowhead indicates an example of a single planktonic cell; the white arrowhead indicates an example of a multicellular aggregate. Scale bars same as in (C).

The first, *Vibrio cholerae* ZWU0020, hereafter referred to as “*Vibrio*”, exists in the larval zebrafish intestine primarily as dense populations of highly motile and planktonic individuals (Fig. 1C, SI Movie 1). *Vibrio* grows rapidly, with an in vivo doubling time of approximately 1 hour (exponential growth rate of 0.8 ± 0.3 1/hr) [76]. The second, *Enterobacter cloacae* ZOR0014, hereafter referred to as “*Enterobacter*” primarily forms large, dense bacterial aggregates with small sub-populations of non-motile planktonic cells (Fig. 1D, SI Movie 2) [77] and has an in vivo doubling time of approximately 2.5 hours (exponential growth rate of 0.27 ± 0.05 1/hr) (SI Appendix, Fig. S1). To delineate and quantify antibiotic responses independent of inter-bacterial competition, we studied *Vibrio* and *Enterobacter* separately in hosts that were initially raised germ-free (Materials and Methods). We assessed response dynamics of each bacterial population after treatment with the antibiotic ciprofloxacin, a broad spectrum fluoroquinolone that interferes with DNA replication by inhibiting DNA gyrase. Ciprofloxacin is widely administered therapeutically and has been used as a model antibiotic in studies of human microbiome disruption [78]. Furthermore, ciprofloxacin is often detected in environmental samples at ng/ml concentrations that are sublethal but capable of perturbing bacterial physiology [79, 80].

As detailed below, we discovered that sublethal levels of ciprofloxacin lead to major reductions in intestinal abundance of both *Vibrio* and *Enterobacter* that could not be predicted from in vitro responses alone. In contrast to conventional wisdom, the slow-growing and highly aggregated *Enterobacter* was impacted far more severely than the fast-growing, planktonic *Vibrio*. Changes in bacterial abundances were driven primarily by clearance from the intestine by peristaltic-like fluid flow, which impacts aggregated bacteria more severely than planktonic

cells. Exposure to sublethal levels of ciprofloxacin shifted both species to a more aggregated state, but for *Enterobacter* this state was unsustainable and led to population collapse and extinction. Quantitative image-derived population data motivate and are well fit by physical models originally used to describe colloidal growth and polymer gelation, implying an antibiotic-induced phase transition in bacterial community physical structure and revealing a general framework for understanding and predicting intestinal antibiotic perturbations.

Results

Low-dose ciprofloxacin increases bacterial aggregation and intestinal expulsion

For both *Vibrio* and *Enterobacter*, we empirically determined a ciprofloxacin dosage that induced clear changes in bacterial physiology and behavior *in vitro*, but that was below the apparent minimum inhibitory concentration. We first describe results of antibiotic exposure, *in vitro* and *in vivo*, for the *Vibrio* species.

From an initial survey of dose-response in rich media, we identified 10 ng/mL ciprofloxacin as an appropriate exposure for *Vibrio* populations. Growth of *Vibrio* in lysogeny broth in the presence of 1 ng/ml ciprofloxacin closely resembles that of the untreated control, while a concentration of 100 ng/ml is largely inhibitory (SI Appendix, Fig. S2A). An intermediate concentration of 10 ng/ml leads to a stable, intermediate optical density. Viability staining (Materials and Methods) after 6 hours of incubation with 10 ng/ml ciprofloxacin identifies 30–80% of cells as alive (SI Appendix, Fig. S3A and S3B), again consistent with this antibiotic concentration being sufficient to perturb the bacterial population without overwhelming lethality. Growth in the presence of 10 ng/ml ciprofloxacin induces marked changes in cell morphology and motility: treated cells exhibit filamentation,

making them considerably longer (mean \pm std. dev. $5.3 \pm 3.1 \mu\text{m}$) than untreated *Vibrio* ($2.9 \pm 0.9 \mu\text{m}$) (SI Appendix, Fig. S2B). Swimming speed was also reduced compared to untreated cells (mean \pm std. dev. $11.4 \pm 7.2 \mu\text{m/s}$, untreated $16.9 \pm 11.1 \mu\text{m/s}$) (SI Appendix, Fig. S2C, SI Movies 3 and 4). We note also that 10 ng/ml ciprofloxacin is comparable to levels commonly measured in environmental samples [79].

While useful for illuminating the appropriate sub-lethal concentration to further examine, experiments in rich media conditions are not an optimal assay for comparison of in vitro and in vivo antibiotic treatments, as the chemical environments are likely very dissimilar. We therefore assessed effects of ciprofloxacin on bacterial populations in the aqueous environments of the flasks housing the larval zebrafish in comparison to populations in the intestines. In the flask water, as in the intestine, the only nutrients are fish-derived. Oxygen levels are comparable to those in the larval gut, due to fast diffusion and the animals' small size. Bacteria in flask water therefore constitute a useful baseline against which to compare antibiotic impacts on intestinal populations.

Vibrio was associated with germ-free zebrafish at 4 days post-fertilization (dpf) by inoculation of the aqueous environment at a density of 10^6 cells/ml (Materials and Methods) and allowed to colonize for 24 hours, which based on previous studies provides ample time for the bacterial population to reach its carrying capacity of approximately 10^5 cells/gut [76]. Animals and their resident *Vibrio* populations were then immersed in 10 ng/ml ciprofloxacin for 24 or 48 hours, or left untreated (Fig. 2A and 2B). *Vibrio* abundances in the gut were assayed by gut dissection and plating to measure colony forming units (CFUs) (Materials and Methods). Abundances in the flask water were similarly assayed

by plating. We quantified the effect of the antibiotic treatment by computing the ratio of bacterial abundances in the treated and untreated cases, resulting in a normalized abundance (Fig. 2C). After a 24 hour treatment, \log_{10} -transformed abundances in the flask water dropped by 0.98 ± 0.4 (mean \pm std. dev.) compared to untreated controls, or one order of magnitude on average. In contrast, \log_{10} -transformed intestinal abundances showed a more severe reduction of 1.75 ± 0.88 (Fig. 2C), or a factor of approximately 60 on average, suggesting that the intestinal environment amplifies the severity of ciprofloxacin treatment. For the 48 hour treatment, the declines in flask water and intestinal abundances were similarly severe (Fig. 2C). In terms of absolute abundances, pooled data from 24 and 48 hour treatments gives a mean \pm std. dev. of the \log_{10} -transformed *Vibrio* population of 3.1 ± 0.9 ($n = 40$), compared to 4.9 ± 0.5 ($n = 42$) for untreated specimens (Fig. 2D). Unpooled data are similar (SI Appendix, Fig. S3E, S3F).

To assess the possibility that the intestine makes *Vibrio* more susceptible to ciprofloxacin-induced cell death, we embedded larval zebrafish in a 0.5% agarose gel, which allowed collection of expelled bacteria. After staining expelled bacterial cells with the viability dyes SYTO9 and propidium iodide, we imaged ejected material. We found no detectable difference between ciprofloxacin-treated and untreated populations (Fig. 2F, insets). Similarly sizeable fractions of viable and non-viable cells are evident in both ciprofloxacin-treated and untreated populations; however, co-staining of zebrafish host cells hindered exact quantification (SI Appendix, Fig. S4). This result suggests that the ciprofloxacin-induced population decline observed *in vivo* occurs independent of overt cell death and is a consequence of the response of living bacteria to the intestinal environment. We further note that the dose-response of the intestinal *Vibrio* abundance (SI Appendix, Fig. S5)

mirrors the dose-response of the in vitro growth rate, implying that the larval gut does not significantly alter or concentrate ciprofloxacin. This is also consistent with the widespread use of zebrafish larvae as a pharmacological screening platform, as water soluble chemicals readily enter and leave the animal [81, 82].

To investigate the causes of ciprofloxacin's disproportionately large impact on in vivo bacterial abundance, we used light sheet fluorescence microscopy to directly monitor *Vibrio* populations within the intestine over several hours as they responded to antibiotic exposure. Three-dimensional time-lapse imaging revealed that within hours of ciprofloxacin treatment, large numbers of bacteria became depleted from the anterior-localized planktonic and motile population (SI Movies 5 and 10). Cells were instead found in the mid and distal regions of the gut, where they appeared to be condensed into large multicellular aggregates prior to being expelled from the gut altogether (SI Movies 5 and 11). After 10 hours of exposure, *Vibrio* populations in ciprofloxacin-treated hosts contained large, 3D aggregates localized to the posterior of the intestine, a feature not observed in untreated controls (Fig. 2E and 2F) nor in all previous characterizations of this strain [71, 76]. We note also that in vitro, antibiotic-treated *Vibrio* does not form large aggregates (SI Appendix, Fig. S3 and S6, SI Movie 4)

To determine whether the bacterial aggregation observed in vivo stems from a fundamentally different response to antibiotics at the single-cell level or different large-scale consequences of similar cell-level response, we generated in *Vibrio* a genetically encoded fluorescent reporter of the SOS pathway (SI Appendix, Fig. S7, Materials and Methods), a DNA damage repair pathway induced by genotoxic agents such as ciprofloxacin [83, 84]. Genes in the SOS regulon halt replication and enable DNA repair, and also affect motility and biofilm formation [80, 85]. In

vitro, we found that treatment with 10 ng/ml ciprofloxacin strongly induced *recN*-based SOS reporter activity, with a heterogeneous response across individual cells (SI Appendix, Fig. S3C and S3D). Within the intestine, SOS reporter activity was also heterogeneous, appearing in both planktonic and aggregated cells. Planktonic cells that were SOS-positive appeared more filamented and less motile compared to SOS-negative cells within the same host (SI Movie 6). The activation of the SOS reporter in vitro and in vivo by ciprofloxacin (SI Movie 6 and Fig S3C and S3D) suggests that in both cases a canonical SOS response is involved in the perturbation of *Vibrio* physiology.

Together, these data begin to reveal a mechanism by which the intestine amplifies the effect of low-dose ciprofloxacin. Individual *Vibrio* cells first undergo an SOS response that is associated with changes in cellular morphology and behavior. In the context of the mechanical activity of the intestine, these molecular and cellular-level changes then give rise to population-level aggregation and spatial reorganization throughout the entire length of the intestine, with the population shifting its center of mass posteriorly (Fig. 2G, $n = 4$ per case). This process culminates in the expulsion of large bacterial aggregates from the host, causing a precipitous decline in total bacterial abundance (Fig. 2H).

Low-dose ciprofloxacin suppresses small cluster reservoirs associated with intestinal persistence

In contrast to *Vibrio*, *Enterobacter* is slower growing, non-motile, and naturally forms dense aggregates within the zebrafish intestine. *Enterobacter* populations have an in vivo growth rate of $0.27 \pm 0.05 \text{ h}^{-1}$ (mean \pm std. dev, SI Appendix, Fig. S1), compared to $0.8 \pm 0.3 \text{ h}^{-1}$ for *Vibrio* [76]. Based on

conventional notions of antibiotic tolerance, we hypothesized that *Enterobacter* would be less affected by ciprofloxacin treatment than the fast growing, planktonic *Vibrio*. However, as detailed below, we found this prediction to be incorrect; *Enterobacter* exhibits an even greater response to low-dose ciprofloxacin.

We first established in vitro that 25 ng/ml ciprofloxacin produces similar effects on *Enterobacter* growth as did 10 ng/ml exposure on *Vibrio*. With the identical inoculation procedure used for *Vibrio*, log₁₀-transformed *Enterobacter* abundance in the flask water dropped by 1.2 ± 0.4 (mean \pm std. dev.) compared to untreated controls after 24 hours, and dropped by 1.8 ± 0.2 after 48 hours (Fig. 3A). These values match well the values for *Vibrio*: 0.98 ± 0.37 for 24 hours, 1.81 ± 0.5 for 48 hours. Assays in rich media show a similarly reduced density between the two species (SI Appendix, Fig. S8) and an even lesser degree of cell death and damage in vitro for *Enterobacter* as compared to *Vibrio*, with a viable fraction of approximately 95% (SI Appendix, Fig. S9A and S9B). As with *Vibrio*, in vitro growth measurements and viability staining both imply that low-dose ciprofloxacin treatment of *Enterobacter* induces growth arrest rather than widespread lethality.

Strikingly, low-dose ciprofloxacin treatment of fish colonized with *Enterobacter* (Materials and Methods) resulted in even greater reductions in abundance than in the case of *Vibrio*, with the majority of populations becoming nearly or completely extinct during the assay period (Fig. 3A and 3B). Inoculation, treatment, dissection, and plating were performed as for *Vibrio* (Materials and Methods). Compared to untreated controls, log₁₀-transformed intestinal abundances were reduced by 2.3 ± 1.1 after 24 hours, and by 3.2 ± 1.0 after 48 hours (Fig. 3A). These reductions in intestinal abundances greatly exceeded the reductions of bacterial abundances in the flask water (Fig 3A). In terms of absolute abundances,

pooled data from 24 and 48 hour treatments gives a mean \pm std. dev. of the log₁₀-transformed *Enterobacter* population of 1.5 ± 1.0 ($n = 40$), compared to 4.0 ± 1.0 ($n = 39$) for untreated specimens (Fig. 3B); unpooled data are similar (SI Appendix, Fig. S9C and S9D).

Live imaging of intestinal populations at single time points revealed approximately 40% of treated hosts to be devoid or nearly devoid of *Enterobacter*, consistent with the plating-based measurements. In hosts that contained appreciable bacterial populations we observed a clear difference between treated and untreated specimens: *Enterobacter* populations in ciprofloxacin-treated hosts contained fewer small bacterial clusters and fewer individual planktonic cells than untreated controls (Fig. 3C and 3D). We quantified this distinction using computational image analysis to identify each cluster (Materials and Methods), defining a single cell as a cluster of size one. Bacterial populations in ciprofloxacin-treated animals contained $\sim 80x$ fewer clusters than untreated animals (Fig. 3C). Viability staining showed that there were no obvious differences in the viable fractions of bacteria expelled from the intestines of untreated and treated hosts (Fig. 3D, insets, SI Appendix, Fig. S10). As with *Vibrio*, these observations suggested that the reduction in *Enterobacter*'s intestinal abundance was independent of cell death.

Previous studies of other naturally aggregated bacterial species have revealed that large bacterial aggregates are highly susceptible to expulsion from the gut [76, 86]. To establish whether this is also the case for *Enterobacter* in the absence of low-dose ciprofloxacin treatment, we performed time-lapse 3D imaging (Materials and Methods). Indeed, in 2 out of 5 hosts imaged for 3.5 hours each, we observed events in which the largest bacterial aggregate was abruptly expelled from the

intestine (Fig. 4A and SI Movie 7). These time-lapse movies also showed clear examples of cluster aggregation (SI Movie 8), in which single cells and small aggregates appear to come together and fuse, a process that is likely due to the rhythmic intestinal contractions that occur between frames. Importantly, smaller aggregates and planktonic cells that preferentially localize to the intestinal bulb are relatively undisturbed during these expulsion events, save for a few clusters that become incorporated into the large mass during its transit (SI Movie 7).

Our observations suggest an explanation of how low-dose ciprofloxacin can lead to dramatic drops in *Enterobacter* abundance that moreover illuminates the more general question of how naturally aggregating bacterial species can persist in the vertebrate gut in spite of transport-driven expulsion. We provide both a qualitative and a quantitative description of the relevant dynamics, beginning with the following conceptual model: single cells of *Enterobacter* replicate to form small clusters, which then aggregate to form larger clusters under the influence of intestinal flow. Large clusters are transported by the rhythmic contractions of the gut [76, 86, 87] and are stochastically expelled from the host [76, 86]. The individual bacteria and small clusters that remain within the intestine serve as a reservoir that reseeds the next population, and the process of replication, aggregation, and expulsion repeats. Therefore, persistence within the intestine requires processes that generate single cells or small clusters, otherwise transport will eventually lead to extinction. This reseeding could take the form of (i) immigration of new cells from the environment, (ii) passive fragmentation of clusters, or (iii) active fragmentation in which single cells break away from a cluster surface during cell division. Immigration from the environment likely occurs even in established populations, but measurements in larval zebrafish suggest very low rates

of immigration [88]. We therefore suspected that more robust mechanisms must promote persistence. Supporting the active fragmentation mechanism, we found in untreated hosts examples of *Enterobacter* populations that contain an abundance of single cells, a single large aggregate, and a lack of mid-sized aggregates (SI Appendix, Fig. S9E). Following low-dose ciprofloxacin treatment, the planktonic cell reservoir associated with resilience to intestinal transport is depleted (Fig. 3C), most likely due to stalled *Enterobacter* division (SI Appendix, Fig. S8), leading to collapse of the resident bacterial population (Fig. 3A and 3B).

A quantitative model of bacterial cluster dynamics

To solidify and test our conceptual picture, we developed a predictive mathematical model of bacterial cluster dynamics. We describe the framework of the model, its validation, and general insights it provides into perturbations and population stability. Drawing on ideas from non-equilibrium statistical mechanics and soft matter physics, we constructed a general kinetic model that describes the time evolution of a collection of bacterial clusters with varying sizes, illustrated schematically in Fig. 4B. We posit that four processes govern cluster dynamics: aggregation, fragmentation, growth, and expulsion. Each is described by a kernel that specifies its rate and size dependence: (1) aggregation of a cluster of size n and a cluster of size m occurs with rate A_{nm} ; (2) fragmentation of a cluster of size $n+m$ into clusters of size n and m occurs with rate F_{nm} ; (3) growth (due to cell division) of a cluster of size n occurs with rate G_n ; (4) expulsion (removal by intestinal transport) of a cluster of size n occurs with rate E_n . Note that condensation of the population into a single massive cluster poises the system for extinction, for any nonzero E_n . The model is non-spatial and is inspired by well established

frameworks for nucleation and growth phenomena such as polymer gelation and colloidal aggregation [89]. For example, sol-gel models describe a transition between dispersed individual units (“sol”) and a system-spanning connected network (“gel”) in materials capable of polymerization. In the thermodynamic limit of infinite system size, the model can be studied using standard analytic techniques [89]. However, unlike polymer solutions and other bulk systems for which the possible number of clusters is effectively unbounded, our intestinal populations are constrained to have at most a few hundred clusters (Fig. 3C), necessitating the use of stochastic simulations (Materials and Methods).

In its general form, the model encompasses a wide range of behaviors that can be encoded in the various functional forms possible for the rate kernels A_{nm} , F_{nm} , G_n , and E_n . Based on our observations and theoretical considerations elaborated in the Materials and Methods section, we made the following assumptions: (1) the rate of aggregation between two clusters is independent of their size, $A_{nm} = \alpha$; (2) fragmentation occurs only by separation of single cells and with a rate that is independent of cluster size, $F_{nm} = \beta$ for $m = 1$ and $F_{nm} = 0$ otherwise; (3) growth is logistic with a global carrying capacity, $G_n = rn(1 - N/K)$ with N the total number of cells, r the per capita growth rate, and K , the carrying capacity; (4) expulsion is independent of cluster size, $E_n = \lambda$. This model contains as special cases various simple models of linear polymers [90] and also resembles recent work modelling chains of *Salmonella typhimurium* cells in the mouse gut [91]. As discussed in the SI Appendix, these choices constitute the minimal model consistent with theoretical constraints and experimental phenomenology. More complex models are of course possible, but the requisite increase in the number of

adjustable parameters would result in a trivial but meaningless ability to fit the observed data.

Even with the assumptions described above, the model needs 5 parameters: rates of aggregation, fragmentation, growth, and dispersal, and a global carrying capacity. However, all of these parameters can be set by experimentally derived values unrelated to cluster size distributions. We measured *Enterobacter*'s per capita growth rate by performing time-lapse imaging of initially germ-free hosts that had been exposed to *Enterobacter* for only 8 hours, capturing the exponential increase of a small founding population (SI Appendix, Fig. S1, SI Movie 9), yielding $r = 0.27 \pm 0.05 \text{ hr}^{-1}$ (mean \pm std. dev across $n = 3$ hosts). We identified expulsion events as abrupt collapses in *Enterobacter* abundance from time-lapse images (Fig. 3C, SI Movie 7) and set the expulsion rate equal to the measured collapse rate, $\lambda = 0.11 \pm 0.08 \text{ hr}^{-1}$ (mean \pm standard error, assuming an underlying Poisson process (Materials and Methods)). The model can be simulated to provide the mean and variance of the \log_{10} -transformed abundance distribution at a given time for a given set of parameters. Using this approach, we fit static bacterial abundance measurements from dissection and plating at 72 hours post-inoculation (Materials and Methods) to determine the carrying capacity, K , and the ratio of fragmentation and aggregation rates, β/α . As discussed in the Materials and Methods section, the cluster dynamics should depend primarily on the ratio of β/α rather than either rate separately. This yielded $\log_{10} K = 5.0 \pm 0.5$ and $\log_{10} \beta/\alpha = 2.5 \pm 0.4$.

The model therefore allows a parameter-free prediction of the size distribution of *Enterobacter* aggregates, plotted in Fig. 5A together with the measured distribution derived from three-dimensional images, averaged across 12 untreated

hosts. The two are in remarkable agreement. We also plot, equivalently, the cumulative distribution function $P(\text{size} > n)$, the probability that a cluster will contain greater than n cells, again illustrating the close correspondence between the data and the prediction and validating the model. We emphasize that no information about the cluster size distribution was used to estimate any of the model parameters. We further note that the cluster size distribution is a stringent test of the model's validity. Other cluster models predict different forms, typically with steep tails [90, 91]. The linear chain model of [91], for example, leads to an exponential distribution of cluster sizes that does not match the shallower, roughly power-law form of our data.

The abundance phase diagram and extinction transition

Our kinetic model provides insights into the consequences of low-dose antibiotic perturbations on gut bacterial populations. We consider a general phase diagram of possible growth, fragmentation, aggregation, and expulsion rates, and then situate *Enterobacter* in this space. For simplicity of illustration, we consider a two-dimensional representation with one axis being the ratio of the fragmentation and aggregation rates, β/α , and the other being the ratio of the growth and expulsion rates, r/λ (Fig. 5B). As noted above and in the Materials and Methods section, the model in the regime studied should depend on the ratio β/α rather than on β or α independently. However, the roles of r and λ are not simply captured by their ratio. The expulsion rate nonetheless provides a scale to which to compare the growth rate, r , and we plot Fig. 5B using r/λ calculated for fixed $\lambda = 0.11 \text{ hr}^{-1}$, the measured value. For completeness, we show a three-dimensional $r, \lambda, \beta/\alpha$ phase diagram as SI Appendix, Figure S11E and S11F. We numerically

calculated the steady state phase diagram of the model (Materials and Methods) and show in Figure 5B the mean log-transformed abundance, $\langle \log_{10}(N + 1) \rangle$. The regime of extinction ($N = 0$) is evident (dark purple, with dashed white boundary).

The data-derived parameter values place untreated intestinal *Enterobacter* fairly close to the extinction transition (Fig. 5B). An antibiotic-induced growth rate reduction of approximately 5x is sufficient to cross the boundary to the $N = 0$ regime (i.e. to extinction), moving downward in Fig. 5B. This growth rate reduction, or an equivalent increase in death rate, reflects the conventional view of antibiotic effects. An approximately 300x reduction in the balance between fragmentation and aggregation spurs an alternative path to extinction, moving leftward in Fig. 5B, reflecting a distinct mechanism resulting solely from changes in physical structure. The extinction transition in this direction corresponds to the condensation of the population into a single cluster, reminiscent of gelation phase transitions in polymer systems. As described above, low-dose ciprofloxacin causes a strong reduction in the number of small bacterial clusters, lowering β and possibly also r if fragmentation and individual cell division are linked. Conservatively assuming an equal effect along both axes, and fitting simulations to the 24 hour treatment abundances (Materials and Methods), we find that the antibiotic reduces r and β/α by ~ 10 x. This drives the bacterial system through the phase boundary and well into the extinction regime (Fig. 5B, orange circle), consistent with our observations.

In contrast to *Enterobacter*, treatment of *Vibrio* with ciprofloxacin does not lead to widespread extinction after 48 hours, suggesting that treated populations either lie safely at a new steady state away from the extinction boundary, or are

close enough to the transition so that dynamics are slow. To estimate model parameters for ciprofloxacin-treated *Vibrio*, we performed a two parameter fit of $(\beta/\alpha, r)$ to the 24 hour treatment abundances. Because of *Vibrio*'s large population size ($\sim 10^5$ clusters), we modified the stochastic simulation procedure using a tau-leaping algorithm (Materials and Methods, SI Appendix, Fig. S12). We indeed find ciprofloxacin-treated *Vibrio* is located close to but safely inside the extinction boundary (Fig. 5B). Untreated *Vibrio* populations show no appreciable multicellular aggregation and are located off-scale far to the upper-right side of the phase diagram (Fig. 5B, arrow).

Discussion

We have discovered that sublethal levels of a commonly used antibiotic can reduce the intestinal abundance of bacterial populations much more severely than would be predicted from in vitro responses, and that this amplification is a consequence of drug-induced changes to the bacterial groups' spatial architecture. Contrary to conventional notions of antibiotic tolerance, largely derived from in vitro studies, reductions in bacterial abundances were greater for the slow-growing, aggregated *Enterobacter* species than for the fast-growing, planktonic *Vibrio*. Live imaging revealed drug-induced increases in bacterial cohesion that, coupled to gut mechanical activity, lead to the expulsion of viable bacterial cells. The microscopic details of this cohesion, likely involving cell wall characteristics, mechanical compression by the gut wall and fluid flows, and perhaps intestinal mucus rheology, remain to be explored.

Notably, the underlying processes of bacterial aggregation and host intestinal transport are found throughout the animal kingdom, suggesting a

general relevance beyond zebrafish that may explain, for example, data on weak antibiotics having strong effects on mammalian microbiomes [63, 64]. Of course, chemical perturbations in more anatomically complex animals or non-gnotobiotic animals that house hundreds of resident bacterial species will undoubtedly involve additional processes beyond those uncovered here. We note, however, that responses to intestinal flow will influence bacterial population dynamics regardless of ecological complexity, and that our choice of model bacterial species spans the extremes of highly planktonic and highly cohesive strains, further implying generality. In the larval zebrafish, enhanced bacterial susceptibility to transport leads to expulsion from the gut. In larger or more complex intestines this may take the form of displacement from one region to a more distal region, with a corresponding shift in local nutrients or competitors, in addition to expulsion from the gut altogether.

The concentrations of ciprofloxacin examined here are commonly found in environmental samples, indicating a potentially widespread perturbation of animal gut microbiota due to antibiotic contaminants. In addition, the expulsion of live, antibiotic-exposed bacteria from animal intestines through the aggregation-based processes described here suggests a potential mechanism for enhanced spread of antibiotic resistance. This possibility is bolstered by our observation that in addition to aggregation, ciprofloxacin-treated cells undergo an active SOS response, which has been shown to promote mutation and horizontal gene transfer [92, 93, 94]. Together, these observations underscore recent concerns about the public health risk posed by antibiotic contaminants in the environment [67].

Our biophysical model of aggregation, fragmentation, growth, and expulsion describes our data well and provides testable predictions. It is remarkable, given

the chemical and morphological complexity of even the larval zebrafish gut, that such a minimal model can accurately predict emergent properties such as the size distribution of bacterial aggregates. That this works is an indication of the power of theories of soft condensed matter physics, whose generality may prove useful in understanding the gut microbiome. Furthermore, our model supplies a framework for a quantitative understanding of gut microbial homeostasis in general. Like recent work modelling antibody-mediated en chaining of *Salmonella* cells in the mouse gut [91], our model implies that the physical processes of bacterial cluster formation and fragmentation play central roles in large-scale microbiota stability. We suggest that our cluster-dynamics model, validated by quantitative agreement between predictions and in vivo data (Fig. 5A), may prove useful in less tractable host species such as mice and humans. Without live imaging or non-invasive sampling, it is challenging to estimate kinetic properties of microbial populations, such as aggregation rates. However, advances in histological sample preparation [95] can preserve bacterial aggregates and yield cluster size distributions; inverting our model, such distributions can reveal the underlying in vivo bacterial kinetics.

Regarding antibiotics, the main prediction of our model is that naturally aggregated, slow growing bacteria will be impacted more severely than fast growing, planktonic species by equivalent low-dose antibiotic perturbations. This is contrary to conventional wisdom that links bacterial tolerance to reduced growth and increased aggregation [68, 69], which stems from studies of antibiotic exposure in static or well-mixed environments. We find that in the intestine, where bacteria can be removed through fluid flow, there exist critical values of aggregation, fragmentation, growth, and expulsion rates, beyond which sustainable colonization becomes impossible (Fig. 5B). Naturally aggregated and slow-growing

species are situated closer to this extinction phase boundary and are therefore more easily driven to population collapse by low-dose antibiotic perturbations. Intriguingly, new meta-omics methods [70] can be used to estimate *in vivo* growth rates of mammalian gut microbes, which would be interesting to correlate with antibiotic responses. We note in addition that inter-bacterial competition in the gut can be influenced by clustering and susceptibility to intestinal transport [76, 86], suggesting that competition outcomes could be altered by antibiotic treatment if changes in aggregation properties are different for different species. A final prediction of our model is that intestinal transport, which has been linked to microbiota composition [74], will influence the effects of low-dose antibiotic perturbations on microbial community composition. Combining pharmacological manipulations of intestinal transport with antibiotic treatments may therefore lead to novel strategies for precision engineering of the gut microbiome.

Materials and Methods

Animal care

All experiments with zebrafish were done in accordance with protocols approved by the University of Oregon Institutional Animal Care and Use Committee and following standard protocols [96].

Gnotobiology

Wild-type (AB×TU strain) zebrafish were derived germfree (GF) and colonized with bacterial strains as previously described [97] with slight modifications elaborated in the SI Appendix.

Bacterial strains and culture

Vibrio cholerae ZWU0020 and *Enterobacter cloacae* ZOR0014 were originally isolated from the zebrafish intestine [75]. Fluorescently marked derivatives of each strain were previously generated by Tn7-mediated insertion of a single constitutively expressed gene encoding dTomato [77]. We note that all plating- and imaging-based experiments performed in this study were done using fluorescently marked strains, which carry a gentamicin resistance cassette, with the exception of experiments in which fluorescent dyes were used to assess viability of cells. Archived stocks of bacteria were maintained in 25% glycerol at -80°C. Prior to experiments, bacteria were directly inoculated from frozen stocks into 5 ml LB media (10 g/L NaCl, 5 g/L yeast extract, 12 g/L tryptone, 1 g/L glucose) and grown for ~16 hours (overnight) shaking at 30°C.

Culture-based quantification of bacterial populations

Dissection of larval guts was done as described previously [98], with slight modifications elaborated in the SI Appendix. To compare the effect of ciprofloxacin on populations in the intestine and in the flask water, we normalized treated abundances by the corresponding untreated median abundance (Fig. 2C and 3A). To account for variation in untreated bacterial dynamics between weekly batches of fish, we performed the normalization within each batch. Unnormalized data is available in the SI Dataset.

Light sheet fluorescence microscopy of live larval zebrafish

Live imaging of larval zebrafish was performed using a custom-built light sheet fluorescence microscope previously described in detail [99], with slight modifications elaborated in the SI Appendix.

Viability staining of expelled aggregates:

Germ-free larval zebrafish were colonized with wild type *Vibrio* or *Enterobacter* (without fluorescent markers) for 24 hours and then mounted into agarose plugs using small glass capillaries identically to the imaging procedure (above). Individual capillaries were suspended into isolated wells of a 24-well tissue culture plate filled with embryo media containing anesthetic or anesthetic + ciprofloxacin (10 ng/ml for *Vibrio*, 25 ng/ml for *Enterobacter*) and the larvae were extruded from the capillaries. Fish remained mounted for 24 hours, during which expelled bacteria remained caught in the agarose plug. After treatment, fish were pulled back into the capillaries and transferred to smaller wells of a 96 well plate containing embryo media, anesthetic, and the LIVE/DEAD BacLight Bacterial Viability stains SYTO9 and propidium iodide. Fish were stained according to kit instructions, with the exception of the incubation period being extended from 15 to 30 min to account for potential issues with the aggregate nature of the cells [100]. Following staining, fish were pulled again into the capillaries and transferred to the light sheet microscope for imaging. As shown in the SI Appendix, Figures S4 and S10, zebrafish cells stain in addition to bacterial cells, precluding accurate quantification of viable fractions.

Image analysis

Bacteria were identified in three-dimensional light sheet fluorescence microscopy images using a custom MATLAB analysis pipeline previously described [71, 99], with minor changes elaborated in the SI Appendix.

Kinetic model and stochastic simulations

Simulation details are provided in the SI Appendix. In brief, Gillespie's direct method [101] was used to simulate stochastic aggregation, fragmentation, and expulsion events, while growth was treated as deterministic. To simulate *Vibrio* populations, direct stochastic simulation becomes intractable due to the large number of clusters ($\sim 10^5$ single cells). We therefore implemented a modified tau-leaping algorithm [102] that facilitates large simulations. We opted for a straightforward fixed τ method and empirically determined an optimal value of $\tau = 0.001$ h (SI Appendix, Fig. S12A,B). All simulations were written in MATLAB and code is available at [INSERT URL](#)

Acknowledgements

We thank Rose Sockol and the University of Oregon Zebrafish Facility staff for fish husbandry. Research was supported by an award from the Kavli Microbiome Ideas Challenge, a project led by the American Society for Microbiology in partnership with the American Chemical Society and the American Physical Society and supported by The Kavli Foundation. Work was also supported by the National Science Foundation under Awards 1427957 (R.P.) and 0922951 (R.P.), the M.J. Murdock Charitable Trust, and the National Institutes of Health (<http://www.nih.gov/>), under Awards P50GM09891 and P01GM125576-01 to K.G.

and R.P., F32AI112094 to T.J.W., and T32GM007759 to B.H.S. The content is solely the responsibility of the authors and does not represent the official views of the NSF, National Institutes of Health, or other funding agencies. This work benefited from access to the University of Oregon high performance computer, Talapas.

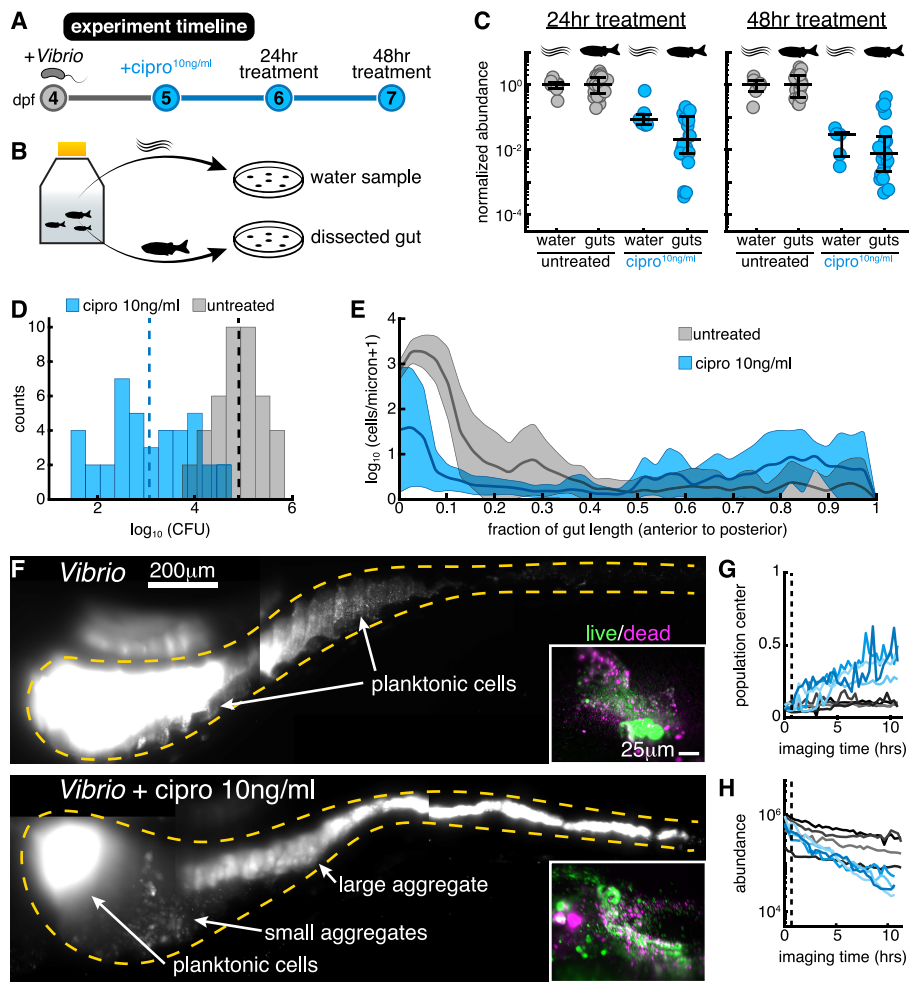


FIGURE S2. Low-dose ciprofloxacin induces *Vibrio* aggregation and expulsion in vivo. A: Schematic of the experimental timeline. B: Schematic of the sampling scheme for plating measurements. C: Normalized abundances (number of colony forming units (CFUs) scaled by untreated medians) of water and gut populations. N values left to right: 8, 24, 7, 20, 6, 18, 5, 20. Water N values denote number of flasks; gut N values denote number of fish. D: Histograms of gut CFUs with pooled data from 24 and 48 h treatments. Counts indicate the number of individual fish with a given \log_{10} *Vibrio* CFUs. Dashed lines indicate the mean of each set, showing a \sim 100-fold reduction in intestinal *Vibrio* abundance in antibiotic-treated fish. E: Ensemble-averaged spatial distributions of log-transformed cell density as a function of distance along the gut axis, integrated over the perpendicular dimensions. F: Maximum intensity projections of 3D images of untreated (top) and ciprofloxacin-treated (bottom) *Vibrio* populations. Insets: Viability staining of bacteria expelled from the gut, with green and magenta indicating living and dead cells, respectively. G-H: Dynamics of in vivo *Vibrio* populations untreated (grey lines) and treated with 10 ng/ml ciprofloxacin (blue lines). G: 1D center of mass, normalized to intestine length. H: Total image-derived *Vibrio* abundance. In both (G) and (H), each curve represents a different zebrafish. Vertical dotted lines indicate the time of drug administration to the treatment cohort, $t = 0.67$ hours.

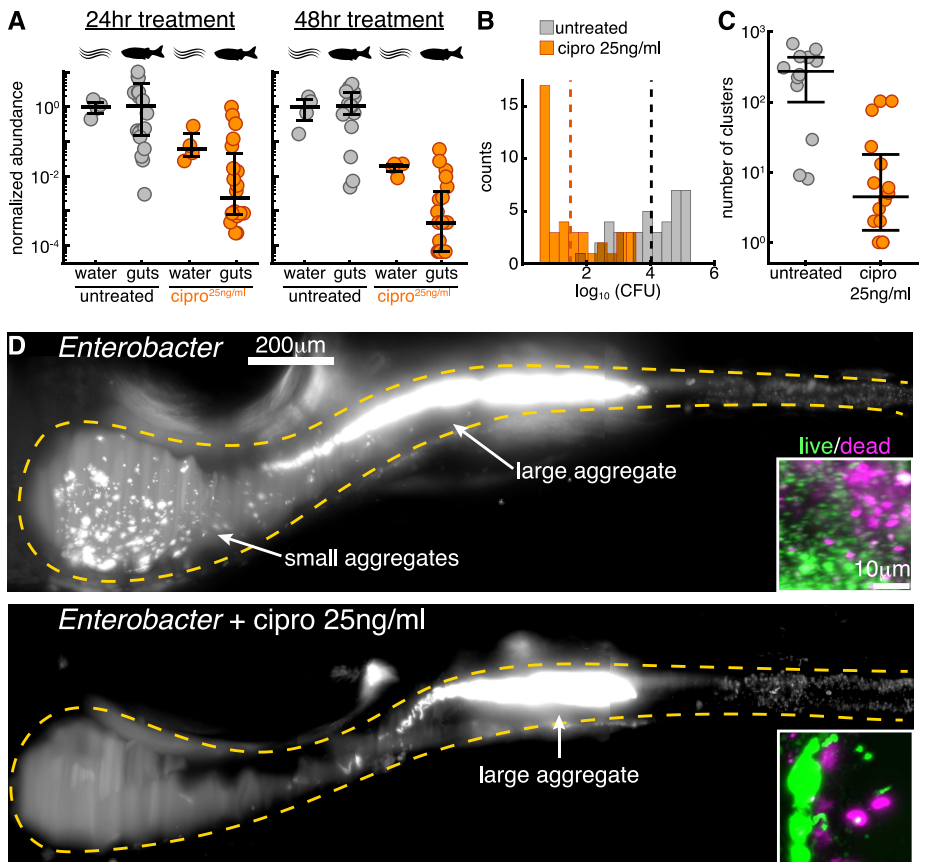


FIGURE S2. Low-dose ciprofloxacin collapses *Enterobacter* populations and suppresses small clusters *in vivo*. A: Normalized abundances (number of colony forming units (CFUs) scaled by untreated medians) of water and gut populations. N values left to right: 4, 20, 4, 20, 4, 19, 4, 20. Water N values denote number of flasks; gut N values denote number of fish. B: Histograms of gut CFUs with pooled data from 24 and 48 h treatments. Counts indicate the number of individual fish with a given \log_{10} *Enterobacter* CFUs. Dashed lines indicate the mean of each set, showing a ~1000-fold reduction in intestinal *Enterobacter* abundance in antibiotic-treated fish. C: Total number of bacterial clusters in the intestine, quantified from 3D images (Materials and Methods). D: Maximum intensity projections of 3D images of untreated (top) and ciprofloxacin-treated (bottom) *Enterobacter* populations. Insets: Viability staining of bacteria expelled from the gut, with green and magenta indicating living and dead cells, respectively.

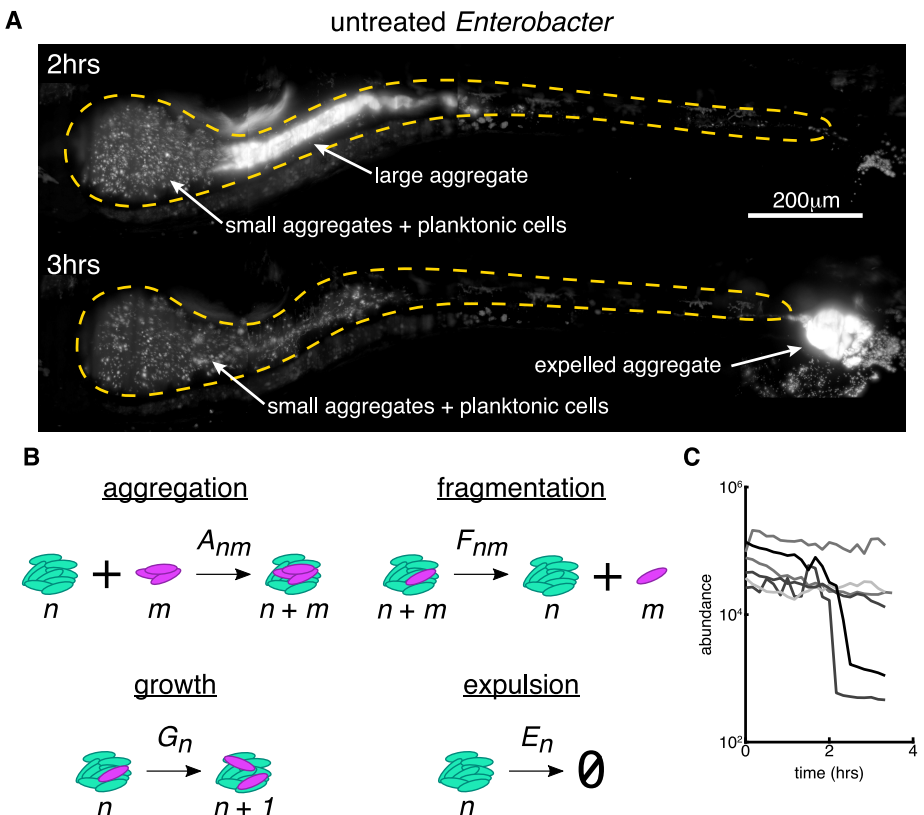


FIGURE S2. Small bacterial clusters are required for recovery after large expulsion events. A: Maximum intensity projections of untreated *Enterobacter* populations before (top, $t = 2$ hours from the start of imaging) and after (bottom, $t = 3$ hours) an expulsion event (See also SI Movie 5). Scale bar = 200 μm . B: Schematic of a kinetic model of bacterial cluster dynamics, illustrating its four constituent processes. C: Image-derived time-series of *Enterobacter* abundance in five untreated hosts showing sporadic large expulsion events.

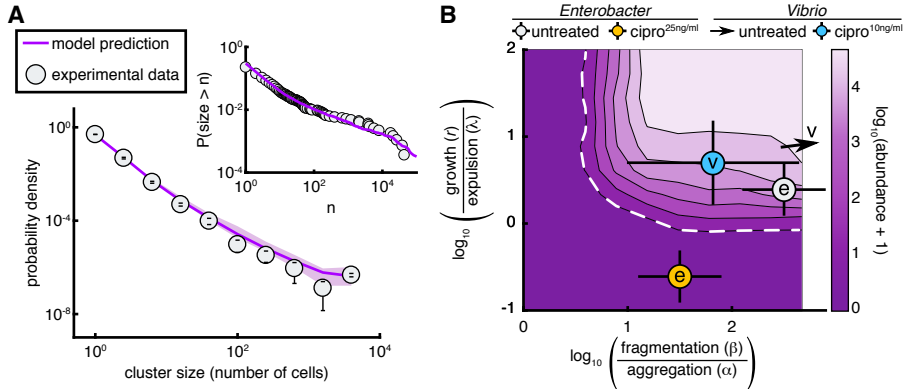


FIGURE S2. A stochastic kinetic model predicts bacterial cluster sizes and generates a phase diagram for in vivo abundance. A: The distribution of image-derived *Enterobacter* cluster sizes (grey circles) along with the prediction of our stochastic model (purple line). There are no free parameters in the fit; values were fixed by abundance, growth, and expulsion rate measurements independent of cluster size. Parameters: $r = 0.27 \text{ hr}^{-1}$, $\lambda = 0.11 \text{ hr}^{-1}$, $\alpha = 0.1 \text{ hr}^{-1}$, $\beta = 10^{1.5} \text{ hr}^{-1}$, $K = 10^5$. Error bars on experimental data are standard deviations across hosts. Shaded confidence intervals for the model prediction are bounds from parameter uncertainties. Inset: The same experimental data and model plotted without binning as a reverse cumulative distribution. B: Phase diagram of the log-transformed abundance, $\langle \log_{10}(N + 1) \rangle$, showing the extinction transition (white dashed line). From best fit parameter estimates, the in vivo state of untreated *Enterobacter* is overlaid as a grey circle, and 25 ng/ml ciprofloxacin-treated *Enterobacter* as an orange circle; both circles are marked with “e”. Untreated *Vibrio* is located off the scale, indicated by the arrow, 10 ng/ml ciprofloxacin treated *Vibrio* is overlaid as a cyan circle marked with “v”. The doses for *Enterobacter* and *Vibrio* were established to be approximately equivalent in vitro. Parameters: $\lambda = 0.11 \text{ hr}^{-1}$, $\alpha = 0.1 \text{ hr}^{-1}$, $K = 10^5$ were fixed; r and β were varied on logarithmic grids.

REFERENCES CITED

- [62] Dethlefsen L, Relman DA (2011) Incomplete recovery and individualized responses of the human distal gut microbiota to repeated antibiotic perturbation. *Proceedings of the National Academy of Sciences* 108(Supplement 1):4554–4561.
- [63] Cho I, et al. (2012) Antibiotics in early life alter the murine colonic microbiome and adiposity. *Nature* 488(7413):621.
- [64] Schulfer AF, et al. (2019, doi:10.1038/s41396-019-0349-4, published online ahead of print) The impact of early-life sub-therapeutic antibiotic treatment (STAT) on excessive weight is robust despite transfer of intestinal microbes. *The ISME Journal*.
- [65] Gaulke CA, Barton CL, Proffitt S, Tanguay RL, Sharpton TJ (2016) Triclosan exposure is associated with rapid restructuring of the microbiome in adult zebrafish. *PLoS One* 11(5):e0154632.
- [66] Andersson DI, Hughes D (2014) Microbiological effects of sublethal levels of antibiotics. *Nature Reviews Microbiology* 12(7):465.
- [67] "National Academies of Sciences E, Medicine, others" (2018) *Environmental Chemicals, the Human Microbiome, and Health Risk: A Research Strategy.* (National Academies Press).
- [68] Walters MC, Roe F, Bugnicourt A, Franklin MJ, Stewart PS (2003) Contributions of antibiotic penetration, oxygen limitation, and low metabolic activity to tolerance of *pseudomonas aeruginosa* biofilms to ciprofloxacin and tobramycin. *Antimicrobial Agents and Chemotherapy* 47(1):317–323.
- [69] Fux C, Costerton JW, Stewart PS, Stoodley P (2005) Survival strategies of infectious biofilms. *Trends in Microbiology* 13(1):34–40.
- [70] Korem T, et al. (2015) Growth dynamics of gut microbiota in health and disease inferred from single metagenomic samples. *Science* 349(6252):1101–1106.
- [71] Schlomann BH, Wiles TJ, Wall ES, Guillemin K, Parthasarathy R (2018) Bacterial cohesion predicts spatial distribution in the larval zebrafish intestine. *Biophysical Journal* 115(11):2271–2277.
- [72] Moor K, et al. (2017) High-avidity IgA protects the intestine by en chaining growing bacteria. *Nature* 544(7651):498.

- [73] Welch JLM, Hasegawa Y, McNulty NP, Gordon JI, Borisy GG (2017) Spatial organization of a model 15-member human gut microbiota established in gnotobiotic mice. *Proceedings of the National Academy of Sciences* 114(43):E9105–E9114.
- [74] Cremer J, Arnoldini M, Hwa T (2017) Effect of water flow and chemical environment on microbiota growth and composition in the human colon. *Proceedings of the National Academy of Sciences* 114(25):6438–6443.
- [75] Stephens WZ, et al. (2016) The composition of the zebrafish intestinal microbial community varies across development. *ISME Journal* 10:644–654.
- [76] Wiles TJ, et al. (2016) Host Gut Motility Promotes Competitive Exclusion within a Model Intestinal Microbiota. *PLoS Biology* 14(7):1–24.
- [77] Wiles TJ, et al. (2018) Modernized tools for streamlined genetic manipulation and comparative study of wild and diverse proteobacterial lineages. *mBio* 9(5):e01877–18.
- [78] Dethlefsen L, Relman DA (2011) Incomplete recovery and individualized responses of the human distal gut microbiota to repeated antibiotic perturbation. *Proceedings of the National Academy of Science* 108.
- [79] Girardi C, et al. (2011) Biodegradation of ciprofloxacin in water and soil and its effects on the microbial communities. *Journal of Hazardous Materials* 198:22–30.
- [80] Goneau LW, et al. (2015) Subinhibitory antibiotic therapy alters recurrent urinary tract infection pathogenesis through modulation of bacterial virulence and host immunity. *mBio* 6(2):e00356–15.
- [81] Rennekamp AJ, Peterson RT (2015) 15 years of zebrafish chemical screening. *Current opinion in chemical biology* 24:58–70.
- [82] Yoganantharajah P, Gibert Y (2017) The use of the zebrafish model to aid in drug discovery and target validation. *Current topics in medicinal chemistry* 17(18):2041–2055.
- [83] Erill I, Campoy S, Barbé J (2007) Aeons of distress: an evolutionary perspective on the bacterial sos response. *FEMS Microbiology Reviews* 31(6):637–656.
- [84] Kreuzer KN (2013) Dna damage responses in prokaryotes: regulating gene expression, modulating growth patterns, and manipulating replication forks. *Cold Spring Harbor Perspectives in Biology* 5(11):a012674.

- [85] Irazoki O, Mayola A, Campoy S, Barbé J (2016) Sos system induction inhibits the assembly of chemoreceptor signaling clusters in salmonella enterica. *PLoS One* 11(1):e0146685.
- [86] Logan SL, et al. (2018) The Vibrio cholerae type VI secretion system can modulate host intestinal mechanics to displace gut bacterial symbionts. *Proceedings of the National Academy of Sciences* 115(16):E3779–E3787.
- [87] Ganz J, et al. (2018) Image velocimetry and spectral analysis enable quantitative characterization of larval zebrafish gut motility. *Neurogastroenterology & Motility* 30(9):e13351.
- [88] Robinson CD, et al. (2018) Experimental bacterial adaptation to the zebrafish gut reveals a primary role for immigration. *PLoS biology* 16(12):e2006893.
- [89] Krapivsky PL, Redner S, Ben-Naim E (2010) *A Kinetic View of Statistical Physics*. (Cambridge University Press).
- [90] Krapivsky P, Redner S (1996) Transitional aggregation kinetics in dry and damp environments. *Physical Review E* 54(4):3553.
- [91] Bansept F, et al. (2019) Enchained growth and cluster dislocation: a possible mechanism for microbiota homeostasis. *bioRxiv*, doi: 10.1101/298059, 2019.
- [92] Baharoglu Z, Mazel D (2011) Vibrio cholerae triggers sos and mutagenesis in response to a wide range of antibiotics: a route towards multiresistance. *Antimicrobial Agents and Chemotherapy* 55(5):2438–2441.
- [93] Guerin É, et al. (2009) The sos response controls integron recombination. *Science* 324(5930):1034–1034.
- [94] Beaber JW, Hochhut B, Waldor MK (2004) Sos response promotes horizontal dissemination of antibiotic resistance genes. *Nature* 427(6969):72.
- [95] Tropini C, Earle KA, Huang KC, Sonnenburg JL (2017) The gut microbiome: connecting spatial organization to function. *Cell Host & Microbe* 21(4):433–442.
- [96] Westerfield M (2007) The Zebrafish Book. A Guide for the Laboratory Use of Zebrafish (*Danio rerio*), 5th Edition. *University of Oregon Press, Eugene (Book)*.
- [97] Melancon E, et al. (2017) Best practices for germ-free derivation and gnotobiotic zebrafish husbandry. *Methods in Cell Biology* 138:61–100.
- [98] Milligan-Myhre K, et al. (2011) Study of host–microbe interactions in zebrafish in *Methods in Cell Biology*. (Elsevier) Vol. 105, pp. 87–116.

- [99] Jemielita M, et al. (2014) Spatial and temporal features of the growth of a bacterial species colonizing the zebrafish gut. *mBio* 5(6):1–8.
- [100] Netuschil L, Auschill TM, Sculean A, Arweiler NB (2014) Confusion over live/dead stainings for the detection of vital microorganisms in oral biofilms—which stain is suitable? *BMC Oral Health* 14(1):2.
- [101] Gillespie DT (1977) Exact stochastic simulation of coupled chemical reactions. *The Journal of Physical Chemistry* 81(25):2340–2361.
- [102] Gillespie DT (2001) Approximate accelerated stochastic simulation of chemically reacting systems. *The Journal of Chemical Physics* 115(4):1716–1733.

APPENDIX B

SWIMMING MOTILITY OF A GUT BACTERIAL SYMBIONT PROMOTES RESISTANCE TO INTESTINAL EXPULSION AND ENHANCES INFLAMMATION

B.1. Abstract

Some of the densest microbial ecosystems in nature thrive within the intestines of humans and other animals. To protect mucosal tissues and maintain immune tolerance, animal hosts actively sequester bacteria within the intestinal lumen. In response, numerous bacterial pathogens and pathobionts have evolved strategies to subvert spatial restrictions, thereby undermining immune homeostasis. However, in many cases, it is unclear how escaping host spatial control benefits gut bacteria and how changes in intestinal biogeography are connected to inflammation. A better understanding of these processes could uncover new targets for treating microbiome-mediated inflammatory diseases. To this end, we investigated the spatial organization and dynamics of bacterial populations within the intestine using larval zebrafish and live imaging. We discovered that a proinflammatory *Vibrio* symbiont native to zebrafish governs its own spatial organization using swimming motility and chemotaxis. Surprisingly, we found that *Vibrio*'s motile behavior does not enhance its growth rate but rather promotes its persistence by enabling it to counter intestinal flow. In contrast, *Vibrio* mutants lacking motility traits surrender to host spatial control, becoming aggregated and entrapped within the lumen. Consequently, non-motile and non-chemotactic mutants are susceptible to intestinal expulsion and experience large fluctuations in absolute abundance.

Further, we found that motile *Vibrio* cells induce expression of the proinflammatory cytokine TNF α in gut-associated macrophages and the liver. Using inducible genetic switches, we demonstrate that swimming motility can be manipulated *in situ* to modulate the spatial organization, persistence, and inflammatory activity of gut bacterial populations. Together, our findings suggest that host spatial control over resident microbiota plays a broader role in regulating the abundance and persistence of gut bacteria than simply protecting mucosal tissues. Moreover, we show that intestinal flow and bacterial motility are potential targets for therapeutically managing bacterial spatial organization and inflammatory activity within the gut.

B.2. Introduction

Humans and other animals foster diverse microbial communities within their intestines. Although these symbiotic consortia support vital aspects of host biology, they can also harbor proinflammatory pathogens and pathobionts, which are indigenous members of the microbiota that have latent pathogenic potential [? ?]. Understanding how hosts normally constrain the virulent activities of resident bacteria and the mechanisms by which disease-causing lineages escape this control will open new opportunities for developing microbiome-based therapies to improve human and animal health.

One way hosts keep potentially pathogenic bacterial lineages in check within the intestine is by imposing widespread restrictions on microbiota spatial organization. The most recognized spatial control measures employed by the host are mucus, immunoglobulins, and antimicrobial peptides, which act to confine bacteria to the intestinal lumen, away from mucosal surfaces [3–5]. In turn,

it is thought that intense competition for resources pushes bacteria to evolve strategies for subverting host control and occupying new spatial niches [6,7]. In line with this idea, several prototypic pathobionts undergo blooms in abundance that are coincident with shifts in intestinal biogeography [1,8–10]. A potential trait underlying this behavior that is common to many pathobionts—as well as numerous bona fide pathogens—is flagella-based swimming motility [11–13].

Swimming motility, together with chemotaxis, gives bacteria the agency to govern their own spatial organization and access niches that are typically thought to enhance growth and survival [14–17]. The connection between motility and gastrointestinal colonization has historically been studied in the context of pathogens such as *Helicobacter pylori*, *Campylobacter jejuni*, *Vibrio cholerae*, and *Salmonella Typhimurium* [12]. With *S. Typhimurium* in particular, it has been found that this pathogen uses motility and chemotaxis to associate with and invade the intestinal mucosa, induce inflammation, and facilitate growth [17–19]. In several instances it has also been shown that flagellin, the protein subunit comprising the bacterial flagellum, can be a major driver of inflammation [20–22]. Highlighting the importance of curbing the pathogenic potential of motile bacteria, studies in mice have revealed several mechanisms by which hosts detect and quench flagellar motility to maintain intestinal homeostasis [4,20,23,24]. In total, significant progress has been made in understanding the role motility plays in the infectious lifestyles of pathogens and its proinflammatory consequences for the host. However, a broader view of how motility behaviors might be shaping the lifestyles of resident gut bacteria remains limited and largely unexplored.

Insights into this question have started to emerge from our studies on how diverse bacterial taxa colonize the zebrafish intestine. The optical transparency

and small size of larval zebrafish make them an ideal vertebrate model for probing how bacteria use motility to spatially organize their populations within a living animal. With light sheet fluorescence microscopy (LSFM) it is possible to capture the full three-dimensional architecture of bacterial populations at single bacterial cell resolution across the entire length of the larval intestine [25]. In addition, the spatiotemporal dynamics of bacterial and host cells can be followed in real time or over the course of many hours. Using LSFM, we have found that for many non-inflammatory commensal bacteria native to the zebrafish microbiome, the bulk of their populations are non-motile and reside as dense multicellular aggregates within the intestinal lumen [26,27]. Notably, this pattern of bacterial spatial organization is consistent with histological data from both the mouse and human intestine [28–31]. We discovered that in this aggregated regime, bacteria are extremely vulnerable to intestinal flow. Consequently, aggregated bacterial populations can be stochastically expelled from the host in large numbers, producing punctuated drops in abundance [32,33].

In contrast, unlike most zebrafish gut bacteria studied thus far, we have identified an isolate of non-toxigenic *V. cholerae* (strain ZWU0020, further referred to as “Vibrio” for brevity) that exhibits pathobiont-like characteristics and assembles intestinal populations made up of planktonic cells displaying vigorous swimming motility [32,34]. This particular Vibrio strain was originally isolated from the intestine of an apparently disease-free zebrafish and does not encode cholera toxin or toxin-coregulated pilus [35]. The mass swimming behavior of Vibrio populations gives them a liquid-like space-filling property that promotes frequent and close contact with the intestinal mucosa [32]. This attribute appears to make Vibrio highly resistant to intestinal expulsion. As a result, Vibrio stably

colonizes the intestine and reaches absolute abundances that are up to ten times higher than other zebrafish symbionts [33]. *Vibrio*'s unique intestinal lifestyle is also potentially linked to its pathobiont character, which is marked by its ability to supplant established, naturally aggregated bacterial populations [32], and induce intestinal inflammation and exacerbate pathology in susceptible hosts [34,36].

In the present work we used *Vibrio* as model gut symbiont to investigate the mechanisms by which its motility behaviors control its colonization and contribute to its proinflammatory potential. By combining live imaging, host and bacterial mutants, and *in situ* manipulation of motility behaviors, we were able to disentangle *Vibrio*'s requirements for motility during multiple stages of intestinal colonization. We found that for *Vibrio*, swimming motility and chemotaxis do not enhance exponential growth rate but rather enable cells to physically resist intestinal expulsion and maintain stable, highly abundant populations. We also found that host tissues—namely, gut-associated macrophages and cells within the liver—are acutely sensitive to bacterial motility and spatial organization within the intestine. Together, our work expands the scope of bacterial swimming motility during intestinal colonization by revealing how motility can shape the large-scale spatial organization and dynamics of gut bacterial populations. Our study further shows that intestinal mechanics are a host spatial control measure capable of regulating the abundance and persistence of gut bacteria. Ultimately, our work yields new mechanistic insights into the form and function of the intestinal ecosystem and highlights that bacterial motility and the factors controlling the spatial organization of resident microbiota are potential targets for therapeutic manipulation of the gut microbiome.

B.3. Results

B.3.1. Loss of swimming motility or chemotaxis attenuates intestinal colonization and interbacterial competition

To dissect the role of flagellar motility during intestinal colonization, we generated two motility-deficient *Vibrio* mutants (S1A Fig). To test swimming motility in general, we deleted the two-gene operon *pomAB* that encodes the polar flagellar motor (creating a swimming motility-deficient *Vibrio* mutant we refer to as “ Δ mot”). To test *Vibrio*’s ability to spatially organize its populations in response to environmental cues, we deleted the gene *cheA2*, which encodes a histidine kinase necessary for chemotaxis (creating a chemotaxis-deficient *Vibrio* mutant we refer to as “ Δ che”). In vitro, Δ mot exhibited complete loss of swimming motility whereas Δ che had a run-biased behavior with swim speeds comparable to wild type but failed to chemotax in soft agar (S1B Fig). Both motility mutants displayed normal growth and assembled a single polar flagellum similar to wild type (S1C and S1D Fig).

We first assessed the absolute abundances of each strain over time by gut dissection and cultivation. We inoculated equal amounts of wild-type *Vibrio*, Δ mot, and Δ che individually into the aqueous environment of four-day-old germ-free larval zebrafish. *Vibrio* rapidly colonized germ-free animals to high abundance, reaching a maximal carrying capacity of 105–106 cells per intestine by 24 h post-inoculation (hpi) and maintaining a high-level of abundance through 72 hpi (Fig 1A). In contrast, Δ mot and Δ che displayed attenuated intestinal colonization phenotypes (Fig 1A). Both mutants were slow to access the zebrafish intestine and reached maximal abundances at 24 hpi that were 10–100-fold lower than wild type

(Fig 1A). This observation suggests that each mutant has a reduced immigration rate, which is in line with previous work indicating that bacterial motility traits may facilitate dispersal and initial colonization of the zebrafish intestine [37,38]. Importantly, differences in intestinal abundances did not appear to be due to differences in the water environment because the levels of each strain outside the fish remained constant and comparable over the assay period (Fig 1A inset).

Fig 1. Loss of swimming motility or chemotaxis attenuates intestinal colonization and interbacterial competition. (A) Abundances of wild-type Vibrio, Δ mot, and Δ che during mono-association. Plotted are medians and interquartile ranges ($n \geq 17$ animals/marker). Significant differences between each mutant and wild-type Vibrio determined by Mann-Whitney (purple asterisks: Δ mot; cyan asterisks: Δ che). *** $p \leq 0.0001$, ** $p = 0.0002$. Inset shows median bacterial abundances in the water environment from each replicate experiment across all time points. (B) Experimental timeline of Aeromonas–Vibrio competition. (C) Intestinal abundances of Aeromonas and wild-type or mutant Vibrio strains during different competition schemes. Aeromonas abundances while alone during mono-association are shown for statistical comparison. Letters denote significant differences between Aeromonas treatments. Lines show paired Aeromonas and Vibrio abundances within individual fish. $p \leq 0.05$, Kruskal-Wallis and Dunn's multiple comparisons test. Adjacent bars denote medians and interquartile ranges. Significant differences based on Wilcoxon between Aeromonas and each Vibrio strain are noted below each competition. (D) Abundances of wild-type and mutant Vibrios during competition with Aeromonas (from panel C) normalized to abundances during mono-association at 24 hpi (from panel A). Bars denote medians and interquartile ranges. Significant differences determined by Mann-

Whitney. Fold-decreases based on medians. Underlying data plotted in A, C, and D are provided in S1 Data.

We next compared the ability of wild-type *Vibrio* and each mutant to invade an established population of *Aeromonas veronii* (strain ZOR0001, further referred to as “*Aeromonas*”). Like *Vibrio*, *Aeromonas* species are abundant members of the zebrafish intestinal microbiota [35]. Previous studies suggest that these two genera naturally compete against one another within complex intestinal communities [39]. In addition, we have shown that *Vibrio* is capable of invading and displacing established *Aeromonas* populations in gnotobiotic animals [32]. Following the competition scheme depicted in Fig 1B, we found that each *Vibrio* strain had a distinct competitive interaction with *Aeromonas* (Fig 1C). Wild-type *Vibrio* potently colonized *Aeromonas*-occupied intestines and induced 10–100-fold drops in *Aeromonas* abundances (Fig 1C). Zebrafish colonized with the Δmot mutant, however, were dominated by *Aeromonas*, which did not experience any significant declines in abundance compared to mono-association (Fig 1C). Invasion with the Δche mutant had an intermediate impact on *Aeromonas* abundances and the two appeared to co-exist (Fig 1C). Comparing abundances during competition to those during mono-association showed that each *Vibrio* strain’s colonization was hindered to varying degrees while invading established *Aeromonas* populations (Fig 1D). Wild-type *Vibrio* abundances were only 2-fold lower during competition than during mono-association (Fig 1D). In contrast, Δmot abundances were 6-fold lower (and in several instances reduced by up to 100-fold), whereas the impact on Δche abundances was intermediate with a 4-fold reduction (Fig 1D). Overall, these data show that *Vibrio* requires swimming motility and chemotaxis for normal intestinal colonization and interbacterial competition.

B.3.2. Motility and chemotaxis mutants have altered intestinal spatial organization

We previously showed that wild-type *Vibrio* cells strongly localize to the larval zebrafish foregut (Fig 2A and 2B) [27], which is an anatomical region comparable to the mammalian small intestine (namely, the duodenum and jejunum) [40,41], and display a highly active swimming behavior both within the intestinal lumen and at mucosal surfaces [32]. In contrast, zebrafish symbionts naturally lacking motility within the gut, like *Aeromonas*, form populations that display a posterior-shifted spatial distribution and a high degree of luminal aggregation [27,32]. Thus, the impaired competitiveness of Δmot and Δche against *Aeromonas* (Fig 1C) could be associated with changes in their intestinal spatial organization.

Fig 2. Motility and chemotaxis mutants have altered intestinal spatial organization. (A) Cartoon of a 6-day-old zebrafish. Dashed box marks intestinal region imaged by LSFM. (B) Anatomical regions of the larval zebrafish intestine. (C) Maximum intensity projections acquired by LSFM showing the spatial organization of wild-type *Vibrio* (top), Δmot (middle), and Δche (bottom) within the intestine. Top right inset shows a zoomed-in view of wild-type *Vibrio* cells in a separate fish that was colonized with a 1:100 mixture of green- and red-tagged variants so that the cellular organization of the dense *Vibrio* population could be discerned. The dilute channel (green) is shown. Dashed lines mark approximate intestinal boundaries. Open arrowheads: single bacterial cells; solid arrowheads: small aggregates; tailed arrowheads: large aggregates. Arrowheads with a black stroke mark swimming cells, which appear as comet-like streaks. (D) Cartoon showing the intestinal region pictured in panel (E). (E) Maximum intensity projections acquired by LSFM showing transverse view of the foregut

region colonized with wild type, Δ mot, or Δ che. (F) Fraction of planktonic cells contained within each strain's population. Each circle is a measurement from a single intestinal population. Bars denote medians and interquartile ranges. Letters denote significant differences. $p < 0.05$, Kruskal-Wallis and Dunn's multiple comparisons test. (G) Image-derived abundances of wild type ($n = 7$), Δ mot ($n = 4$), and Δ che ($n = 5$) with respect to position along the length of the gut. Shaded regions mark confidence intervals. Underlying data plotted in F and G are provided in S1 Data.

To determine how motility and chemotaxis affect *Vibrio*'s cellular behavior and spatial organization within the intestine, we examined wild type, Δ mot, and Δ che in live animals using LSFM. A fluorescently marked variant of each strain was first mono-associated with germ-free animals and then imaged at 48 hpi. In line with our previous characterizations [26,27], wild-type *Vibrio* assembled dense populations concentrated within the foregut that were almost entirely composed of planktonic cells swimming in the lumen as well as within the intestinal folds (Fig 2C–2G, S1 and S2 Mov). A movie representation of the static image presented in Fig 2C “wt” under “foregut region” was previously published and can be viewed here: <https://doi.org/10.6084/m9.figshare.7040309.v1> [26]. In contrast, Δ mot and Δ che assembled populations with greatly altered behavior and spatial organization.

Populations of Δ mot were non-motile whereas Δ che had a small subset of motile cells that could often be observed in the foregut (Fig 2C, S1 Mov). Both Δ mot and Δ che also became highly aggregated within the intestine (Fig 2C–2E) despite exhibiting no signs of aggregation during in vitro culture (S1B and S1C Fig). In S1 Mov we provide a live representation of Δ che within the midgut to emphasize its aggregated form within this intestinal region. The fraction of

planktonic cells contained within each mutant population within the intestine was \approx 10-fold lower than wild type (Fig 2F). The aggregated cells of Δ mot appeared to be mostly restricted to the lumen whereas the swimming cells of Δ che, like wild type, were observed within the intestinal folds (Fig 2D and 2E, S2 Mov). The Δ mot mutant was also largely excluded from the anterior most portion of the foregut whereas Δ che often formed a layer of cells associated with the anterior wall near the esophageal-intestinal junction (Fig 2C). The population-wide aggregation of both mutants (which we refer to as cohesion) coincided with an overall posterior-shift in distribution compared to wild type (Fig 2C and 2G). This shift in distribution is consistent with previous findings of strong correlations across bacterial species between cohesion and localization along the zebrafish intestine [27]. In total, our live imaging data show that *Vibrio* requires swimming motility and chemotaxis to spatially organize its populations within the intestine. Further, Δ mot and Δ che formed aggregated and lumen-restricted populations reminiscent of zebrafish bacterial symbionts that largely lack swimming motility *in vivo* [26,27].

B.3.3. Swimming motility and chemotaxis promote persistence by enabling bacteria to counter intestinal flow and resist expulsion

We previously found that naturally aggregated bacteria are vulnerable to intestinal flow and expulsion from the host [32,33]. To explore if the attenuated colonization phenotypes of Δ mot and Δ che are connected to their perturbed spatial organization in a way that causes increased sensitivity to the intestine's mechanical forces, we followed the spatiotemporal dynamics of wild-type *Vibrio* and each mutant in live animals by LSFM. Prior to imaging, each strain was given 24 h to reach its respective carrying capacity in germ-free zebrafish. Despite wild-

type Vibrio showing modest declines in abundance from 24–72 hpi (Fig 1A), it was highly uniform and stable over periods of ≥ 10 h, maintaining its abundance, low cohesion, and foregut localization (Fig 3A, S3 Mov). We note that image-based quantification of wild-type Vibrio abundances was performed in a concurrent study [33] and have been replotted here. In contrast, Δmot and Δche underwent dramatic fluctuations in their abundances and spatial organization (Fig 3A, S3 Mov). Cells and small aggregates in Δmot and Δche populations appeared to become packed by intestinal contractions into large masses within the midgut before being abruptly expelled. Autofluorescent material was often observed surrounding aggregated cells, suggesting that host mucus was involved in this process. Image-based quantification of absolute abundances showed that $\geq 90\%$ of Δmot and Δche populations could be lost in a single collapse event (Fig 3A). Following collapses, residual small aggregates in the midgut and low numbers of planktonic cells in the foregut appeared to undergo bursts in replication that effectively restored the abundance and spatial organization of the population before the next collapse. Notably, this pattern of aggregation, collapse, and regrowth mirrors other non-motile symbiont populations, namely, those formed by zebrafish-derived *Aeromonas* and *Enterobacter* species [32,33]. Animating the relationship between cohesion and intestinal localization for each Vibrio strain across animals over time showed that both mutant populations exhibit large fluctuations in spatial organization whereas wt Vibrio populations are highly stable (S4 Mov).

Fig 3. Swimming motility and chemotaxis promote persistence by enabling bacteria to counter intestinal flow and resist expulsion. (A) Image-based quantification of abundances over time for wild-type Vibrio, Δmot , and Δche . Lines represent individual populations in individual fish. (B) Cultivation-based

quantification of abundances for Δ mot and Δ che in co-housed ret-/- mutant hosts and wild-type/heterozygous sibling controls (sib). Abundances of wild-type Vibrio, Δ mot, and Δ che in wild-type hosts (from Fig 1A, 72 hpi) are shown for comparison. Bars denote medians and interquartile ranges. Letters denote significant differences. $p \leq 0.05$, Kruskal-Wallis and Dunn's multiple comparisons test. Underlying data are provided in S1 Data.

Our live imaging results suggested that the altered spatial organization of Δ mot and Δ che populations, namely their increased cohesion, makes them more susceptible to intestinal flow and expulsion, and thus is likely the cause of their reduced abundances. This putative mechanism contrasts with the general assumption that swimming motility and chemotaxis primarily promote bacterial growth by facilitating nutrient foraging and avoidance of hostile environments. To probe the likelihood of these two different mechanisms we quantified the *in vivo* exponential growth rates of Δ mot and Δ che (see Methods). We found that both Δ mot and Δ che exhibit exponential growth rates within the intestine (Δ mot = 0.7 ± 0.3 hr⁻¹ [n = 2]; Δ che = 0.9 ± 0.4 hr⁻¹ [n = 5]) that are comparable to a previously determined wild-type Vibrio exponential growth rate of 0.8 ± 0.3 hr⁻¹ (mean \pm standard deviation) [32]. This result supports the idea that the reduced intestinal abundances of Δ mot and Δ che are not due to attenuated growth, but rather are a consequence of altered behavior and spatial organization that increases susceptibility to intestinal flow and expulsion.

To test this expulsion-based mechanism more directly, we assessed whether the abundance of Δ mot and Δ che could be rescued in ret-/- mutant zebrafish hosts, which have reduced intestinal transport due to a dysfunctional enteric nervous system [32,42]. Humans with ret mutations can develop Hirschsprung

Disease, which is an affliction characterized by intestinal dysmotility and altered gut microbiome composition [43,44]. Strikingly, we found that the intestinal abundances of both Δ mot and Δ che were fully rescued to wild-type levels in ret-/ mutant animals (Fig 3B). In contrast, Δ mot and Δ che abundances in co-housed sibling control animals mirrored those in wild-type animals (Fig 3B). Importantly, we found that wild-type Vibrio shows no change in intestinal abundance in ret-/ mutant animals (S2A Fig), indicating that the rescue of Δ mot and Δ che is not due to a general overgrowth phenomenon. In addition, inspecting the spatial organization of Δ mot in ret-/ mutant animals revealed that in some instances Δ mot populations displayed relocalization to the anterior portion of the foregut, suggesting that intestinal flow is responsible for Δ mot's posterior-shifted distribution in wild-type animals (S2B Fig). Together, these results provide further evidence that swimming motility and chemotaxis do not promote persistence by affecting growth per se but by enabling bacterial cells to physically resist intestinal flow and expulsion from the host.

B.3.4. Sustained swimming motility is required for maintaining intestinal spatial organization and persistence

Without swimming motility, Vibrio has clear defects in both immigration and intestinal persistence. Therefore, we sought to experimentally separate the roles motility plays during these different stages of colonization. We specifically wanted to determine whether Vibrio requires sustained motility for intestinal persistence or if the impaired immigration and altered assembly of motility mutant populations was in some way responsible for their aggregated and collapsing phenotype. To accomplish this, we built a motility “loss-of-function” switch that uses inducible

CRISPR interference (CRISPRi) to suppress transcription of the flagellar motor gene operon pomAB (Fig 4A and S3 Fig). The motility loss-of-function switch is based on a tetracycline induction system in which a constitutively expressed Tet repressor protein (TetR) is used to regulate the expression of a catalytically dead Cas9 (dCas9). We incorporated a constitutively expressed single guide RNA (sgRNA) to target dCas9 to the 5' end of the native pomAB locus where it would block transcriptional elongation. To visually track switch activity in bacterial populations, we co-expressed dcas9 with a gene encoding superfolder green fluorescent protein (sfGFP) (Fig 4A). To mark all cells independent of switch activity, we co-expressed a gene encoding dTomato with tetR. Details on switch design and optimization are provided in the Methods and in S3A–S3D Fig. We integrated the motility loss-of-function switch into the genome of wild-type *Vibrio* (creating VibriomotLOF) and confirmed that induction of the switch with the tetracycline analog anhydrotetracycline (aTc) robustly inactivates swimming motility in vitro without perturbing growth (S3E and S3F Fig).

Fig 4. Sustained swimming motility is required for maintaining intestinal spatial organization and persistence. (A) Schematic of CRISPRi-based motility loss-of-function (LOF) switch. Lower left table summarizes switch activity and bacterial behaviors plus/minus aTc. Bent arrows denote promoters, “T” denotes transcriptional terminators. Solid lines represent constitutive interactions, dashed lines represent induced interactions. (B) Experimental timelines used to investigate in situ inactivation of swimming motility. (C) A maximum intensity projection acquired by LSFM of an animal colonized by VibriomotLOF at 6 h post-induction. Dashed line mark approximate intestinal boundaries. An arrowhead with a black stroke marks an area of swimming cells expressing only dTomato (magenta,

“switch = OFF”). White tailed arrowheads mark aggregated cells (green, “switch = ON”). (D) Population center of mass over time for intestinal populations of wild-type *Vibrio* (gray) and VibriomotLOF (magenta/green). Lines are single bacterial populations within individual fish. Vertical dashed line marks time of aTc induction. (E) Abundances of VibriomotLOF at 24 and 48 h post-induction with aTc. Bars denote medians and interquartile ranges. Significant differences determined by Mann-Whitney. Underlying data plotted in D and E are provided in S1 Data.

With the motility loss-of-function switch constructed, we tested if sustained swimming motility is required by established *Vibrio* populations to persist within the intestine using both live imaging and cultivation-based measurements of abundance (Fig 4B). For live imaging, germ-free zebrafish were first colonized to carrying capacity with VibriomotLOF. At 24 hpi, repression of motility was induced by adding aTc to the water of colonized zebrafish hosts. We then performed time series imaging of multiple animals using LSFM. Initially, subpopulations emerged that could be distinguished by their switch activation status, behavior, and spatial organization (S5 Mov). Unswitched motile cells expressing only dTomato displayed a foregut localization pattern typical of wild-type *Vibrio* (Fig 4C). In contrast, we observed non-motile cells expressing GFP becoming aggregated and segregating away from motile populations (Fig 4C). GFP-positive cells within aggregates were more restricted to the intestinal lumen and their arrangement suggested they were encased in mucus (Fig 4C and S5 Mov). By 10 hours post-induction, VibriomotLOF displayed clear shifts in population center of mass toward the midgut together with expulsion of multicellular aggregates (Fig 4D).

Cultivation-based measures of absolute abundances revealed that at 24 h post-induction VibriomotLOF populations had a 2.5-fold lower median abundance compared to uninduced controls (Fig 4E). Inducing for an additional 24 h resulted in a 5-fold reduction in median intestinal abundance (Fig 4E). Together, our experiments using the motility loss-of-function switch demonstrate that *Vibrio* requires sustained swimming motility to maintain its spatial organization and to persist at high levels. Our results also reveal that relatively brief interruptions in *Vibrio*'s swimming behavior are capable of producing rapid and dynamic changes in spatial organization and drops in abundance.

B.3.5. Acquisition of swimming motility or chemotaxis leads to rapid recovery of intestinal spatial organization and abundance

We next asked whether established Δmot and Δche populations could recover their spatial organization and abundance if they reacquired swimming motility or chemotaxis, respectively. Answering this question would give insight into the capacity of resident gut bacteria and would-be pathobionts to exploit a sudden loss of host spatial control. Using the motility loss-of-function switch backbone, we constructed motility and chemotaxis “gain-of-function” switches by inserting either *pomAB* or *cheA2* in place of *dcas9* (Fig 5A). The motility and chemotaxis gain-of-function switches were integrated into the genomes of Δmot and Δche , respectively, creating ΔmotGOF and ΔcheGOF . In vitro tests showed that inducing the gain-of-function switches restored wild-type swimming behaviors in each strain without altering growth (S4A–S4C Fig). Moreover, activation of motility and chemotaxis prior to colonization produced intestinal abundances at 24 hpi that matched the carrying capacity of wild type (Fig 5B). These functional

tests show that the motility and chemotaxis gain-of-function switches can be used to inducibly complement the Δ mot and Δ che mutants. Moreover, these genetic complementation experiments also show that the colonization phenotypes of Δ mot and Δ che were not due to off-target or polar effects resulting from our chromosomal manipulations.

Fig 5. Acquisition of swimming motility or chemotaxis leads to rapid recovery of intestinal spatial organization and abundance. (A) Schematic of the motility and chemotaxis gain-of-function (GOF) switches. Table summarizes switch activity and bacterial behaviors plus/minus aTc. (B) Δ motGOF or Δ cheGOF abundances 24 hpi plus/minus aTc. Δ motGOF and Δ cheGOF were pre-induced overnight in liquid culture prior to inoculation, aTc was maintained in the water for continuous switch activation. Abundances of wild-type Vibrio, Δ mot, and Δ che in wild-type hosts (from Fig 1A, 24 hpi) are shown for comparison. Bars denote medians and interquartile ranges. Letters denote significant differences. $p \leq 0.05$, Kruskal-Wallis and Dunn's multiple comparisons test. (C) Probability densities showing the spatial distributions of Δ motGOF and Δ cheGOF at 24 h post-induction. Magenta = uninduced, green = induced. Shaded regions mark standard errors. Sample sizes (populations within individual animals): Δ motGOF "OFF", $n = 5$; Δ motGOF "ON", $n = 7$, Δ cheGOF "OFF", $n = 6$; Δ cheGOF "ON", $n = 6$. (D) Maximum intensity projections acquired by LSFM from the same animal showing Δ cheGOF undergoing rapid changes in spatial organization following induction. Dashed lines mark approximate intestinal boundary. (E) Abundances of Δ motGOF and Δ cheGOF over time. Magenta and green circles indicate abundances plus/minus aTc, respectively. Plotted are medians and interquartile ranges ($n \geq 19$ animals/marker). Abundances of wild-type Vibrio,

Δmot , and Δche (from Fig 1A) are shown for comparison. Significant differences between each mutant and wild-type determined by Mann-Whitney (magenta asterisks: uninduced; green asterisks: induced). *** $p < 0.0001$, ns = not significant. Underlying data plotted in B, C, and E are provided in S1 Data.

We monitored the response dynamics of activating swimming motility or chemotaxis in established populations following similar experimental timelines as depicted in Fig 4B. Live imaging revealed that induced populations of ΔmotGOF and ΔcheGOF underwent clear shifts in spatial distribution toward the foregut within the first 24 h of induction compared to uninduced controls (Fig 5C). Strikingly, ΔmotGOF and ΔcheGOF showed that large-scale changes in behavior and spatial organization could occur extremely rapidly, with both populations becoming more space-filling and foregut-localized within hours (Fig 5D, S6 and S7 Movs). Cultivation-based measurements of absolute abundances showed only modest increases in median intestinal abundances in the first 24 h of induction (Fig 5E, 48 hpi). However, by 48 h post-induction the median intestinal abundances of ΔmotGOF and ΔcheGOF populations had recovered to wild-type levels (Fig 5E, 72 hpi). Therefore, regaining swimming behavior and undergoing spatial reorganization preceded the recovery of intestinal abundance.

Surprisingly, uninduced control populations of ΔmotGOF and ΔcheGOF also exhibited a recovery in intestinal abundance by 72 hpi (S4D Fig). In vitro characterization and DNA sequencing revealed that this spontaneous recovery was likely due to non-synonymous mutations in tetR that were acquired during intestinal colonization and impaired the function of the Tet repressor protein, thus resulting in constitutive switch activation. While unexpected, we surmise that the extremely rapid sweep of “evolved clones” carrying disabled switches—which were

rarely observed in induced populations or the aqueous environment outside the host (S4E Fig)—is evidence of strong selective pressures for motility traits within the gut.

B.3.6. Motile bacterial cells within the intestine induce local and systemic tnfa expression

We next set out to connect *Vibrio*'s motility-based lifestyle to its pathogenic potential. We recently showed that overgrowth of *Vibrio*-related taxa sparks intestinal pathology marked by increased epithelial hypertrophy and neutrophil influx that is dependent on tumor necrosis factor alpha (TNF α) signaling [34]. We further identified that *Vibrio* ZWU0020 on its own can potently stimulate inflammation [36] and exacerbate pathology in susceptible hosts [34]. To explore the link between *Vibrio*'s motility behaviors and its inflammatory potential, we used LSFM and transgenic zebrafish hosts that express GFP under the control of the TNF α promoter (Tg(tnfa:GFP)) [45].

Germ-free animals displayed little tnfa reporter activity in or near the foregut where the bulk of wild-type *Vibrio* cells typically reside (Fig 6A). Similar to previous findings [45], animals colonized with a conventional, undefined microbial community also had low numbers of cells with tnfa reporter activity (Fig 6A). In contrast, at 24 hpi wild-type *Vibrio* induced pronounced tnfa reporter activity in numerous host cells within both the intestine and liver (Fig 6A). All animals colonized with wild-type *Vibrio* had tnfa-expressing cells in or near the liver whereas less than a third of germ-free and conventionalized animals had detectable tnfa reporter activity in this area (Fig 6B). Quantifying fluorescence intensity across the foregut region (including adjacent extraintestinal tissues and the liver)

showed that *Vibrio* induces an approximately 100-fold increase in tnf α reporter activity over germ-free and conventional levels (Fig 6C). In contrast to wild-type *Vibrio*, Δ mot and Δ che elicited muted inflammatory responses. Animals colonized with Δ mot showed a pattern of tnf α reporter activity similar to germ-free animals (Fig 6A–6C). However, despite the comparable intestinal abundances of Δ mot and Δ che (Fig 1A), Δ che induced intermediate, although variable, levels of tnf α reporter activity (Fig 6A–6C). This finding suggests that host tissues do not merely sense bacterial abundances, but also their active swimming behavior and/or proximity to epithelial surfaces. Together, these data provide evidence that swimming motility and chemotaxis are major contributors to *Vibrio*'s proinflammatory potential.

Fig 6. Motile bacterial cells induce local and systemic tnf α expression.
(A) Maximum intensity projections acquired by LSFM of the foregut region of tnf α :GFP transgenic zebrafish raised germ-free, with a complex microbial community (conventionalized), or colonized solely with dTomato-expressing (magenta) wild-type *Vibrio*, Δ mot, or Δ che. Animals were imaged at 24 hpi. Dashed lines mark the approximate intestinal boundaries. Empty arrowheads mark host cells with tnf α :GFP reporter activity. Solid arrowheads mark tnf α :GFP reporter activity in extraintestinal tissues in or near the liver. (B) Percent of zebrafish subjected to different colonization regimes with tnf α :GFP activity in or near the liver. ≥ 6 animals/group were blindly scored by 3 researchers. Bars denote medians and interquartile ranges. gf: germ-free; cvz: conventionalized. (C) Total GFP fluorescence intensity across the foregut region normalized to median gf fluorescence intensity. Bars denote medians and interquartile ranges. Letters denote significant differences. $p \leq 0.05$, Kruskal-Wallis and Dunn's multiple comparisons

test. (D) Maximum intensity projections acquired by LSFM of the foregut region of a tnfa:GFP, mpeg1:mCherry (magenta) transgenic zebrafish colonized with dTomato-expressing wild-type Vibrio (magenta). Animal was imaged at 24 hpi. Open arrowhead indicates a tnfa+/mpeg1+ cell. Underlying data plotted in B and C are provided in S1 Data.

We next probed the possible host cell types involved in sensing motile Vibrio populations. The amoeboid morphology and migratory behavior of many tnfa-expressing cells hinted that they might be immune cells (Fig 6A and S8 Mov). Using double transgenic zebrafish carrying the tnfa reporter and expressing fluorescently marked macrophages (*Tg(mpeg1:mCherry)* [46]), we quantified the fraction of tnfa-positive macrophages within the foregut region, which we consider here as a field of view containing the foregut and adjacent tissues such as the liver. We found that half ($54 \pm 10\%$ [mean \pm standard deviation, $n = 100$ cells from 4 animals]) of the tnfa-positive cells in the foregut region induced by Vibrio were indeed macrophages (Fig 6D and S9 Mov). Nearly all tnfa-positive cells that were directly associated with the foregut were macrophages ($93 \pm 12\%$ [mean \pm standard deviation, $n = 18$ cells from 3 animals]). In contrast, the majority of tnfa-positive cells associated within the liver did not appear to be macrophages based on mpeg1:mCherry expression, nor were they neutrophils (based on experiments with animals carrying an mpx:mCherry reporter), suggesting that they were other non-immune cell types. Collectively, our data indicate that wild-type Vibrio populations stimulate expression of tnfa locally within intestinal tissues as well as at systemic sites, namely the liver. Macrophages are also one of the main cell types that is sensitive to Vibrio colonization.

B.3.7. Host tissues rapidly respond to sudden increases in bacterial swimming motility within the intestine

To maintain homeostasis, the host must be simultaneously tolerant and sensitive to the activity of resident bacterial populations. It is crucial for host tissues to quickly differentiate between harmful and benign changes in the intestinal microbiota; for example, the overgrowth of a pathobiont versus diurnal fluctuations in commensal bacteria [47]. Therefore, we next determined if sudden increases in bacterial motility behaviors—which are a potential signature of pathobionts escaping host control—could elicit an equally rapid host response.

Following a similar live imaging timeline as depicted in Fig 4B, we used LSFM to track tnfa reporter activity in response to induced populations of Δ motGOF. As expected, at time zero Δ motGOF populations displayed low abundance, high cohesion, and a posterior-shifted distribution with little tnfa reporter activity in host tissues (Fig 7A–7C). By 24 h post-induction, Δ motGOF populations had begun to spatially reorganize within the foregut and contained an increased number of swimming cells (Fig 7A). At the same time, there was an increase in tnfa-expressing host cells near the intestine, which were likely macrophages (Fig 7A). In one instance, we captured tnfa-positive host cells within the mucosa adjacent to bacterial cells actively swimming near the epithelial surface (S10 Mov). After the first 24 h of induction, the fraction of animals with tnfa-positive cells in or near the liver did not increase appreciably (Fig 7B); however, there was a 2.5-fold increase in median tnfa reporter activity, implying that initial responses to changes in bacterial swimming motility occur locally within intestinal tissues (Fig 7C). By 48 h of switch induction, Δ motGOF populations exhibited wild-type-like space-filling properties and foregut-localization (Fig 7A).

Likewise, tnfa reporter activity was also mostly restored to wild-type levels (Fig 7B and 7C). Nearly all animals (92%, n = 17) had tnfa-positive cells in or near the liver and the median tnfa reporter activity across the foregut region was 20-fold higher than germ-free levels (Fig 7B and 7C). Our data reveal that host tissues are remarkably sensitive to sudden increases in bacterial motility behaviors that occur over relatively short time scales.

Fig 7. Host tissues rapidly respond to sudden increases in bacterial swimming motility within the intestine. (A) Maximum intensity projections acquired by LSFM of the foregut region of separate tnfa:GFP transgenic zebrafish colonized with Δ motGOF (magenta). Dashed lines mark approximate intestinal boundaries. Times are hours post-switch induction. Solid arrowhead marks bacterial aggregates, empty arrowhead marks single bacterial cells. (B) Percent of zebrafish subjected to different colonization regimes with tnfa:GFP activity in or near the liver. ≥ 4 animals/group were blindly scored by 3 researchers. Bars denote medians and interquartile ranges. Data from animals colonized with wild-type Vibrio (wt) or Δ mot (from Fig 6B) are shown for comparison. Horizontal dashed lines mark gf range plotted in Fig 6B. (C) Total GFP fluorescence intensity across the foregut region normalized to median gf fluorescence intensity plotted in Fig 6C, horizontal dashed lines mark gf range. Bars denote medians and interquartile ranges. Data from animals colonized with wild-type Vibrio (wt) or Δ mot (from Fig 6C) are shown for comparison. Letters denote significant differences. $p \leq 0.05$, Kruskal-Wallis and Dunn's multiple comparisons test. Underlying data plotted in B and C are provided in S1 Data.

B.4. Discussion

Our study connects the motile lifestyle of a gut bacterial symbiont to its colonization and proinflammatory potential. All gut bacteria must contend with host-mediated restrictions on microbiota spatial organization [48–50]. The mechanism by which *Vibrio* maintains stable colonization involves resisting intestinal flow through sustained swimming and chemotaxis. Conventional wisdom is that motility promotes the growth of bacteria by enabling them to forage nutrients and avoid hostile environments [14,17,18]. In contrast, our data show that *Vibrio*'s motility behaviors within the zebrafish gut do not enhance its exponential growth rate but rather allow it to resist intestinal expulsion. *Vibrio* thus provides a model of intestinal persistence that is distinct from more familiar examples involving adhesion to or invasion of host tissues, which are largely based on the examination of dissected and fixed samples and do not consider large-scale dynamics that play out across the entire gut [51–53]. Ultimately, *Vibrio*'s colonization strategy uses continuous swimming to remain in place within the host's intestine.

Vibrio's swimming behavior underlies many of its pathobiont characteristics, including its ability to invade and displace resident bacteria, persist at high abundances, and stimulate host inflammation. The basis of *Vibrio*'s inflammatory activity is presently unknown. On the host side, our work implicates macrophages as a host cell type that is capable of responding to *Vibrio*'s motile behavior through the upregulation of TNF α , but whether the mechanism of sensing *Vibrio* is direct or indirect remains to be determined. We also observed other host cells at systemic sites, particularly within the liver, that upregulate TNF α in response to wild-type *Vibrio* colonization. Transcriptional profiling (e.g., via single-cell RNA sequencing)

and transgenic animals carrying genetic reporters will be useful for probing the identity of these additional host cell types as well as the receptor(s) and signaling cascades involved in sensing *Vibrio* populations.

On the bacterial side, future work is aimed at testing how host inflammation is connected to *Vibrio*'s abundance, position along the intestine, mucosal proximity, and cellular behavior. Intriguingly, the different inflammatory activities of Δ mot and Δ che, despite their similar spatial organizations and production of flagella, highlights the possibility that the mechanism involves active bacterial motility. We posit that motility allows bacteria to access epithelial surfaces, increasing concentrations of inflammatory molecules at host cell surfaces and possibly triggering mechanosensory pathways. For example, flagellar rotation itself has been shown to increase the shedding of immunogenic lipopolysaccharide and outer membrane vesicles in other *Vibrio* lineages [54,55]. It is also possible that the Δ mot and Δ che mutants differ from wild-type in their level of expression of inflammatory flagellar components despite displaying intact flagella *in vitro*.

Vibrio's colonization dynamics show how swimming motility and chemotaxis enable gut bacteria to evade spatial constraints imposed by the host. Notably, Δ mot and Δ che reveal how bacteria with impaired motility surrender to intestinal mechanics, which act to confine them within the lumen where they can be periodically purged. The aggregation of Δ mot and Δ che within the intestine was unexpected, especially for Δ che, which displays vigorous swimming *in vitro*. It is possible that both mutants experience shifts in metabolism or induce biofilm behaviors *in vivo* as a consequence of their inability to effectively control their spatial distribution. It is also possible that the aggregation of Δ mot and Δ che stems from a defect in flagellar assembly or signaling, which could be disentangled

using mutants lacking flagella altogether. Alternatively, Δmot and Δche cells may become entrapped within intestinal mucus and grow locally to produce small clonal aggregates that are subsequently consolidated into larger aggregates by intestinal mechanics before being collectively expelled. Corroborating this idea, it was shown in an infant mouse model that the attenuated colonization of a human-derived isolate of *V. cholerae* lacking motility can largely be reversed in animals that are pre-treated with a mucolytic agent that disrupts mucus architecture [56]. Furthermore, it is possible that the swimming activity of Δche may actually facilitate mucus entrapment. It has been shown that non-chemotactic, straight-swimming bacterial cells that are unable to periodically redirect their swimming trajectory can become jammed within a porous medium (such as in a soft agar matrix commonly used to study chemotaxis *in vitro*) [57]. We propose that a similar mechanism could lead to entrapment and aggregation of Δche cells within intestinal mucus, which wild-type *Vibrio* cells avoid because they are able to actively escape from mucus through regular changes in swimming direction mediated by chemotactic signaling.

More broadly, our study supports the idea that in addition to the intestine's role in transporting digesta and expelling waste, intestinal flow and mucus dynamics also appear to exert spatial and population control over non-motile and non-chemotactic resident microbiota. Consistent with this, our previous characterization of *sox10* mutant zebrafish demonstrated how the enteric nervous system can prevent microbiome-mediated inflammation and pathology by constraining intestinal bacterial abundances and composition [34]. Further, we recently showed that intestinal mechanics can amplify the impact of sublethal antibiotic treatment on gut bacteria, which induces bacterial aggregation and thus,

leads to enhanced intestinal expulsion [33]. A similar phenomenon was described in the mouse intestine, where antibody-mediated en chaining of bacterial cells enhanced clearance of *S. Typhimurium* [58]. Our observation that intestinal flow impacts the distribution of bacteria throughout the gut is also corroborated by findings in “gut-on-a-chip” fluidic systems [59].

Given the clear advantage of motility behaviors within the gut, it is somewhat surprising that the majority of zebrafish gut bacteria studied so far—many of which are capable of flagellar motility—form aggregated populations made up of mostly non-motile cells [26]. This discrepancy may be reconciled by considering the broader ecological life cycles of gut bacteria. For example, we have found that intestinal populations of *Aeromonas* grow more rapidly within multicellular aggregates than as planktonic cells [60]. Moreover, *Aeromonas* also benefits from swimming motility during interhost dispersal [37]. *Aeromonas* thus highlights how aggregation and expulsion by intestinal flow may actually facilitate growth and transmission in the context of a population of hosts [61]. Bacterial aggregation may also be part of a bacterial strategy for preventing host inflammation and avoiding subsequent antimicrobial responses. Supporting this idea, we recently found that several aggregated *Aeromonas* species are sensitive to host inflammation [62]. In contrast, the particular *Vibrio* strain used in the present work is largely tolerant to host inflammation [36] and thus, can stimulate host inflammatory responses without consequence.

Further investigation of the relationship between intestinal mechanics and gut bacterial lifestyles will open new avenues for therapeutic engineering of the gut microbiome. Our findings suggest that manipulating bacterial motility and aggregation may be used to induce large-scale, yet specific, changes in both

bacterial abundances and host inflammatory state. Moreover, using drug- or diet-based modulators of intestinal flow may enhance the efficacy of antibiotics or promote microbiome recovery and fortification following perturbation. Our experiments using genetic switches to toggle bacterial motility and inflammatory activity serve as a proof-of-concept for these types of manipulations. Highlighting the potential of these interventions, human studies have shown that colonic transit time is a top predictor of microbiome composition [63,64]. Moreover, impaired intestinal flow can lead to bacterial overgrowth and pathogenic changes in the microbiome [34,44,65]. Considering the dynamic nature of the intestinal ecosystem on spatial and temporal scales relevant to bacterial cells will be key to therapeutically engineering the microbiome.

B.5. Methods

B.5.1. Ethics statement

All experiments with zebrafish were done in accordance with protocols approved by the University of Oregon Institutional Animal Care and Use Committee and following standard protocols (protocol number 15-98) [66]. Specific handling and housing of animals during experiments are described in detail under the section “Gnotobiology”. All zebrafish used in this study were larvae, between the ages of 4- and 7-days post-fertilization. Sex differentiation occurs later in zebrafish development and thus was not a factor in our experiments.

B.5.2. Zebrafish lines

Zebrafish lines used in this study included: University of Oregon stock wild-type ABCxTU; zebrafish carrying the ret1hu2846 mutant allele [32,42];

zebrafish carrying the Tg(tnfa:GFP) transgene [45]; and zebrafish carrying the Tg(mpeg1:mCherry) transgene [46]. Double transgenic animals included Tg(tnfa:GFP) x Tg(mpeg1:mCherry) and Tg(tnfa:GFP) x Tg(mpx:mCherry) [67]. Of note, ret1hu2846 is recessive and adult zebrafish carrying this mutant allele were maintained as heterozygotes. Incrossing ret1hu2846 animals produces ret+/+, ret+/-, and ret-/- individuals. ret-/- larvae can be visually distinguished from ret+/+ and ret+/- larvae based on developmental features. In our study we classified ret+/+ and ret+/- larvae together as “sibling” controls.

B.5.3. Bacterial strains and culture

B.5.3.1. General

All wild-type and recombinant bacterial strains used or created in this study are listed in S1 Table. Archived stocks of bacteria are maintained in 25% glycerol at -80°C. Prior to manipulations or experiments, bacteria were directly inoculated into 5 ml lysogeny broth (10 g/L NaCl, 5 g/L yeast extract, 12 g/L tryptone, 1 g/L glucose) and grown for 16 h (overnight) shaking at 30°C. For growth on solid media, tryptic soy agar was used. Gentamicin (10 µg/ml) was used to select recombinant Vibrio strains during their creation (for both gene deletion and insertion variants). Ampicillin (100 µg/ml) was used for maintaining plasmids in *E. coli* strains.

B.5.3.2. In vitro growth measurements

In vitro growth of bacterial strains was assessed using the FLUOstar Omega microplate reader. Prior to growth measurements, bacteria were grown overnight in 5 ml lysogeny broth at 30°C with shaking. The next day, cultures

were diluted 1:100 into fresh lysogeny broth (aTc was added to the media when switch induction was required) and dispensed in triplicate or quadruplicate (i.e., 3–4 technical replicates) (200 μ l/ well) into a sterile 96 well clear flat bottom tissue culture-treated microplate. Absorbance measurements at 600 nm were recorded every 30 min for 16 h (or until stationary phase) at 30°C with shaking. Growth measurements were repeated at least two independent times for each strain (i.e., two biological replicates) with consistent results. Data plotted are from a single replicate.

B.5.3.3. In vitro motility assays

The swimming behavior of each *Vibrio* strain was assessed using soft agar assays and live imaging of bacterial motility in liquid media on glass slides. For soft agar assays, bacteria were first grown overnight in 5 ml lysogeny broth at 30°C with shaking. One milliliter of bacterial culture was then washed by centrifuging cells at 7,000 x g for 2 minutes, aspirating media, and suspending in 1 ml 0.7% NaCl. This centrifugation and aspiration wash step was repeated once more and bacteria were suspended in a final volume of 1 ml 0.7% NaCl. One microliter of washed bacterial cells was inoculated into swim agar plates made of tryptic soy agar containing 0.2% agar. In the case of Δ motGOF and Δ cheGOF, aTc was also added to the agar at the indicated concentrations. Swim plates were incubated at 30°C for 6 h and imaged using a Gel Doc XR+ Imaging System. For live imaging of swimming behavior, bacteria were first grown overnight in 5 ml lysogeny broth at 30°C with shaking. The next day, cultures of wild-type *Vibrio*, Δ mot, and Δ che were diluted 1:100 in tryptic soy broth and grown for 2 h with shaking at 30°C. Δ motGOF and Δ cheGOF were diluted 1:100 in tryptic soy broth +/– 50 ng/ml

aTc and grown for 4 h with shaking at 30°C. VibriomotLOF was diluted 1:1000 in tryptic soy broth +/- 50 ng/ml aTc and grown for 7 h with shaking at 30°C. Prior to imaging, bacteria were diluted 1:40 in tryptic soy broth, mounted on glass slides with a coverslip and imaged for 10 s using a Nikon Eclipse Ti inverted microscope equipped with an Andor iXon3 888 camera. Representative maximum intensity projections of 10 s movies shown in S1, S3, and S4 Figs were generated in FIJI [68]. For measurements of swimming behavior, bacteria were tracked using the radial center algorithm [69] for object localization and nearest-neighbor linking. Motility assays were repeated at least two independent times (i.e., two biological replicates) with consistent results.

B.5.3.4. Scanning electron microscopy

Bacteria were prepared for environmental scanning electron microscopy (ESEM) by first growing cells on tryptic soy agar overnight at 30°C. A sterile inoculating loop was used to transfer 100 μ l of cells to a 1.6 ml tube containing 500 μ l of 3% glutaraldehyde fixative. We visually confirmed that Vibrio cells isolated from an agar plate are highly motile and thus capable of producing flagella during culture on solid media. Cells were fixed overnight at 4°C. The next day, cells were sequentially washed in increasing concentrations of ethanol: first in plain ddH₂O followed by 20%, 40%, 60%, and 80% ethanol. Each wash involved centrifuging cells at 7,000 x g for 2 minutes, aspirating media, and suspending in the next wash medium. A small aliquot of washed cell suspension was applied to a silicon wafer, dried, and imaged using a FEI Quanta 200 ESEM/VPSEM environmental scanning electron microscope provided by the University of Oregon's Center for Advanced Materials Characterization in Oregon (CAMCOR) facility.

B.5.3.5. Disk diffusion assays

Disk diffusion assays were often used to test and optimize dTomato and sfGFP reporter function of genetic switches as described in S3C and S3D Fig. Bacteria were first grown overnight in 5 ml lysogeny broth at 30°C with shaking. One hundred microliters of dense overnight culture were spread onto tryptic soy agar plates to produce a lawn of growth. Prototyping was typically done using plasmid-base switches in *E. coli* (as was the case in S3C and S3D Fig), thus tryptic soy agar plates also contained ampicillin to ensure plasmid maintenance. A sterile piece of Whatman filter paper (0.5 cm wide) was placed in the center of the plate and impregnated with 2 µg of aTc. Plates were incubated overnight at 30°C. Switch reporter activity was assessed using a Leica MZ10 F fluorescence stereomicroscope equipped with 1.0x, 1.6x, and 2.0x objectives, and a Leica DFC365 FX camera. Images were captured and processed using standard Leica Application Suite software and FIJI [68].

B.5.4. Molecular techniques and genetic manipulations

B.5.4.1. General

Recombinant strains used or created in this study are listed in S1 Table. Plasmids used or created in this study are listed in S2 Table. Primer and oligo DNA sequences are listed in S3 Table.

E. coli strains used for molecular cloning and conjugation were typically grown in 5 ml lysogeny broth at 30°C or 37°C with shaking in the presence of appropriate antibiotic selection to maintain plasmids. For propagation of *E. coli* on solid media, LB agar was used. Unless specified, standard molecular techniques

were applied, and reagents were used according to manufacturer's instructions. Restriction enzymes and other molecular biology reagents for polymerase chain reaction (PCR) and nucleic acid modifications were obtained from New England BioLabs. Various kits for plasmid and PCR amplicon purification were obtained from Zymo Research. The Promega Wizard Genomic DNA Purification Kit was used for isolating bacterial genomic DNA. DNA oligonucleotides were synthesized by Integrated DNA Technologies (IDT). Sanger sequencing was done by Sequetech to verify the sequence of all cloned genetic parts. A Leica MZ10 F fluorescence stereomicroscope with 1.0x, 1.6x, and 2.0x objectives and Leica DFC365 FX camera were used for screening fluorescent bacterial colonies.

Genome and gene sequences were retrieved from "The Integrated Microbial Genomes & Microbiome Samples" (IMG/M) website (<https://img.jgi.doe.gov/m/>) [70]. Where applicable, "IMG" locus tags are provided for genetic loci, which can be used to access sequence information via the IMG/M website.

B.5.4.2. Construction of gene deletions

Markerless, in-frame gene deletions were constructed using allelic exchange and the pAX1 allelic exchange vector (Addgene Plasmid #117397) as previously described [26]. Detailed procedures and protocols can be accessed online: <https://doi.org/10.6084/m9.figshare.7040264.v1>. Creation of Δmot via deletion of pomAB (locus tags: ZWU0020_01568 and ZWU0020_01567) (S1A Fig) was reported previously [26]. Creation of Δche via deletion of cheA2 (locus tag: ZWU0020_00514) (S1A Fig) was accomplished by first constructing a cheA2 allelic exchange cassette using splice by overlap extension (SOE). The cheA2 allelic exchange cassette was designed to fuse the start and stop codons of the cheA2 gene

(S1A Fig). PCR primer pairs WP165 + WP166 and WP167 + WP168 were used to amplify 5' and 3' homology regions flanking the cheA2 gene, respectively, from *Vibrio* ZWU0020 genomic DNA. The resulting amplicons were spliced together and the SOE product was ligated into a pAX1-based allelic exchange vector, producing pAX1-ZWU0020-cheA2 (pTW383). After subsequent subcloning steps, the final sizes of the 5' and 3' homology regions were 763 bp and 845 bp.

The pAX1-ZWU0020-cheA2 vector was delivered into *Vibrio* via conjugation (i.e., bacterial mating) as previously described using *E. coli* SM10 as a donor strain [26]. Briefly, *Vibrio* and SM10/pAX1-ZWU0020-cheA2 were combined 1:1 on a filter disk placed on tryptic soy agar. The mating mixture was incubated at 30°C overnight. Following incubation, bacteria were recovered and spread onto tryptic soy agar containing gentamicin and incubated overnight at 37°C to select for *Vibrio* merodiploids. Merodiploid colonies were isolated and screened for successful deletion of the cheA2 gene. Putative mutants were genotyped by PCR using primers that flanked the cheA2 locus (WP0169 + CheA2.ZW20.KOconfirm.REV), which produced two differently sized amplicons representing the wild-type and mutant alleles (S1A Fig).

B.5.4.3. Design and construction of genetic switches

Customizable, plasmid-based gain-of-function (pXS-GOF-switch, pTW265) and loss-of-function (pXS-LOF-switch, pTW308) switch scaffolds were initially constructed and optimized using the pXS-dTomato (Addgene Plasmid #117387) backbone, which was previously generated [26]. The general architecture of switch elements is depicted in S3A Fig. Each element is flanked by unique restriction sites to allow straightforward insertion of new elements by restriction cloning.

pXS-dTomato contains the “tracker” element, which comprises a constitutive Ptac promoter (without the lac operator sequence) [26] driving the dTomato gene. The “switch reporter” element was first inserted, which comprises a PLtetO promoter [71] driving a sfGFP gene that was amplified from pTW168 using WP138 + WP118. Next, the “repressor” element was inserted, which comprises a tetR gene that was amplified from Enterobacter ZOR0014 genomic DNA using WP146 + WP139. As described in S3B and S3C Fig, a near-random ribosome binding site (ndrrdn) was incorporated by PCR into the 5’ untranslated region of the tetR gene via WP146. A clone containing the ribosome binding site sequence “ctaggt” was isolated that had strong reporter repression/induction and robust tracker expression. Next, as described in S3B and S3D Fig, a ribozyme-based insulator sequence (RiboJ) [72] was inserted between the switch reporter and the insertion site designated to hold switch “cargo” genes. The RiboJ sequence was inserted using a custom synthesized gBlock gene fragment (IDT). The resulting plasmid-based switch scaffold—comprising a tracker, switch reporter, repressor, and RiboJ sequence—became pXS-GOF-switch. To generate pXS-LOF-switch, we inserted the dcas9 gene [73] (excised from pdCAS9, Addgene Plasmid #44249) as the “cargo” element and a constitutively expressed single guide RNA (“sgRNA” element) driven by the CP25 promoter [74], which was inserted using a custom synthesized gBlock gene fragment (IDT). The stock sgRNA that was inserted into the pXS-LOF-switch is based on a previously characterized sgRNA specific for the lacZ gene of *E. coli* [73], which facilitated optimization of loss-of-function switch activity in *E. coli* K-12 (MG1655). To expedite insertion of the gain-of-function and loss-of-function switches into the *Vibrio* chromosome, each switch scaffold was subcloned into the previously described Tn7 delivery vector pTn7xTS (Addgene Plasmid #117389),

creating pTn7xTS-GOF-switch (pTW285) and pTn7xTS-LOF-switch (pTW317).

We note that insertion of the switch scaffolds into the pTn7xTS vector limits some downstream customization due to restriction site conflicts.

To construct the motility loss-of-function switch, the lacZ sgRNA in the pTn7xTS-LOF-switch was replaced with a sgRNA specific for the *Vibrio pomA* gene, creating pTn7xTS-mot-LOF-switch (pTW340). The pomA sgRNA was inserted using a custom synthesized gBlock gene fragment (IDT). To construct the motility gain-of-function switch, the pomAB locus, including the native pomA ribosome binding site, was amplified using WP170 + WP171 and inserted into the cargo site of pTn7xTS-GOF-switch, creating pTn7xTS-mot-GOF-switch (pTW324). To construct the chemotaxis gain-of-function switch, the cheA2 locus, including the native cheA2 ribosome binding site, was amplified using WP92 + WP93 and inserted into the cargo site of pTn7xTS-GOF-switch, creating pTn7xTS-che-GOF-switch (pTW282).

B.5.4.4. Tn7-mediated chromosomal insertions

Chromosomal insertion of fluorescent markers and genetic switches was done via a Tn7 transposon-based approach using the Tn7 delivery vector pTn7xTS as previously described [26]. Detailed procedures and protocols can be accessed online: <https://doi.org/10.6084/m9.figshare.7040258.v1>. Specific pTn7xTS vectors carrying markers or switches were delivered into *Vibrio* via triparental mating using two *E. coli* SM10 donor strains carrying either the pTn7xTS delivery vector or the pTNS2 helper plasmid (Addgene Plasmid #64968). Briefly, *Vibrio* and SM10 donor strains were combined 1:1:1 on a filter disk placed on tryptic soy agar. The mating mixture was incubated at 30°C overnight. Following incubation, bacteria were recovered

and spread onto tryptic soy agar containing gentamicin and incubated overnight at 37°C to select for *Vibrio* insertion variants. Insertion of the Tn7 transposon and the genetic cargo it carried into the attTn7 site near the glmS locus of *Vibrio* was confirmed by PCR using primers WP11 + WP12.

Fluorescently marked wild-type *Vibrio* constitutively expressing dTomato (ZWU0020 attTn7::dTomato) was previously generated using pTn7xTS-dTomato (Addgene Plasmid #117391) [26]. In the current work, fluorescently marked Δ mot and Δ che were constructed in the same way, creating Δ mot attTn7::dTomato and Δ che attTn7::dTomato. VibriomotLOF was created by inserting the motility loss-of-function switch from pTn7xTS-mot-LOF-switch. Δ motGOF was created by inserting the motility gain-of-function switch from pTn7xTS-mot-GOF-switch. Δ cheGOF was created by inserting the chemotaxis gain-of-function switch from pTn7xTS-che-GOF-switch.

B.5.5. Gnotobiology

B.5.5.1. Germ-free derivation

For all experiments, zebrafish embryos were initially derived germ-free using previously described gnotobiotic procedures with slight modification [75]. Briefly, fertilized eggs from adult mating pairs were harvested and incubated in sterile embryo media (EM) containing ampicillin (100 μ g/ml), gentamicin (10 μ g/ml), amphotericin B (250 ng/ml), tetracycline (1 μ g/ml), and chloramphenicol (1 μ g/ml) for 6 h. Embryos were then washed in EM containing 0.1% polyvinylpyrrolidone–iodine followed by EM containing 0.003% sodium hypochlorite. Surface sterilized embryos were distributed into T25 tissue culture flasks containing 15 ml sterile EM at a density of one embryo per milliliter and

kept in a temperature-controlled room at 28–30°C with a 14 h/ 10 h light/dark cycle. The germ-free status of larval zebrafish was assessed before every experiment by visually inspecting flask water for microbial contaminants using an inverted microscope. Culture-based assessment of germ-free status was done as needed by plating 100 μ l flask water on rich media (e.g., tryptic soy agar). Embryos were sustained on yolk-derived nutrients and not fed prior to or during any experiments.

B.5.5.2. Bacterial associations

For bacterial associations, bacterial strains were grown overnight in lysogeny broth with shaking at 30°C and prepared for inoculation by pelleting the cells from 1 ml of culture for 2 min at 7,000 x g and washed once in sterile EM. For all experiments, except where noted otherwise, washed bacteria were inoculated into the water of T25 flasks containing 4-day-old larval zebrafish at a final density of 10⁶ bacteria/ml. For competition experiments, Vibrio strains were added to the water of Aeromonas-colonized zebrafish (at 5-days-old) without removing the original Aeromonas inoculum from the water. In addition, to enable enumeration of Aeromonas and Vibrio strains on agar plates, competition experiments were done using a previously constructed dTomato-expressing Aeromonas strain (Aeromonas attTn7::dTomato) [26]. For loss-of-function and gain-of-function switch experiments involving cultivation-based abundance measurements, prior to aTc-induction zebrafish were washed and placed in sterile EM to ensure that changes in intestinal populations were not interfered with by bacteria in the water. To conventionalize animals (i.e., colonize with a complex, undefined microbial consortium), 0 and 4-day-old larval zebrafish were inoculated with 100 μ l of water taken from parental

spawning tanks. No difference was found between conventionalization times in terms of host tnfa:GFP expression.

B.5.6. Cultivation-based measurement of abundances

Dissection of larval zebrafish guts was done as previously described with slight modification [76]. Briefly, dissected guts of tricaine-euthanized zebrafish were harvested and placed in a 1.6 ml tube containing 500 μ l sterile 0.7% saline and 100 μ l 0.5 mm zirconium oxide beads. Guts were homogenized using a bullet blender tissue homogenizer for 25 seconds on power 4. Lysates were serially plated on tryptic soy agar and incubated overnight at 30°C prior to enumeration of colony forming units and determination of bacterial abundances. Abundance data presented throughout the main text and in S2 Fig are pooled from a minimum of two independent experiments ($n = 16\text{--}36$ dissected guts per condition). Abundance data presented for Δ motGOF and Δ cheGOF without aTc induction in S4 Fig are from a single representative experiment ($n = 8\text{--}10$ dissected guts per condition; water abundances are from single measurements). Samples with zero countable colonies on the lowest dilution were set to the limit of detection (5 bacteria per gut). Data were plotted and analyzed using GraphPad Prism 6 software. Unless stated otherwise, statistical differences between two groups of data were determined by Mann-Whitney; statistical differences between two paired groups of data were determined by Wilcoxon; and statistical differences among three or more groups of data were determined by Kruskal-Wallis test with Dunn's multiple comparisons test.

B.5.7. Live imaging

B.5.7.1. Light sheet fluorescence microscopy

Live larval zebrafish were imaged using a custom-built light sheet fluorescence microscope previously described in detail [60]. Prior to mounting, larvae were anesthetized with MS-222 (tricaine). A metal plunger was used to mount fish into small glass capillaries containing 0.5% agarose gel. Samples were then suspended vertically, head up, in a custom imaging chamber containing embryo media and anesthetic. Larvae in the set gel were extruded from the end of the capillary and oriented such that the fish's left side faces the imaging objective. For experiments involving just fluorescent bacteria, the 1mm long intestine is imaged in four subregions that are registered in software after imaging. A single 3D image of the full intestine volume (200x200x1200 microns) sampled at 1-micron steps between z-planes is imaged in 45 seconds. For experiments including the tnfa:GFP reporter, only one subregion containing the anterior foregut region and 100 microns of tissue anterior to the gut was captured for the majority of samples. In these image stacks, nearly the full extent of the fish's left-right width was captured, approximately 400 microns in z. For time lapse imaging of genetic switch induction, fish were mounted as normal and baseline dynamics were captured for 30-90 min depending on the experiment. Then, the inducer aTc was added to the sample chamber media in an approximately 1 ml solution of embryo media, MS-222, and aTc. Excitation lasers of wavelengths 488 and 561 nm were adjusted to a power of 5 mW as measured before the imaging chamber. An exposure time of 30 ms was used for all 3D scans and 2D movies. Time lapse imaging was performed overnight, except for the additional growth rate measurement for Δ che, which occurred during the day. For

color images presented within figures, autofluorescent tissues—namely, the yolk, swim bladder, and ventral skin—were manually converted to grayscale to enhance clarity.

B.5.7.2. Identification of fluorescent bacteria

Identification of bacteria in zebrafish images was conducted using a previously described computation pipeline written in MATLAB [27,60]. In brief, individual bacteria are first identified with a combination of wavelet filtering [77], standard difference of Gaussians filtering, intensity thresholding, and manual curation. Then, multicellular aggregates, which are too dense to resolve individual cells, are segmented via a graph cut algorithm [78] seeded with an intensity mask. The number of cells per multicellular aggregate is estimated by dividing the total aggregate fluorescence intensity by the mean intensity of single cells. These estimates of number of cells per bacterial object in the gut are then used to compute spatial distributions along the length of the gut, following a manually drawn line drawn that defines the gut’s center axis.

B.5.7.3. Measurement of planktonic fractions

Planktonic fractions were computed for each fish by dividing the number of identified single cells by the total abundance. For wild-type *Vibrio*, the primary population of motile bacteria is typically too dense for us to resolve single cells. However, sparse labelling experiments, in which fish were colonized with GFP- and dTomato-marked *Vibrio* at a ratio of 1:100 (Fig. 2C, top row, right), indicated that this population was indeed entirely planktonic. Movies showing motility of sparsely labelled cells were previously published [26,27]. Therefore, to compute planktonic

fraction for wild-type *Vibrio* in single-labeled populations, we treated the dense, anterior sub-population computationally just like we would an aggregate—using our aggregate detection algorithm and estimating the number of cells present by normalizing the total fluorescence intensity to the mean single cell intensity—but then counted these cells as planktonic.

B.5.7.4. Measurement of *in vivo* growth rates

Through time-lapse imaging and the computational image analysis methods discussed above, bacterial growth rates in the intestine can be directly measured by linear fits to log-transformed abundances [32,33,60]. The *in vivo* growth rate of wild-type *Vibrio* was previously measured [32]. The *in vivo* growth rate for Δ_{mot} was measured in the time traces shown in Fig 3A, using manually defined windows of clear exponential growth. To exclude effects of density dependence on the growth rate, only those traces that began at least 1 order of magnitude below the median Δ_{mot} abundance were considered. For Δ_{che} , the time traces in Fig 3A were insufficient for growth rate estimation, because abundances remained at high levels for most of the experiment. Therefore, we measured the growth rate in populations shortly after initial colonization. Specifically, Δ_{che} was allowed to colonize germ-free fish for 6 hours, after which fish were mounted for time lapse imaging. Previous work on another zebrafish gut bacterial symbiont showed that exponential growth rates in established and nascent populations are equal [32]. Abundance data for these time traces are included in the S1 Data.

B.5.7.5. Quantification of tnfa:GFP fluorescence

Cells and tissues expressing tnfa:GFP were segmented in 3D with basic intensity threshold-based segmentation. A pixel intensity threshold of 1500 was empirically found to be a conservative threshold and was used for all samples. The 488 nm excitation laser power was set at 5 mW prior to entering the sample chamber for all samples. The camera was a pco.edge scientific CMOS camera (PCO, Kelheim, Germany). The resulting identified objects were then filtered by size to remove noise. GFP signal from near the ventral skin was excluded with a manually defined cropped region created in the ImageJ software [68]. Green autofluorescence from the interior gut region rarely passed the intensity and size thresholds to contribute to measured tnfa:GFP signal. Similarly, in the motility gain-of-function switch experiments, we found that the GFP reporter of switch induction never reached fluorescence intensity levels high enough to contribute measurably to the tnfa:GFP signal. Nevertheless, this region was automatically identified and removed via intensity threshold-based segmentation in the red 568/620 nm (excitation/emission) color channel. Both red autofluorescence and signal from red (dTomoTo) fluorescent bacteria were used to identify this gut region. Finally, to standardize total tnfa:GFP quantification across different samples, an operational peri-intestinal region was defined as containing the foregut plus all tissue 100 microns anterior of the start of the gut, which was automatically identified in the mask generated from the red color channel. Automatic gut segmentation and removal was not performed for the dual tnfa:GFP/mpeg1:mCherry reporter fish.

B.5.7.6. Measuring tnfa:GFP/mpeg1:mCherry fluorescence

Red fluorescence from mpeg1:mCherry marking macrophages was segmented analogously to tnfa:GFP signal, using basic intensity threshold-based segmentation in 3D and size filtering. A tnfa+ object and an mpeg+ object were considered to overlap if their centroids were separated by less than 10 microns, a threshold empirically determined to produce accurate results as judged by eye. The fraction of tnfa+ objects that were also mpeg+ and the fraction of mpeg+ objects that were also tnfa+ were computed using the counts for overlapping and non-overlapping cells.

B.5.8. Data and statistical analysis

Data were plotted using MATLAB and GraphPad Prism 6 software. Statistical analyses were done using GraphPad Prism 6. Unless stated otherwise, medians and interquartile ranges were plotted. Statistical tests performed are specified in figure legends and within the Methods under “Cultivation-based measurement of abundances”. A p-value of 0.05 or less was considered significant for all analyses. Sample sizes are noted within the main text, figure legends, within the Methods under “Cultivation-based measurement of abundances”, and in S1 Data (.xls). What “n” represents is specified in the main text and figure legends.

B.6. Acknowledgements

We thank Maria Bañuelos and other members of the Guillemin lab as well as Dr. Judith Eisen and members of her lab for thoughtful discussion throughout this study. We also thank Rose Sockol and the University of Oregon Zebrafish Facility staff for fish husbandry and care.

B.7. Supporting Information

S1 Fig. Motility and chemotaxis mutant construction and in vitro characterization. (A) Gene diagrams depict the in-frame markerless deletion of pomAB (Δ mot construction) and cheA2 (Δ che construction). “ Δ ” denotes the mutant allele and the DNA sequence shown below represents the resulting fusion of the start and stop codons in each case. Black triangles represent primers used for PCR-confirmation of each mutant, and the amplicon sizes (bp) of the wild-type (wt) and mutant (Δ) alleles are provided above each locus. DNA gels to the right of each diagram show the successful deletion of both pomAB and cheA2 from the *Vibrio* chromosome. We note that the Δ mot mutant was constructed in a previous publication [26] and the DNA gel shown is a version of that already published but is included here for continuity and thoroughness. ns: non-specific amplicon. (B) Left: Swimming motility of wild type (wt), Δ mot, and Δ che in liquid media and soft agar. Motility in liquid media was recorded for 10 seconds on a glass slide. Images show cellular movements over the entire 10 second period, which illustrates each cell’s swimming trajectory. Swim distances were captured 6 h post-inoculation of bacteria into the agar. Right: Probability densities showing the distribution of cellular swimming speeds in liquid media for each *Vibrio* strain. Sample sizes (measured bacterial swim tracks): wt = 2,962; Δ mot = 754; Δ che = 3,069. Inspection of cultures before and during analyses provided no obvious indications of elevated in vitro aggregation for Δ mot or Δ che compared to wild type (C) In vitro growth curves of each *Vibrio* strain in rich media (lysogeny broth). Line traces the average optical density (OD) from four replicate wells, bars indicate range. Notably, smooth growth curves reiterate that Δ mot or Δ che do not exhibit elevated aggregation in vitro (D) Scanning electron micrographs of

each *Vibrio* strain after growth on solid media. Images show that each strain is capable of assembling a single polar flagellum. Underlying data plotted in B and C are provided in S1 Data.

S2 Fig. Additional wild-type and Δmot colonization data in ret-/- mutant hosts. (A) Cultivation-based abundances for wild-type *Vibrio* in co-housed ret-/- mutant hosts and wild-type/heterozygous sibling controls (sib). Abundances of wild-type *Vibrio* in wild-type hosts (from Fig 1A, 72 hpi) are shown for comparison. Letters denote significant differences. $p < 0.05$, Kruskal-Wallis and Dunn's multiple comparisons test. (B) Maximum intensity projections acquired by LSFM from a sib control host (top) or a ret-/- mutant host (bottom). Each animal was colonized with Δmot for 72 h prior to imaging. Dashed lines mark approximate intestinal boundaries. Underlying data plotted in A are provided in S1 Data.

S3 Fig. Switch design features and in vitro characterization of the motility loss-of-function switch. (A) Diagram depicts the customizable design of the switch scaffold. Unique restriction sites (rs) flanking switch elements allow each component to be optimized or replaced. The “tracker” encodes a fluorescent protein for marking all bacterial cells. The “repressor” encodes a transcription factor that allows inducible control of “cargo” gene (e.g., dCas9) expression. The “switch reporter” encodes a fluorescent protein that is coexpressed with the cargo gene to signal switch activation. A “sgRNA” is inserted when the switch is used for CRISPRi. (B) Gene diagram indicates the locations (cyan bullseyes) of two elements that were essential for switch function: an optimized tetR ribosome binding site (RBS) and a ribozyme-based insulator. (C) Left: Shown are DNA sequences for the native (top) and functionally optimized (bottom) 5' untranslated region (UTR) of the tetR gene. Underlined cyan text denotes the RBS. Bolded

text marks the tetR start codon. The middle sequence represents the library of tetR 5' UTRs containing randomized RBS sequences that were screened (letters are based on IUPAC code). Right: Switch function was assessed using disk diffusion assays in which *E. coli* carrying the switch (without a cargo gene inserted) were spread at a density high enough to produce a lawn of growth on an agar plate. A disk impregnated with concentrated aTc was then used to induce switch activity, thereby making the adjacent cells express GFP if the switch was functional. Top right: Original switch prototypes failed to be induced and displayed suppressed expression of the dTomato tracker, which we surmised was due to overexpression of TetR. Bottom right: A library of switch clones containing random RBS sequences in the tetR 5' UTR were screened, resulting in the recovery of a functional clone that displayed sensitive switch activation and robust tracker expression. (D) Top row: Early switch prototypes relied on the co-transcription of the cargo gene and sfGFP reporter. However, the insertion of large cargo genes, such as a dcas9 or cheA2, hampered sfGFP expression compared to an “empty” switch without a cargo gene, which was evident in disk diffusion assays. We surmised that this was due to part-junction interference between sfGFP and the cargo, leading to poor translation of sfGFP. Bottom row: Insertion of the self-cleaving RiboJ ribozyme insulator between sfGFP and the cargo alleviated the apparent interference. (E) Left: Swimming motility of Δ motLOF in liquid media plus/minus aTc (50 ng/ml). Motility in liquid media was recorded for 10 seconds on a glass slide. Images show cellular movements over the entire 10 second period, which illustrates each cell's swimming trajectory. Motility was assessed 7 h post-induction. Middle: The percentage of swimming cells in Δ motLOF populations in liquid media plus/minus aTc (50 ng/ml) from four separate fields of view. Right: Probability densities

showing the distribution of cellular swimming speeds in liquid media for Δ motLOF plus/minus aTc (50 ng/ml). Sample sizes (measured bacterial swim tracks): Δ motLOF -aTc = 2,677; Δ motLOF +aTc = 944. (F) In vitro growth curves of Δ motLOF in rich media (lysogeny broth) plus/minus aTc (50 ng/ml). Line traces the average optical density (OD) from three replicate wells, bars indicate range. Underlying data plotted in E and F are provided in S1 Data.

S4 Fig. In vitro characterization of motility and chemotaxis gain-of-function switches and supporting data on the evolution of gain-of-function switches in vivo. (A) Left: Swimming motility of Δ motGOF and Δ cheGOF in liquid media plus/minus aTc (50 ng/ml). Motility in liquid media was recorded for 10 seconds on a glass slide. Images show cellular movements over the entire 10 second period, which illustrates each cell's swimming trajectory. Motility was assessed 4 h post-induction. Right: Motility of wild-type Vibrio, Δ motGOF, and Δ cheGOF in soft agar plus/minus aTc (10 ng/ml). Swim distances were captured 6 h post-inoculation of bacteria into the agar. (B) Swim distances of wild-type Vibrio, Δ motGOF, and Δ cheGOF in soft agar 6 h post-induction with different concentrations of aTc. (C) In vitro growth curves of Δ motGOF and Δ cheGOF in rich media (lysogeny broth) plus/minus aTc (50 ng/ml). Line traces the average optical density (OD) from three replicate wells, bars indicate range. (D) Cultivation-based abundances of Δ motGOF or Δ cheGOF at 72 hpi either with (green) or without (magenta) aTc induction. Abundances of wild-type Vibrio (gray), Δ mot (purple), and Δ che (cyan) (from Fig 1A, 72 hpi) are shown for comparison. Abundances of each GOF strain in the presence of aTc are from Fig 5E and are also shown for comparison. Bars denote medians and interquartile ranges. Letters denote significant differences. $p \leq 0.05$, Kruskal-Wallis and Dunn's

multiple comparisons test. (E) Shown is the fraction of “evolved clones” (i.e., bacterial colonies recovered that displayed constitutive switch activation) from the intestines of zebrafish colonized with Δ motGOF or Δ cheGOF at 72 hpi that were either induced (green) or not induced (magenta) with aTc. Bars denote medians and interquartile ranges. In each condition, a black dashed bar and diamond labeled with a “w” indicates the fraction of evolved clones recovered from the water environment. Underlying data plotted in B–E provided in S1 Data.

S1 Mov. Montage of real time movies showing wild-type Vibrio, Δ mot, and Δ che within larval zebrafish intestines. Movies were acquired by light sheet fluorescence microscopy at 24 hpi. Wild-type Vibrio is highly motile and planktonic, with swimming cells frequently making close contact with the intestinal epithelium. The bright signal in the left side of the frame is a mass of motile cells that is too dense for individuals to be resolved (see Fig 2C). In contrast, Δ mot is largely aggregated and confined to the lumen. The Δ che mutant exhibits an intermediate phenotype consisting of a motile subpopulation that is less dense than wild-type populations. The first three fields of view shown center on the foregut region. The fourth field of view (“che-midgut”) centers on the midgut to highlight aggregates of Δ che cells within this region. For the fourth field of view, intensities were log-transformed to highlight both the structure of the aggregates and the motile, planktonic cells visible in the lower left. Scale bar = 50 μ m.

S2 Mov. Montage of animated z-stacks showing wild-type Vibrio, Δ mot, and Δ che within larval zebrafish intestines. Movies were acquired by light sheet fluorescence microscopy at 24 hpi. Wild-type Vibrio is highly motile and planktonic, with swimming cells frequently making close contact with the intestinal epithelium. The bright signal in the left side of the frame is a mass of motile cells

that is too dense for individuals to be resolved (see Fig 2C). In contrast, Δ mot is largely aggregated and confined to the lumen. The Δ che mutant exhibits an intermediate phenotype consisting of a motile subpopulation that is less dense than wild-type populations. The field of view centers on the foregut region. The label in the upper-right corner denotes the depth in z (left-right) through the intestine. Scale bar = 50 μ m.

S3 Mov. Montage of time-lapse movies showing wild-type Vibrio, Δ mot, and Δ che within larval zebrafish intestines. Movies were acquired by light sheet fluorescence microscopy starting at 24 hpi. Wild-type Vibrio cells, which are highly motile and planktonic, robustly localize to the foregut region. The bright signal in the left side of the frame is a stable mass of motile cells that is too dense for individuals to be resolved (see Fig 2C). In contrast, Δ mot is largely aggregated, confined to the lumen, and exhibits large fluctuations in spatial organization, including the rapid expulsion of a large aggregate. The Δ che mutant exhibits an intermediate phenotype, consisting of a motile subpopulation that is less dense than wild-type populations with large, multicellular aggregates. A large aggregate of Δ che cells is expelled near the end of the movie. The field of view spans the entire larval intestine. Scale bar = 200 μ m.

S4 Mov. Animation of the spatiotemporal dynamics of wild-type Vibrio, Δ mot, and Δ che within larval zebrafish intestines. Through computational image analysis, bacterial populations were segmented and enumerated. From this quantification, we computed the fraction of the population that were single cells (planktonic fraction) and computed the population center of mass along the length of the gut (population center). Each marker represents an entire bacterial population from an individual fish. The movie depicts the time evolution

of multiple populations in this 2-dimensional phase space. Wild-type *Vibrio* populations robustly localize to the foregut region and maintain a high planktonic fraction. In contrast, Δmot and Δche populations undergo large fluctuations in aggregation and localization over time.

S5 Mov. Inactivation of swimming motility in established VibriomotLOF populations using the motility loss-of-function switch. Shown are two examples of VibriomotLOF switching dynamics within the larval zebrafish intestine captured by light sheet fluorescence microscopy. VibriomotLOF initially colonized each intestine in a phenotypically wild-type state (i.e., switch = “OFF”) with cells expressing only dTomato (magenta) and displaying a strong localization to the foregut and a high fraction of motile cells. At time zero, populations were induced by addition of aTc to the media. Both examples show the emergence of a multicellular aggregate from the anterior population of motile cells, a posterior-shift in overall distribution, and an increase in GFP expression signaling switch activation. Scale bars for time-lapses are 200 μm . Each frame of the time-lapses are maximum intensity projections of a 3D image stack across the full intestinal volume. For the second example, we highlight the 3D structure of an emerging bacterial aggregate (arrow) with an animated rendering (dTomato fluorescence only). Scale bar for the rendering is 50 μm . The montage ends with a real time movie of VibriomotLOF cells approximately 16 h post-induction showing widespread loss of motility (dTomato fluorescence only). Real time movie scale bar = 50 μm .

S6 Mov. Activation of swimming motility in an established ΔmotGOF population using the motility gain-of-function switch. ΔmotGOF initially colonized the intestine with the motility gain-of-function switch in the “OFF” state and therefore was non-motile and assembled a population that was aggregated and had

a poster-shifted distribution. At time zero, the population was induced by addition of aTc to the media. The resulting switching dynamics were captured by light sheet fluorescence microscopy. Each frame of the time-lapse is a maximum intensity projection of a 3D image stack across the full intestinal volume. Over time, motile cells appear and occupy the foregut region. Scale bar = 200 μ m. Following the time-lapse, we show a real time movie of a different fish at approximately 6 h post-induction that captures induced Δ motGOF cells swimming within the foregut.

Real time movie scale bar = 50 μ m.

S7 Mov. Activation of chemotaxis in an established Δ cheGOF population using the chemotaxis gain-of-function switch. Δ cheGOF initially colonized the gut with the chemotaxis gain-of-function switch in the “OFF” state and therefore was non-chemotactic and assembled a population that was aggregated and had a poster-shifted distribution. At time zero, the population was induced by addition of aTc to the media. The resulting switching dynamics were captured by light sheet fluorescence microscopy. Each frame of the time-lapse is a maximum intensity projection of a 3D image stack across the full intestinal volume. Over time, there is a dramatic increase in the number of planktonic and motile cells that occupy the foregut region. Scale bar = 200 μ m. Following the time-lapse, we show a real time movie of a different fish at approximately 6 h post-induction that captures induced Δ cheGOF cells swimming within the foregut. Real time movie scale bar = 50 μ m.

S8 Mov. Migratory behavior of tnfa:GFP+ cells. Time-lapse movie of a live tnfa:GFP transgenic larval zebrafish showing the migratory behavior of gut-associated tnfa+ cells (arrowheads). Images were acquired by light sheet fluorescence microscopy. Each frame of the time-lapse is a maximum intensity

projection of a 3D image stack that captures the full intestinal volume. Scale bar = 200 μm .

S9 Mov. Animated z-stack of a tnfa:GFP/mpeg1:mCherry double transgenic larval zebrafish colonized with wild-type Vibrio. The mpeg1:mCherry reporter and Vibrio dTomato marker were imaged simultaneously using a single excitation and emission system, and are shown in magenta. tnfa:GFP fluorescence is shown in green. Images were acquired by light sheet fluorescence microscopy. We first show an animated z-stack that depicts single planes of the light sheet with the depth (left–right) indicated in the upper right. tnfa+ and mpeg1+ single-positive cells, as well as tnfa+/mpeg1+ double-positive cells, are apparent. Scale bar = 50 μm . Following the animated z-stack, we show a two-color, 3D rendering. Rendering scale bar = 50 μm .

S10 Mov. Spatial distribution of tnfa+ host cells responding to swimming bacterial cells within the intestine. Montage shows the foregut region of a larval zebrafish carrying the tnfa:GFP reporter (green) colonized with ΔmotGOF (magenta) 24 h post-induction of the motility gain-of-function switch with aTc. Images and real time movie were acquired by light sheet fluorescence microscopy. We first show an animated z-stack that depicts single planes of the light sheet with the depth (left–right) indicated in the upper right. Arrows indicate tnfa+ host cells and bacterial cells. Next, we show a 3D rendering of the same intestine, which highlights the association of tnfa+ host cells with the mucosa. The montage ends with a real time movie of a single optical plane showing the swimming behavior of induced ΔmotGOF cells relative to tnfa+ host cells within the mucosa. All scale bars = 50 μm .

S1 Table. Bacteria used and created in this study

S2 Table. Plasmids used and created in this study

S3 Table. Primer and oligo DNA sequences

S1 Data. File (.xls) containing all plotted numerical data

S1 raw images. File containing images of DNA gels shown in S1 Fig

REFERENCES CITED

APPENDIX C

CONCLUSION

A reference to an image can be done like this one, to Figure S2. You might also want to cite an article like this: [?].



FIGURE S2. This is a short description that goes in the Table of Figures. This is an extension of that description, which may include cascading turns of phrase, which appears directly below the figure as expected, but not in the table of figures which appears at the beginning of this exceedingly amazing dissertation.